Model-based Cooperative Acoustic Navigation and Parameter Identification for Underactuated Underwater Vehicles

by

Zachary J. Harris

A dissertation submitted to The Johns Hopkins University in conformity with the requirements for the degree of Doctor of Philosophy.

Baltimore, Maryland

September, 2019

Abstract

This thesis reports novel theoretical and experimental results addressing two increasingly important problems in underwater robotics: model-based cooperative acoustic navigation for underwater vehicles (UVs) lacking a Doppler velocity log (DVL) and dynamic-model parameter estimation for underactuated UVs, such as the now-ubiquitous class of torpedo-shaped UVs. This thesis reports an extension of a method to identify simultaneously UV dynamical plant model parameters (parameters for critical terms such as mass, added mass, hydrodynamic drag, and buoyancy) and control-actuator parameters (control-surface models and thruster model) in 6 degree of freedom (DOF) to tolerate simulated sensor measurement noise representative of representative of real-world sensor data, as well as extensive numerical simulations to evaluate the sensitivity of the approach to sensor noise.

The current state-of-the-art in one-way travel-time combined acoustic communication and navigation (cooperative acoustic navigation) is to utilize purely kinematic, constant-velocity plant process models together with an on-board bottom-lock DVL to provide frequent, high-accuracy velocity corrections. However, DVLs are expensive, power consumers, physically large, and limited to acoustic bottom-lock range, which restricts their use to $\mathcal{O}(10-100\text{m})$ above the sea floor or beneath surface ice. Simulation and experimental results reported herein indicate the submerged UV position estimate from cooperative acoustic navigation with a kinematic model is poor and even unstable in the absence of

DVL velocity observations. These simulation and experimental results also show that cooperative acoustic navigation with a dynamic plant model performs well without a DVL and outperforms DVL-based dead reckoning, at least in the situation presented herein where the magnitude of the ambient water-current velocity is small.

The performance of the UV dynamic model, i.e., its ability to predict the vehicle's state, depends primarily on the accuracy of the model structure and model parameters. Accurate estimates of these parameters are also required for model-based control, fault detection, and simulation of UVs. While the general form of dynamical plant models for UVs is well understood, accurate values for dynamic-model parameters are impossible to determine analytically, are not provided by UV manufacturers, and can only be determined experimentally. Moreover, oceanographic UVs are subject to frequent changes in physical configuration, including changes in ballasting and trim, on-board equipment, and instrumentation (both external and internal), which may significantly affect the vehicle dynamics. Plant-model parameter estimation is generally more difficult for underactuated, torpedo-shaped UVs than for fully actuated UVs with thrusters because: 1) the reduced actuation available on underactuated UVs limits the plant excitation that can be induced from the control inputs, and 2) torpedo-shaped vehicles are often actuated with control surfaces (e.g., fins, wings, rudders, etc), which are difficult to characterize independently of the plant-model parameters. For these reasons, we seek an approach to parameter estimation for underactuated UVs in 6 DOF that simultaneously estimates plant and actuator parameters and can be performed routinely in the field with minimal time and effort by the vehicle operator.

The goals of this thesis are to advance the state-of-the-art of (1) model-based state estimation for cooperative acoustic navigation of UVs and (2) dynamic plant-model parameter identification for underactuated UVs. The first goal is addressed with the evaluation of a dynamic UV plant model in cooperative acoustic navigation and a comparative analysis

ABSTRACT

of the dynamic UV model and kinematic UV model without a DVL. The second goal is addressed in a collaborative effort comprising: (1) the development of the nullspace-based least squares (NBLS) algorithm for underactuated UV plant-parameter and actuator-parameter estimation in 6 DOF, and (2) the extension of an adaptive identification (AID) algorithm, and corresponding stability proof, to estimate simultaneously plant-model and actuator parameters for underactuated UV with diagonal mass and drag matrices in 6 DOF with realistic sensor measurement noise. These capabilities were verified by in situ vehicle experiments with the JHU Iver3 autonomus underwater vehicle (AUV) and by simulation studies.

Thesis Adviser: Dr. Louis L. Whitcomb, Professor, Johns Hopkins University

Thesis Committee:

Dr. Louis L. Whitcomb, Professor, Johns Hopkins University
Dr. Marin Kobilarov, Assistant Professor, Johns Hopkins University
Dr. Dana Yoerger, Senior Scientist, Woods Hole Oceanographic Institution

Acknowledgements

To everyone who supported me. You know who you are. Especially my family: Jessica, my mom and dad, and my brother.

Special thanks also to Dave Reitz, Jim Eldred, and Gordon Roberts, who inspired and took the time to mentor my interest in maritime robotics when I was young.

Additional thanks to my collaborators: Louis, without whom this thesis would not exist; Tyler Paine for collaborating on the novel approaches to parameter estimation; and Ryan Eustice and Sarah Webster for generously and graciously allowing me to use and extend their code on cooperative acoustic navigation.

Dedication

to all those who taught or inspired me

Contents

List of Tables

LIST OF TABLES

List of Figures

LIST OF FIGURES

List of Acronyms

AID	adaptive identification
AIDP	adaptively identified parameter set
AIDPM	adaptively identified plant model
AHRS	attitude and heading reference sensor
AMBC	adaptive model-based control
AUV	autonomus underwater vehicle
CAD	computer aided design
CEKF	centralized extended Kalman filter
CFD	computational fluid dynamics
COTS	commerical off-the-shelf
COG	center-of-gravity
COB	center-of-buoyancy
CROSSIM	simulation for cross-validation
DEIF	decentralized extended information filter
DOF	degree of freedom
DVL	Doppler velocity log
GPS	global positioning system
IDSIM	identification simulation

List of Acronyms

INS	inertial navigation system
KF	Kalman filter
LBL	Long Baseline
LS	least squares identification
LSP	least squares identified parameter set
MAE	mean absolute error
ML	machine learning
NN	neural network
NBLS	nullspace-based least squares
PDC	proportional derivative control
LQR	linear-quadratic regulator
LQG	linear-quadratric Gaussian
OLS	ordinary least squares
PDS	positive definite symmetric
RMS	root mean square error
ROV	remotely operated vehicle
SLAM	simultaneous localization and mapping
TOA	time-of-arrival
TOL	time-of-launch
TLS	total least squares
TWTT	two-way travel-time
USBL	ultra-short baseline
UV	underwater vehicle
WHOI	Woods Hole Oceanographic Institution

Chapter 1

Introduction

1.1 Motivation

The operational horizons and opportunities of scientific exploration of the world's oceans are being dramatically expanded by the increasing capabilities of underwater vehicles (UVs) which enable scientists to access previously unexplored areas to conduct oceanographic surveys, collect physical samples, and deploy and recover instruments. The accuracy of scientific surveys conducted with UVs is limited by the geodetic accuracy of the vehicle's navigation.

The goal of this thesis is to improve geodetic localization capabilities for UVs by advancing the state-of-the-art of model-based navigation and dynamic plant-model parameter identification for the now-ubiquitous class of underactuated, torpedo-shaped UVs. In certain cases, such as hydrography surveys, one may perform a bundle adjustment to improve the navigation solution and resulting map; however, improving the UV's navigational accuracy generally results in more accurate bathymetric map products.

1.1.1 Cooperative Acoustic Navigation

Navigation methods for underwater vehicles utilizing velocity signals (e.g., dead-reckoning navigation and Doppler sonar navigation) or acceleration signals (e.g., inertial navigation) accumulate errors that grow unbounded with time and with distance traveled, and thus require independent observations of position to correct the drift accumulated in the navigation estimate.

For land and air vehicle navigation, the global positioning system (GPS) provides a readily available independent source of position corrections for acceleration-based and velocity-based navigation systems [16], but GPS is unavailable to submerged UVs. Bottom-lock Doppler-sonar velocity measurements are an excellent correction source for velocity estimates, and pressure depth sensor measurements are an excellent correction source for the depth (only) of velocity-based and acceleration-based position estimates. However, absolute XY position corrections are still required for bounded-error position estimation.

This thesis reports results for synchronous-clock, one-way travel-time combined acoustic communication and ranging (cooperative acoustic navigation) between acoustic modems for position measurements. Cooperative acoustic navigation is explained in detail in Section 2.1. Specifically, this thesis addresses the navigation problem of a submerged UV

1. operating in concert with a surface ship equipped with an acoustic modem and a

GPS,

2. equipped with an attitude sensor, depth sensor, and an acoustic modem, and
3. not equipped with a DVL or operating beyond DVL acoustic bottom-lock range.

The case of UV navigation without a DVL is relevant because DVLs may not be available on the small, low-cost UVs that are becoming increasingly popular and an increasing number of UVs are being operated in the mid-water column, far above the ocean floor or below surface ice, beyond the DVLs acoustic bottom-lock range, e.g., [90]. Both of these use-cases are areas of ongoing and expanding oceanographic research. Low-cost UVs are reducing the financial barrier to conducting oceanographic research, enabling smaller universities and laboratories to collect real data. And even for institutions that have access to full-scale ocean-going UVs with a full sensor suite including a DVL, there has been a push to explore the region of the ocean from 200m-1000m deep, known as the mid-water column, twilight zone, or mesopelagic zone where DVLs are unable to provide a useful signal. Preliminary studies show this region of the ocean may contain more biomass than the rest of the ocean combined and is largely unexplored [1].

1.1.1.1 First-Order Kinematic UV Process Models

First-order kinematic process models are models of UV motion that model the geometry of UV motion but do not account for externally applied forces/moments or control-actuator forces/moments acting on the UV. The most common assumption for kinematic process models in cooperative navigation is that the vehicle moves at a constant velocity.

Kinematic process models are simple to implement because they require little specific information about the UV, and they perform well in cooperative acoustic navigation with an attitude sensor when the vehicle has access to frequent velocity corrections, such as from a DVL. A kinematic process model with a DVL is the current state-of-the-art for cooperative acoustic navigation.

1.1.1.2 Second-Order Dynamic UV Process Models

Second-order dynamic process models are models of UV motion that model external forces acting on the vehicle—forces such as hydrodynamic lift and drag, and control-actuator forces and torques. Second-order dynamic UV process models appear to provide little benefit in cooperative acoustic navigation when the UV has access to attitude measurements and high-accuracy, frequent velocity measurements, as is the case with a DVL in bottom-lock range, because the velocity measurements from most DVLs have a lower covariance than the dynamic model's process noise. However, as shown in Chapter 3 of this thesis, second-order dynamic process models may significantly improve the cooperative acoustic navigation solution when the UV is not equipped with a DVL or is beyond DVL acoustic bottom-lock range.

Note that the utility of a second-order dynamic model in cooperative acoustic navigation depends entirely on the model's ability to predict accurately the UV state. Because the general structure of second-order dynamic models of UV motion is well known, the accuracy of the model in predicting the true vehicle state depends principally on the parameters used in the model. For this reason, it is impossible to separate the usefulness of dynamic UV models from the problem of identifying the parameters used in the dynamical model.

1.1.2 Parameter Identification of Nonlinear UV Plant Dynamics

We argue that model-based approaches to navigation, control, and fault detection that utilize precise nonlinear models of UV dynamics will enable more precise control and navigation, higher levels of autonomy, and more complex missions for UVs. For example, previously reported studies have shown that nonlinear adaptive model-based control (AMBC) can outperform proportional derivative control (PDC) in trajectory tracking for fully actuated UVs [53].

However, approaches to model-based navigation, model-based control, and model-based fault detection for UVs are limited by the accuracy of the plant parameters used in the dynamic model. While the general form of UV dynamical plant models has been understood since the 1950s [72], the dynamic-model parameters—i.e., parameters for terms including mass, added mass, hydrodynamic drag, buoyancy, and control actuators—are impossible to determine analytically and are not provided by UV manufacturers. An added difficulty is the real-world fact that UVs are subject to frequent changes in physical configuration that may significantly affect the vehicle dynamics. Such changes may include but are not limited to: lengthening or shortening the vehicle to accommodate different payloads, variation in ballasting and trim conditions, and changes to on-board equipment and instrumentation (both external and internal), and they all require the model parameters be re-estimated whenever the vehicle's configuration is significantly altered.

The three most common approaches to parameter estimation are:

1. utilizing data obtained in captive-motion experiments (e.g., towing a vehicle in a hydrodynamic test tank),
2. computational fluid dynamics (CFD), or
3. utilizing data obtained in full-scale experimental trials of an UV in controlled free motion (e.g., under open or closed loop control).

Captive-motion experiments are time consuming, expensive, and difficult to perform properly. Further, the results are valid only for the specific vehicle configuration tested, and it is often impractical to repeat the experiments for every possible configuration of the UV. Typically, the experimental setup involves either rotating-arm experiments or planar motion mechanism (PMM) experiments, such as towing a vehicle on a carriage with a load cell at a fixed velocity in a hydrodynamic test facility. Captive-motion experiments can be quite accurate in certain DOF, but these experiments often require decoupling the DOF, which can lead to model inaccuracies. Typically, separate tests are run with and without the control surfaces (fins) installed in order to isolate the fin drag from the body drag. Additionally, separate test facilities are often required to characterize the fin lift and drag as a function of the angle of attack. More typically, the fin lift and drag as a function of the angle of attack are not experimentally characterized.

Parameter estimation based on computational fluid dynamics uses numerical models of fluid flow around the vehicle to simulate virtual PMM tests. CFD-based approaches to model identification vary widely in accuracy, time, and cost. Additionally, CFD-based approaches require detailed computer aided design (CAD) models of the UV, which are difficult or impossible to obtain from commerical off-the-shelf (COTS) UV manufacturers. On the other hand, a main advantage of CFD-based parameter estimation is the ability to inform design choices during the preliminary vehicle design process.

While these approaches have advantages, both captive-motion experiments and CFD-based approaches are often infeasible for many UV users for reasons of cost, time, and practicality.

Parameter identification based on data collected in full-scale experimental trials of UVs in controlled free motion has several advantages over captive-motion experiments and CFD. First, the approach is accessible to any end user who can deploy an existing UV. Additionally, though beyond the scope of this thesis, an approach that utilizing full-scale experimental data can be extended to run in real-time during UV missions, which paves the way for online model-based fault detection. Parameter-identification methods from full-scale experimental trials largely fall into one of the following categories: least squares identification (LS), adaptive identification (AID), Kalman filter (KF) variants, and machine learning (ML) and neural network (NN) techniques. This thesis reports two novel algorithms for UV plant parameter identification from free-motion experiments, one based on least-squares regression analysis and one based on nonlinear adaptive estimation.

The near-ubiquitous class of torpedo-shaped AUV are underactuated in forward motion—they typically have only 3 or 5 control inputs (4 fin angles and 1 main propulsor), fewer than the UV's 6 DOF, and thus the control actuators cannot impart arbitrary forces and moments on the vehicle. This is significantly different from the case of fully-thruster-actuated ROVs where the thrusters are often capable of exerting arbitrary forces and moments on the vehicle. Torpedo-shaped UVs are controllable only when in forward motion, are incapable of hovering, and are physically unable to track general 6 DOF reference trajectories. This class of underactuated UVs presents real theoretical and practical challenges to the problem of experimentally estimating model parameters for the commonly accepted second-order nonlinear dynamics plant models. Specifically, the question arises if the control actuators have sufficient control authority to excite the plant sufficiently so that the plant model parameters are observable.

Additionally, torpedo-shaped UVs are often actuated with control surfaces (e.g., fins, wings, rudders, etc), the hydrodynamic parameters of which are difficult to characterize independently of the plant-model parameters. Remotely operated vehicles (ROVs), in contrast, are typically actuated by thrusters with a high jet velocity compared to the vehicle's advance velocity. This is an important distinction because thrusters with a low advance velocity that can be physically removed from the UV can typically be characterized in a bollard pull test, which is relatively straightforward to perform in a small tank with a load cell, while propellers with a high advance velocity through the water typically must be characterized in a hydrodynamic towing tank facility. To the best of our knowledge, with the exception of [58], upon which this work is based, there are no previously reported studies for parameter identification of underactuated UVs that simultaneously identify plant-model parameters and actuation parameters in 6 DOF utilizing simulated data from a UV in controlled free motion with realistic sensor measurement noise.

With the exception of the work by McFarland [52], many previously reported AID methods require on model-based adaptive tracking controllers and are not applicable when the UV is operating under any control law other than a specific adaptive tracking controller. On commercially available UVs, the user is often limited to using the proprietary controller provided by the manufacturer, and the user cannot replace the manufacturer's proprietary controller with an adaptive tracking controller. The AID approach reported herein works for UV operating under any known control inputs, and it is, therefore, applicable in the common situation of a UV operating on an unspecified, manufacturer-provided controller or in open-loop control.

1.2 Thesis Outline and Contributions

Chapter 2 - Cooperative Acoustic Navigation with a Kinematic Process Model: This chapter reviews the most common approach to cooperative acoustic navigation of underwater vehicles (UVs), specifically the centralized extended Kalman filter (CEKF) formulation of one-way travel-time (OWTT) combined acoustic navigation and communication (cooperative acoustic navigation), and examines the feasibility of employing cooperative acoustic navigation to provide both position and velocity corrections for UV navigation. The examination of acoustic range-rate observations in addition to acoustic range observations is motivated by the fact that most underwater acoustic modems compute a range rate as part of the acoustic receptions processing of each incoming acoustic data packet, yet no previous cooperative acoustic navigation studies report utilizing these velocity data.

Simulation results are reported utilizing a kinematic model with and without a DVL. These results show that the addition of acoustic range-rate observations does not appear to offer significant advantages for UVs navigation when the acoustic range measurements are good and the vehicle has access to DVL observations. The addition of range-rate measurements may improve navigation accuracy over the case of range-only observations in limited circumstances, such as poor acoustic-range accuracy.

In anecdotal simulation results, we observed poor performance and even instability of the CEKF solution in certain geometries between the ship and submerged vehicle when using a kinematic model without velocity corrections from a DVL, and hypothesized that a dynamic model would be better suited to acoustic navigation without a DVL.

Chapter 3 - Cooperative Acoustic Navigation with a Dynamic Process Model: This chapter reports the development and evaluation of a second-order, nonlinear dynamic process model for a UV within the framework of OWTT cooperative acoustic navigation.

Simulation and experimental results are reported using John Hopkins University's L3 Ocean Server Iver3 AUV (L3 OceanServer, Fall River, MA, USA) carried out in the Chesapeake Bay. The reported results suggest that the cooperative navigation algorithm utilizing a dynamical UV process model may offer a significant advantage over the purely kinematic model in the absence of frequent, high-accuracy velocity observations, as is the case when the UV does not have access to DVL measurements. Further, the results suggest that cooperative acoustic navigation with a dynamic model and no DVL may outperform DVL-based dead reckoning when the magnitude of the ambient water-current velocity is small. As a measure of validity, there appears to be good agreement between the simulated results and the experimental results.

Chapter 4 - Parameter Identification of Underactuated Underwater Vehicles: This chapter reports two novel algorithms for identifying the plant parameters (hydrodynamic mass, quadratic drag, gravitational force, and buoyancy parameters) and the actuator parameters (propeller coefficient and fin hydrodynamic lift and drag as a function of the commanded angle) for second-order, underactuated, rigid-body UV plants in 6 DOF.

The first algorithm is based on least-squares regression analysis. We formulate the least-squares problem to solve for a parameter vector in the nullspace of the regressor matrix, which allows us to estimate the plant parameters and actuator parameters simultaneously. We call this approach nullspace-based least squares (NBLS). NBLS requires signals of body orientation, linear body velocity, angular body velocity, linear body acceleration, and angular body acceleration. With low sensor noise, NBLS can uniquely identify the parameters for an uncoupled model, demonstrating an underactuated UV has sufficient excitation in the uncontrolled DOF. Simulation results from using the identified plant model in the framework of model-based OWTT cooperative acoustic navigation are also presented. This work was first published in [31]. Coauthor Tyler Paine collaborated on the mathematical formulation of the NBLS algorithm, and he took the lead on coding the NBLS algorithm. A noise sensitivity analysis is reported herein that shows NBLS is sensitive to noise in the measured translational body velocity signal.

The second algorithm is based on nonlinear adaptive systems theory, henceforth called adaptive identification (AID). The AID approach requires signals of body orientation, translational body velocity, and angular body velocity but not linear body acceleration or angular body acceleration. A Lyapunov function and corresponding stability proof are provided.

The AID approach for UVs in 6 DOF was developed by Christopher McFarland with the assumption that the control actuator parameters were known [52]. The AID algorithm reported by McFarland was extended by Tyler Paine to include the control-actuator parameters as part of the AID state [58]. An analytical stability proof of this extension to estimate simultaneously the plant-model parameters and control-actuator parameters in 6 DOF was reported in Paine's masters thesis utilizing scalar gains [58]. Paine and Harris contributed equally to the publication of this AID extension to estimate simultaneously the plant and control parameters with an analytic stability proof using scalar gains and a preliminary simulation effort conducted with the forward simulation and AID done in a loop [77]. However, preliminary anecdotal simulation efforts in post-processing the simulated data by the author indicated poor parameter convergence with scalar gains. This thesis extends Paine's stability proof to utilize diagonal gain matrices rather than scalar gains. This thesis also reports simulation results in 6 DOF with realistic sensor noise, as well as a measurement-noise sensitivity analysis. The simulation results corroborate the analytic stability analysis, showing that the adaptively estimated plant parameters are stable and converge to values that provide plant-model input-output behavior closely approximating the true input-output behavior.

To the best of our knowledge, this thesis reports the first method to identify decoupled UV dynamical process model parameters and actuator parameters (control-surface models and thruster model) in 6 DOF with realistic simulated sensor noise.

This approach to nonlinear model identification of UVs is evaluated in simulation studies. The resulting identified UV plant models are evaluated in simulation studies of cooperative navigation.

Chapter 5 - Combined Control and Navigation without a DVL: This chapter reports simulation results for combined control and navigation without a DVL in real time. This chapter is an extension to Chapter 3, which addresses only the solution to the acoustic navigation problem in post processing utilizing a dynamic UV model and no DVL and is agnostic to the controller used. This chapter examines the feasibility of using the cooperative acoustic navigation with a dynamic UV process model and no DVL as an input to the UV controller in real time. We report results with both proportional derivative (PD) and linear-quadratic regulator (LQR) controllers. We conclude that it is feasible to utilize the state estimate from the CEKF formulation of cooperative acoustic navigation utilizing a dynamic model without a DVL as an input to a control system.

Chapter 2

Cooperative Acoustic Navigation with a Kinematic UV Process Model

This chapter reviews cooperative acoustic navigation, providing the necessary background information on the centralized extended Kalman filter formulation. The principal original contribution in this chapter is an observation model for acoustic range-rate measurements and simulation and experimental results investigating the effect of adding acoustic range-rate measurements to acoustic range measurements. This chapter is organized as follows:

Section 2.1 overviews combined acoustic communication and navigation (cooperative acoustic navigation).

Section 2.2 reviews the relevant literature for cooperative acoustic navigation.

Section 2.3 reviews the centralized extended Kalman filter (CEKF) formulation, first reported in by Webster et al [81–84], including the vehicle state description (2.3.2).

Section 2.4 reviews the purely kinematic constant-velocity process model traditionally used in cooperative acoustic navigation.

Section 2.5 reviews the acoustic range observation model (again first reported in [84]) and reports a novel observation model for acoustic range-rate measurements.

Section 2.6 reports simulation results for a kinematic model in synchronous OWTT cooperative acoustic navigation utilizing acoustic range and acoustic range-rate observations with a DVL (2.6.1) and without a DVL (2.6.2).

2.1 Overview

Navigation methods for underwater vehicles utilizing velocity signals (e.g., dead-reckoning navigation and Doppler sonar navigation) or acceleration signals (e.g., inertial navigation) accumulate errors that grow unbounded with time and distance traveled, and thus require independent observations of absolute position or velocity to correct the drift accumulated in the navigation estimate.

For land and air vehicle navigation, the global positioning system (GPS) provides an ideal independent source of position corrections for acceleration and velocity-based navigation systems [16], but GPS is unavailable to submerged UVs. Bottom-lock Doppler-sonar velocity measurements are an excellent correction source for velocity estimates. Pressure depth sensor measurements are an excellent correction source for the depth (only) of velocity-based and acceleration-based position estimates.

For submerged underwater vehicles (for which GPS is unavailable), few methods currently exist for absolute XY position corrections. The most common XY position correction methods are time-of-flight acoustic navigation systems, such as long-baseline (LBL) and ultra-short baseline (USBL) acoustic navigation [36, 41, 55]. Range-only OWTT cooperative underwater navigation uses ranges estimated from the acoustic time-of-flight between subsea nodes, e.g., between two vehicles, or between a client vehicle and a server reference beacon of known (fixed or moving) location. When all vehicles and beacons (nodes) are equipped with precision clocks, each node's acoustic data transmission can be received by multiple receiving nodes—enabling all nodes within acoustic range to simultaneously (a) measure range to the transmitting node from the measured time-of-flight and (b) decode the data encoded in the acoustic data packet. This method provides both bounded-error position estimates and long-range capabilities with reduced need for multiple costly fixed beacons, as is the case with most LBL systems. Unlike traditional two-way travel-time (TWTT) ranging, in which a single TWTT range can serve only one client, OWTT ranging offers the advantage that a single OWTT range can serve many clients. This is called synchronous OWTT cooperative acoustic navigation. If the server reference beacon (e.g., ship, buoy, etc) is equipped with a GPS receiver and encodes its position into the acoustic data packet, synchronous OWTT cooperative acoustic navigation provides a geodetic navigation solution, as shown in Figure 2.1. In practice, the synchronous-clock OWTT measurement is simply the time of flight of the acoustic data packet. If the speed of sound in water is known, a range is computed from the OWTT time-of-flight measurement. into a range. With a range, the UV's position is bounded to be on a hemisphere centered at the ship. If the UV is equipped with a pressure-depth sensor, the hemisphere becomes a circle of possible positions, as shown in Figure 2.1. An extended Kalman filter (EKF) is used to estimate the UV's location on the circle. OWTT navigation also provides scalability by allowing all vehicles within acoustic range to simultaneously use the same acoustic data packet broadcast independent of the number of vehicles. Additionally, OWTT navigation requires multiple acoustic fixes for the position covariance to decrease.

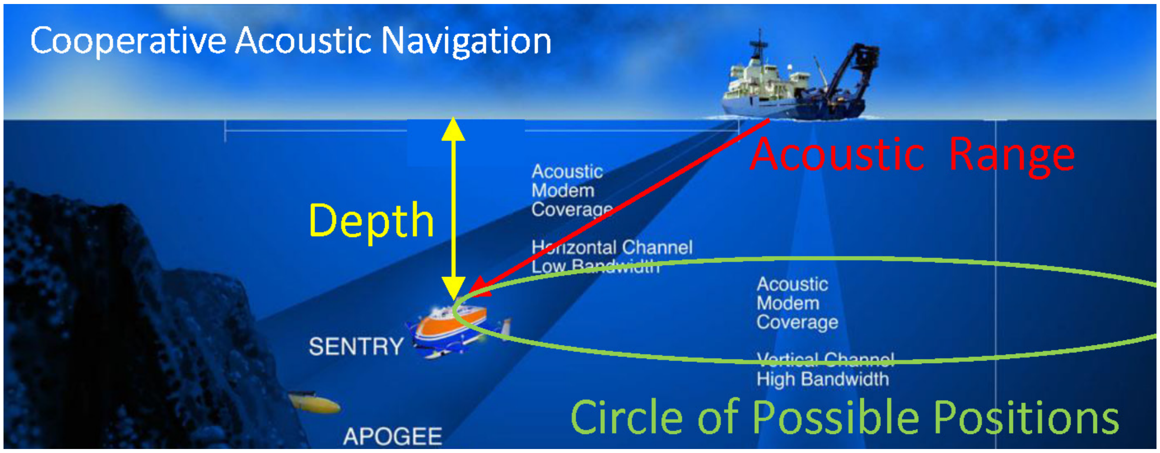

Figure 2.1: Graphical depiction of one-way travel-time (OWTT) cooperative acoustic navigation. A range is computed from the OWTT time of flight of the acoustic data packet using the speed of sound. This range bounds the UV's position to a hemisphere centered at the ship. When the UV is equipped with a depth sensor, the position is bounded to on a circle centered at the ship. An extended Kalman filter (EKF) is used to estimate the UV's location on the circle.

2.2 Literature Review

Radio-frequency (RF) telemetry is the preferred telemetry method for land, air, and space, but is not useful for underwater telemetry because the ocean is opaque to high-frequency RF telemetry. Even extremely low frequency RF telemetry can penetrate seawater only to tens or hundreds of feet [59]. The development of underwater acoustic modems, however, has enabled underwater data telemetry at ranges up to tens of kilometers [15, 40, 69]. The propagation delay of acoustic telemetry in seawater is about 1.5 km per second, and the data bandwidth varies with range, carrier frequency, and encoding (modulation) method.

2.2.1 Range-Only Underwater Navigation

To the best of our knowledge, the earliest reported comprehensive study of underwater-vehicle navigation using acoustic ranging was conducted by Spindell et al. [36] in which they reported full-scale experimental evaluation of an acoustic approach to underwater-vehicle navigation in which a single underwater vehicle could detect range from a set of fixed acoustic navigation transponders whose location was known *a priori*—a method that has since been widely practiced and is now commonly known as long-baseline (LBL) acoustic navigation.

Previous results by the authors and others [9, 61, 80, 83, 85] have shown the effectiveness of position corrections for Doppler and inertial navigation with range-only OWTT underwater navigation using ranges estimated from the acoustic time-of-flight of acoustic data packets between subsea nodes, e.g., between two vehicles or between a vehicle and a reference beacon of known (fixed or moving) location.

Studies by the authors and others report the development and at-sea experimental evaluation of OWTT systems (including hardware and software) for the navigation of underwater vehicles using maximum-likelihood estimation [21,22], the EKF [83], and the extended information filter (EIF) [85,86].

Several authors have reported least-squares methods for single-beacon range-only navigation [33, 44, 54, 67]. Range-only target tracking has been addressed using EKFs and maximum-likelihood estimators (MLE) [3,64,73]. The use of EKFs for homing and single-beacon navigation is reported in [5,6,45,46,78].

Recently, [17] reported the comparison of a particle filter and CEKF for OWTT navigation in post-processing on real-world data. The authors compare model-aided odometry, in the form of a water-velocity bias estimator, to DVL-aided odometry and conclude the PF slightly outperforms the CEKF. In both cases, a kinematic process model was used.

Most recently, [39] reported experimental results with OWTT acoustic navigation with a MEMS inertial measurement unit (IMU) and no DVL. The EKF utilizes a constant-acceleration process model with an accelerometer-bias model. The authors conclude the accuracy their approach is comparable to existing methods.

2.2.1.1 Observability of Single-Beacon Range-Based UV Navigation

The observability of single-beacon range-based UV navigation has been studied fairly extensively. Generally, previously reported studies have shown that the state of the submerged UV is observable provided there is sufficient richness and variability in the geometry of the ranges between the UV and single acoustic beacon.

In [67], Scherbatyuk reports a UV positioning method in the context of Long Baseline (LBL) acoustic positioning systems with on-board attitude sensor and velocity sensor based on least squares. Monte Carlo simulation results are presented to corroborate the analysis.

In [73], Song presents necessary and sufficient conditions for local observability in the context of two-dimensional maneuvering with range measurements from a single beacon. The approach taken in this paper utilizes the Fisher information matrix developed from the analytical treatment of system dynamics and noisy measurement equations established in a modified polar coordinate system. Numerical simulation results are presented to corroborate the analytical results.

In [64], Ristic et al. address the problem of target motion tracking from the range and range-rate measurements. A theoretical Cramer–Rao bound for the performance of an unbiased range-only tracking algorithm is derived, and three algorithms for target motion analysis are developed and compared to the theoretical performance bound. The three algorithms are: the maximum likelihood estimator, the EKF, and the regularized particle filter. Experimental validation of the theory is also presented.

Several studies addressed the observability of single-beacon range-only navigation with

EKF estimation approaches [25–28,49]. In [65], the authors report a nonlinear observability analysis, identifying conditions under which the system is locally weakly observable. In [37], the authors report employ nonlinear differential algebraic methods to derive conditions for observability.

In her 2006 doctoral thesis [43], LaPointe reports a single-beacon navigation approach in the form of a “virtual” LBL system (VLBL). The UV position is determined by advancing multiple ranges from a single transponder along the UV’s dead reckoning track. The UV position is then triangulated using these successive ranges in a manner analogous to a “running fix” in surface ship navigation. Simulation results for the Woods Hole Autonomous Benthic Explorer (ABE) UV are presented.

In [12] Batista et al. addresses the observability for UVs localization based on the range to a single beacon where the vehicle is equipped with an IMU and range measurements to a single source, in addition to angular velocity readings. The paper develops the necessary and sufficient conditions for observability for use in motion planning and control for an UV equipped with an IMU providing angular position and velocity measurements and range measurements to a single transducer. An Kalman filter (KF) is applied for body-frame state estimation, and simulation results are reported. In [13], the authors extend their previous work [12] to address the necessary and sufficient conditions for observability of an mobile agent based on the based on the range to a single source, in addition to relative velocity readings (range-rate observations).

In [18], Crasta et al. address observability of an UV moving in two dimensions using acoustic range to a single beacon at a known location with a nonlinear, kinematic model. In the presence of known ocean currents, the system is found to be globally observable in the sense of Herman and Krener for a constant relative course and constant (nonzero) relative course rate inputs. On the other hand, with unknown ocean currents the system fails to be locally weakly observable with constant relative course but the authors characterize the set of indistinguishable states from a given initial position and ocean current configuration and note that observability can be achieved with constant (nonzero) relative course rate in the presence of unknown, constant ocean currents. In [19], the authors extend the results of [18] to address observability of an UV moving in three dimensions in the presence of ocean currents, under the assumption that the vehicle can only measure its acoustic range to a fixed transponder. A nonlinear, kinematic model is used and the UV can undergo any maneuvers that are completely parameterized by the body velocity, a constant flight path angle, and a constant yaw rate. In the presence of known, constant ocean currents, the 3D kinematic model of the AUV that corresponds to trajectories with nonzero flight path angle and yaw rate is observable. When the latter conditions fail, the authors give a complete characterization of the sets of states that are indistinguishable from a given initial state. In the case of unknown constant ocean currents, the model is shown to be locally weakly observable for nonzero yaw rate.

In [62], Quenzer and Morgansen explore control approaches to improve localization performance of UVs deployed in survey missions. The authors propose two methods for local observability measures to determine the immediate action (control) for a UV. Simulation studies are presented to validate and compare both methods. The authors conclude that the first proposed method has comparable or better performance than an existing maximum information gain method in a lawn mower style survey mission.

In [4], Arrichiello et al. address observability of single and multiple UVs localization using acoustic range measurements with on-board sensors, including depth, velocity, and acceleration sensors. The paper examines the cases of a single UV ranging off a single transponder and multiple UV using inter-vehicle ranges. The paper shows that both the problems of absolute localization of a single vehicle and the relative localization of multiple vehicles may be treated using the same mathematical framework. Tailoring concepts of observability derived for nonlinear systems, the authors analyze how the performance in localization depends on the types of motion imparted to the UV. They propose a well-defined observability metric and report simulation and experimental validation with an EKF state observer. They conclude that performance depends on the UV's motion.

In [60], Parlangeli and Indiveri address observability in the context of single-beacon ranges with a kinematic UV model. Their paper extends previous results building on an augmented state technique allowing to reformulate the nonlinear observability problem in terms of a linear time varying (LTV) one. Globally unobservable motions are characterized in terms of initial conditions and commanded velocity signals. An underactuated model is considered, and a numerical simulation study is presented to demonstrate certain cases where the system is unobservable.

In [20], De Palma et al. address observability for the single beacon localization problem of an UV using a nonlinear, kinematic “double integrator” model with acceleration as the model input and range to a stationary beacon as the output. The observability analysis addresses two complementary issues: the local weak observability for the nonlinear system, and, similar to [60], the global observability for a LTV representation of the system derived through a state augmentation method. The proposed methods for observability analysis are discussed in different case studies (e.g. 2D/3D, absence/presence of current, and presence of additional sensors like a DVL and a depth sensor). A numerical simulation study is presented to corroborate the analytical observability results.

Additionally, several authors have addressed OWTT navigation of surface and underwater vehicles in a simultaneous localization and mapping (SLAM) framework using distributed estimators [7–10, 23].

2.2.2 Acoustic Range Rate

To the best of our knowledge, the earliest study of underwater-vehicle navigation employing acoustic detection of *both range and range rate* was the 1978 study by Spindell et al. [74], which extended the approach reported in [36] by reporting a full-scale experimental evaluation of an approach to underwater-vehicle navigation in which a single underwater vehicle could detect both range and range rate from a set of fixed navigation transponders whose location was known *a priori*.

In [47, 48], the author, apparently unaware of [36, 74], reported the notion of employing acoustic range rate in addition to acoustic range for LBL navigation but did not report specific navigation algorithms for employing range rate nor any experimental evaluation. In [30], the author reports the notion of an underwater acoustic modem estimating and compensating for the Doppler shift of a received acoustic data packet transmission but does not address how a Doppler estimate might be used for navigation.

In [14], the author reported the experimental evaluation of algorithms for acoustically determining the *relative position* of two marine vehicles by employing measurement of acoustic range and acoustic range rate with specific focus on estimating relative positioning conditions, such as the closest-point-of-approach (CPA) of two vessels for the purpose of collision-avoidance.

2.3 Extended Kalman Filter

This section briefly describes the centralized extended Kalman filter (CEKF) and associated process model and observation models used. The primary original contribution reported in this section is the acoustic range-rate observation model (Section 2.5.1.1).

2.3.1 EKF Formulation and Implementation

The extended Kalman filter is a non-optimal extension of the KF to nonlinear plants and observations by linearizing about the time-varying estimated state. A full derivation and formulation of the EKF is available in many texts and is beyond the scope of this thesis, see [11, 75, 81].

The equations for a general nonlinear plant model in continuous time and general nonlinear observation model in discrete time are:

$$\dot{x} = f\big(x(t), u(t)\big) + G(t)w(t) \tag{2.1}$$

$$z_k = h\big(x(t_k)\big) + v_k \ \ \forall k = 1, 2, ... \tag{2.2}$$

where f is the general nonlinear plant model, h is the general nonlinear observation model, $x(t)$ is the continuous-time state, $u(t)$ is the continuous-time control signal, and z_k is a general measurement at time t_k. $v_k \sim \mathcal{N}(0, Q(t))$ is the zero-mean Gaussian process noise, and $v_k \sim \mathcal{N}(0, R_k)$ is the zero-mean Gaussian measurement noise. Note that, in practice, we utilize several observation models reporting data asynchronously.

We linearize the nonlinear process model about the state at time $t = t_k$ with a first-order Taylor series expansion and discretize using zero-order hold. Mathematically,

$$\begin{aligned}
\dot{x} =& f\big(x(t), u(t)\big) + G(t)w(t) && (2.3)\\
=& f\big(x(t_k), u(t_k)\big) + F_x\Big(x(t) - x(t_k)\Big) + F_u\Big(u(t) - u(t_k)\Big) + HOT + G(t)w(t) && (2.4)\\
=& F_x x(t) + f\big(x(t_k), u(t_k)\big) - F_x(t_k) + F_u\Big(u(t) - u(t_k)\Big) + HOT + G(t)w(t), && (2.5)
\end{aligned}$$

where HOT is the higher order terms, F_x is the Jacobian with respect to x, and F_u is the Jacobian with respect to the control, i.e.,

$$F_x = \frac{\partial f(x(t), u(t))}{\partial x}\bigg|_{x=x(t_k)} \tag{2.6}$$

$$F_u = \frac{\partial f(x(t), u(t))}{\partial u}\bigg|_{u=u(t_k)}. \tag{2.7}$$

We note that the UV plant kinematic model (2.23) does not have control inputs, so $F_u = 0$; for the UV plant dynamic model (3.2), we assume the input is piecewise constant over the time step, so $u(t) - u(t_k) = 0$. For the linear approximation, we drop the HOT, and (2.5) simplifies to

$$\dot{x} = F_x x(t) + \underbrace{f\big(x(t_k), u(t_k)\big) - F_x(t_k)}_{\bar{u}(t_k)} + G(t)w(t) \tag{2.8}$$

$$= F_x x(t) + \bar{u}(t_k) + G(t)w(t), \tag{2.9}$$

where $\bar{u}(t_k) = f\big(x(t_k), u(t_k)\big) - F_x(t_k)$ is treated as a constant pseudo-input term. Note that (2.9) is in the standard state-space form,

$$\dot{x} = Ax(t) + Bu(t) + Gw_k \tag{2.10}$$

with $A = F_k$ and $B = \mathbb{I}$. Thus, we can discretize using zero-order hold, a standard method of discretization, the details of which are available in several references, e.g., [81], and will not be repeated here. The end result after discretizing is the standard state-space discrete-time linear system

$$x_{k+1} = F_k x_k + B_k u_k + w_k, \tag{2.11}$$

where F_k is the discrete-time linear state transition matrix, $B_k = \mathbb{I}$ is the discrete-time linear input matrix, and u_k is the piecewise-constant input, all at time step t_k.

The EKF process prediction equations are

$$\mu_{k+1|k} = F_k \mu_{k|k} + B_k u_k \tag{2.12}$$

$$\Sigma_{k+1|k} = F_k \Sigma_{k|k} F_k^T + Q_k \tag{2.13}$$

where $\mu_{i|j}$ is the estimate of the state at time step t_i given the estimate at time step t_j, and Q_k is the discrete-time measurement error covariance.

The EKF measurement update equations are

$$\mu_{k|k} = \mu_{k|k} + K_k\Big(z_k - h(\mu_{k|k-1})\Big) \tag{2.14}$$

$$\Sigma_{k|k} = \Sigma_{k|k-1} - K_k H_k \Sigma_{k|k-1}, \tag{2.15}$$

where H_k is the Jacobian of the nonlinear observation model h at time t_k,

$$H_k = \frac{\partial h\big(x(t_k)\big)}{\partial x(t_k)}\Bigg|_{x(t_k)=\mu_{k|k-1}}, \tag{2.16}$$

and K_k is the Kalman gain at time t_k,

$$K_k = \Sigma_{k|k-1} H_k^T \Big(H_k \Sigma_{k|k-1} H_k^T + R_k\Big)^{-1}. \tag{2.17}$$

2.3.1.1 Implementation for Cooperative Acoustic Navigation

A discrete-time, delayed-state EKF was implemented to fuse depth, gyrocompass, and DVL measurements (when applicable) from the vehicle, GPS measurements from the ship, and acoustic range and range-rate measurements between the vehicle and the ship. We utilize the centralized extended Kalman filter (CEKF) variant, which assumes simultaneous access to vehicle and ship sensor data simultaneously. As a centralized algorithm, the CEKF is suitable for post-processing simulated and experimental data. Previous results have shown that the centralized approach can be extended exactly to a decentralized extended information filter (DEIF) form, and at OWTT measurement updates, the CEKF is analytically and experimentally identical to its decentralized counterpart, the DEIF, as reported in [85]. Additionally, the reader is referred to [83] for the subtleties of the modified process prediction, which occurs when the state augmentation is performed in concert with the process-prediction step.

2.3.1.2 EKF Initialization

In practice, the CEKF position is initialized from the last valid GPS fix of the UV before it submerges, and the velocity is initialized to the DVL reading at that same time or the UV's commanded forward velocity in the case of no DVL.

2.3.2 State Description

As is typical for the CEKF cooperative navigation algorithm [81–84], we define the state vector, $\mathbf{x}$, as the composite of the current vehicle state, current ship state, and n delayed states. Delayed states are required for causal processing because the range measurement occurs between the ship at time-of-launch (TOL) and the vehicle at time-of-arrival (TOA). The state vector used in the CEKF is

$$\mathbf{x} = \begin{vmatrix} x_v^T & x_s^T & x_{v-1}^T & x_{s-1}^T & \ldots & x_{v-n}^T & x_{s-n}^T \end{vmatrix}^T, \tag{2.18}$$

where the current ship state x_s is a 6-DOF vector containing the XY-position and heading and their respective velocities

$$x_s = \begin{vmatrix} x & y & \psi & \dot{x} & \dot{y} & \dot{\psi} \end{vmatrix}^T, \tag{2.19}$$

and the current vehicle state x_v is a 12-DOF vector containing the local-level pose and body-frame velocities

$$x_v = \begin{vmatrix} s^T & \varphi^T & \nu^T & \omega^T \end{vmatrix}^T \tag{2.20}$$

$$s = \begin{vmatrix} x \\ y \\ z \end{vmatrix} \quad \varphi = \begin{vmatrix} \phi \\ \theta \\ \psi \end{vmatrix} \quad \nu = \begin{vmatrix} u \\ v \\ w \end{vmatrix} \quad \omega = \begin{vmatrix} p \\ q \\ r \end{vmatrix}, \tag{2.21}$$

where s is the local-level position, φ is the local-level attitude, ν is the body-frame linear velocity, and ω is the body-frame angular velocity. For convenience, we also define

$$\eta = \begin{vmatrix} s^T & \varphi^T \end{vmatrix}^T \qquad v = \begin{vmatrix} \nu^T & \omega^T \end{vmatrix}^T. \tag{2.22}$$

2.4 Kinematic Process Model

In this chapter, we utilize a kinematic, nonlinear process model for both the vehicle and the ship, identical to the one reported in [83]. Unlike the dynamic model reported later in this thesis (Section 3.1), this process model is a purely kinematic, constant-velocity second-order plant with process noise. The process model for the vehicle is linearized and discretized for use in the EKF standard methods [11].

The vehicle kinematics are

$$\dot{\eta} = K(\varphi)v, \tag{2.23}$$

where

$$K(\varphi) = \begin{bmatrix} R(\varphi) & 0 \\ 0 & L(\varphi) \end{bmatrix} \tag{2.24}$$

is the kinematics matrix. $R(\varphi)$ is the transformation between inertial and body-frame linear velocities, and $L(\varphi)$ is the transformation between inertial and body-frame angular velocities. Explicitly,

$$R(\varphi) = R_z(\psi)^T R_y(\theta)^T R_x(\phi)^T, \tag{2.25}$$

where

$$R_z(\psi) = \begin{bmatrix} \cos(\psi) & \sin(\psi) & 0 \\ -\sin(\psi) & \cos(\psi) & 0 \\ 0 & 0 & 1 \end{bmatrix}, \tag{2.26}$$

$$R_y(\theta) = \begin{bmatrix} \cos(\theta) & 0 & -\sin(\theta) \\ 0 & 1 & 0 \\ \sin(\theta) & 0 & \cos(\theta) \end{bmatrix}, \tag{2.27}$$

$$R_x(\phi) = \begin{bmatrix} 1 & 0 & 0 \\ 0 & \cos(\phi) & \sin(\phi) \\ 0 & -\sin(\phi) & \cos(\phi) \end{bmatrix}, \tag{2.28}$$

and

$$\begin{aligned}\omega =& e_1\dot{\phi} + R_x(\phi)e_2\dot{\theta} + R_x(\phi)R_y(\theta)\dot{\psi} && (2.29)\\ =& \underbrace{\begin{bmatrix} 1 & 0 & -\sin(\theta) \\ 0 & \cos(\theta) & \sin(\phi)\cos(\theta) \\ 0 & -\sin(\phi) & \cos(\phi)\cos(\theta) \end{bmatrix}}_{L(\varphi)^{-1}}, && (2.30)\end{aligned}$$

where $e_1 = |1\ 0\ 0|^T \in \mathbb{R}^3$, $e_2 = |0\ 1\ 0|^T \in \mathbb{R}^3$, and $e_3 = |0\ 0\ 1|^T \in \mathbb{R}^3$. Thus,

$$L(\varphi) = \begin{bmatrix} 1 & \sin(\phi)\tan(\theta) & \cos(\phi)\tan(\theta) \\ 0 & \cos(\phi) & -\sin(\phi) \\ 0 & \sin(\phi)\sec(\theta) & \cos(\phi)\sec(\theta) \end{bmatrix}. \tag{2.31}$$

We re-write (2.23) in state-space representation with the full 12 DOF vehicle state for use in the CEKF

$$\dot{x}_v = \begin{bmatrix} 0 & 0 & R(\varphi) & 0 \\ 0 & 0 & 0 & L(\varphi) \\ 0 & 0 & 0 & 0 \\ 0 & 0 & 0 & 0 \end{bmatrix} x_v + \begin{bmatrix} 0 & 0 \\ 0 & 0 \\ \mathbb{I} & 0 \\ 0 & \mathbb{I} \end{bmatrix} w_v \tag{2.32}$$

$$\dot{x}_s = \begin{bmatrix} 0 & \mathbb{I} \\ 0 & 0 \end{bmatrix} x_s + \begin{bmatrix} 0 \\ \mathbb{I} \end{bmatrix} w_s, \tag{2.33}$$

where $w_v \sim \mathcal{N}(0, Q_v)$ and $w_s \sim \mathcal{N}(0, Q_s)$ are zero-mean Gaussian process noise terms. Positions are represented in inertial world coordiates. Vehicle velocities are represented in body-coordinates, and ship velocities are represented in world-coordinates. The process model for the vehicle is linearized and discretized using standard methods [11]. The reader is referred to [83] for a full description and derivation, including the linearized discrete-time process model and the subtleties of the modified process prediction, which occurs at the top of the second when the state augmentation is performed in concert with the process-prediction step.

2.5 Observation Models

The range and range-rate observation models are nonlinear functions of the vehicle state at TOA and the ship state at TOL. Observation models of the additional sensors, including the DVL, GPS, depth sensor, and gyrocompass, are detailed in [81].

2.5.1 Range Observation Model

As reported in [83], the range observation model can be written in matrix notation as

$$z_{rng} = \left(\mathbf{x}^T \boldsymbol{A}^T \boldsymbol{A} \mathbf{x}\right)^{\frac{1}{2}} + v_{rng}, \tag{2.34}$$

where $v_{rng} \sim \mathcal{N}(0, R_{rng})$ and

$$\boldsymbol{A} = \left| -\boldsymbol{J}_v \;\; \mathbf{0} \ldots \mathbf{0} \;\; \boldsymbol{J}_s \;\; \mathbf{0} \ldots \mathbf{0} \right|^T, \tag{2.35}$$

with $\boldsymbol{J}_v$ and $\boldsymbol{J}_s$ defined such that

$$\boldsymbol{J}_v\, x_v = \begin{vmatrix} x & y & z \end{vmatrix}^T \tag{2.36}$$

$$\boldsymbol{J}_s\, x_s = \begin{vmatrix} x_s & y_s & 0 \end{vmatrix}^T . \tag{2.37}$$

The measurement covariance, R_{rng}, represents the noise of the range measurement. The Jacobian of the range measurement with respect to the full state, $\mathbf{x}$, is

$$\begin{aligned} \boldsymbol{H}_k =& \left.\frac{\partial\, z_{rng}(\mathbf{x})}{\partial\, \mathbf{x}}\right|_{\mathbf{x}=\boldsymbol{\mu}_{k|k-1}} \\ =& \left(\boldsymbol{\mu}_{k|k-1}^T \boldsymbol{A}^T \boldsymbol{A} \boldsymbol{\mu}_{k|k-1}\right)^{-\frac{1}{2}} \boldsymbol{\mu}_{k|k-1}^T \boldsymbol{A}^T \boldsymbol{A}. \end{aligned} \tag{2.38}$$

2.5.1.1 Range-Rate Observation Model

As reported in [32], the range-rate observation model is the time derivative of (2.34). Explicitly,

$$z_{rr} = \left(\mathbf{x}^T \boldsymbol{A}^T \boldsymbol{A} \mathbf{x}\right)^{-\frac{1}{2}} \mathbf{x}^T \boldsymbol{A}^T \hat{\boldsymbol{A}} \mathbf{x} + v_{rr}, \tag{2.39}$$

where $v_{rr} \sim \mathcal{N}(0, R_{rr})$ and

$$\hat{\boldsymbol{A}} = \begin{vmatrix} -\hat{\boldsymbol{J}}_v & \mathbf{0} \dots \mathbf{0} & \hat{\boldsymbol{J}}_s & \mathbf{0} \dots \mathbf{0} \end{vmatrix}^T , \tag{2.40}$$

with $\hat{\boldsymbol{J}}_v$ and $\hat{\boldsymbol{J}}_s$ defined such that

$$\hat{\boldsymbol{J}}_v\, \boldsymbol{R}(\boldsymbol{\varphi})\, x_v = \begin{vmatrix} \dot{x} & \dot{y} & \dot{z} \end{vmatrix}^T \tag{2.41}$$

$$\hat{\boldsymbol{J}}_s\, x_s = \begin{vmatrix} \dot{x}_s & \dot{y}_s & 0 \end{vmatrix}^T . \tag{2.42}$$

The Jacobian of (2.39) with respect to the full state, $\mathbf{x}$, is

$$\begin{aligned}
\boldsymbol{H}_k =& \left.\frac{\partial\, z_{rr}(\mathbf{x})}{\partial\, \mathbf{x}}\right|_{\mathbf{x}=\boldsymbol{\mu}_{k|k-1}} \\
=& -\left(\boldsymbol{\mu}_{k|k-1}^T \boldsymbol{A}^T \boldsymbol{A} \boldsymbol{\mu}_{k|k-1}\right)^{-\frac{3}{2}} \\
& \left(\boldsymbol{\mu}_{k|k-1}^T \boldsymbol{A}^T \boldsymbol{A}\right) \left(\boldsymbol{\mu}_{k|k-1}^T \boldsymbol{A}^T \hat{\boldsymbol{A}} \boldsymbol{\mu}_{k|k-1}\right) + \\
& \left(\boldsymbol{\mu}_{k|k-1}^T \boldsymbol{A}^T \boldsymbol{A} \boldsymbol{\mu}_{k|k-1}\right)^{-\frac{1}{2}} \\
& \boldsymbol{\mu}_{k|k-1}^T \left(\boldsymbol{A}^T \hat{\boldsymbol{A}} + \hat{\boldsymbol{A}}^T \boldsymbol{A}\right),
\end{aligned} \tag{2.43}$$

where $\boldsymbol{\mu}_{k|k-1}$ is the estimated mean of the world-frame position.

2.6 Simulation Results

This section is outlined as follows:

Section 2.6.1 reports simulation results of cooperative acoustic navigation utilizing a kinematic model **with** a DVL comparing acoustic range-only observations to acoustic range and acoustic range-rate observations.

Section 2.6.2 reports simulation results of cooperative acoustic navigation utilizing a kinematic model **without** a DVL comparing acoustic range-only observations to acoustic range and acoustic range-rate observations.

2.6.1 Results utilizing a DVL

We conducted numerical simulations to investigate the effect of range-rate observations on the performance of the CEKF cooperative navigation algorithm described in Section 2.3. We computed a true simulated vehicle path and simulated data for each of the navigation sensors by generating simulated measurements with the measurement-noise characteristics given in Table 2.1. In the simulation presented here, the vehicle conducted a simulated survey mission of ten 1 km track lines spaced 100 m apart with a vehicle advance velocity of 2 knots and a depth of 3 m. The ship circled continuously on a 300 m radius at a velocity of 1.5 knots broadcasting acoustic packets every minute. The speed of sound was assumed constant at 1500 m/s throughout the simulation.

Figure 2.2 shows the true and estimated XY vehicle position from the CEKF utilizing acoustic range observations with the filter's covariance plotted at 60 s intervals. Figure 2.3 shows the true and estimated XY vehicle position estimate from the CEKF utilizing acoustic range and range-rate observations with the filter's covariance plotted at 60 s intervals. In both figures, the arrows point from the vehicle to the ship along acoustic path with the length scaled by the angle from vertical.

Figures 2.4 and 2.5 shows histograms of the error in the X- and Y-directions, with acoustic range and acoustic range and range-rate observations, respectively. These histograms indicate the noise statistics may not be unimodal in X-direction and may not be zero-mean in the Y-direction. However, the variability of the simulation noise in disparate

Table 2.1: Vehicle state measurement sources, resolutions, and accuracies

State	Source	Update Rate	Measurement Std Dev
XY Trans	modem	60 s	1m (range) 0.1m/s (range rate)
Z Trans	Paroscientific	7 Hz	6 cm
Heading	OCTANS	3 Hz	0.10°
Pitch, Roll	OCTANS	3 Hz	0.05°
Trans Velocity	300 kHz RDI DVL	5 Hz	0.01 m/s
Ang Vel	OCTANS	3 Hz	0.4-0.6°/s

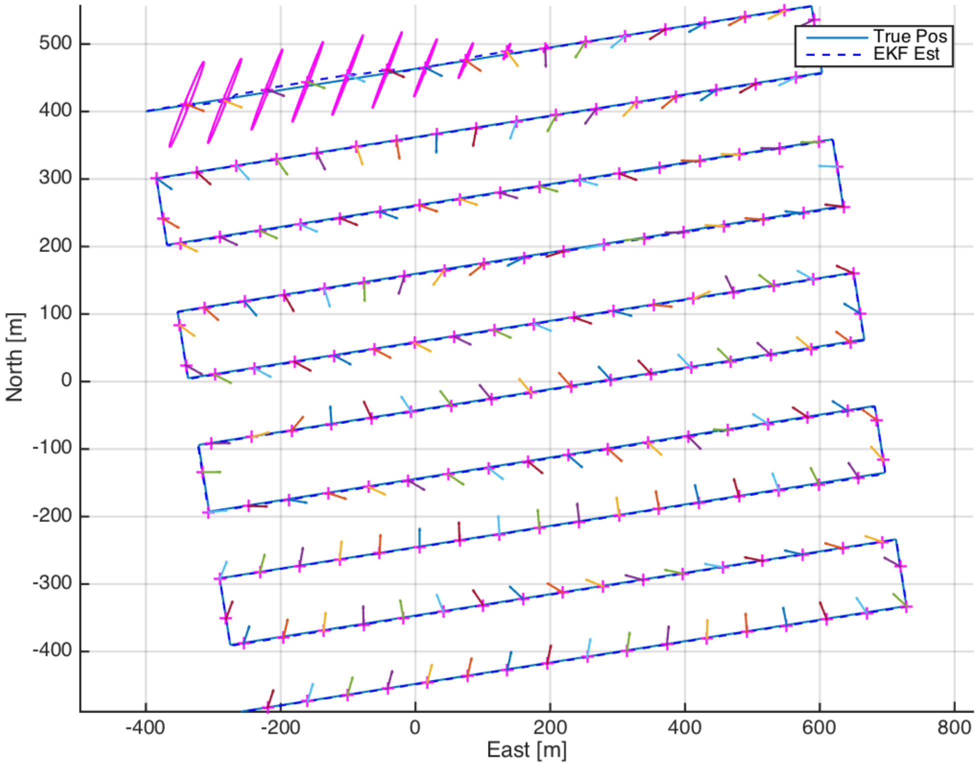

Figure 2.2: Vehicle XY position estimate from the CEKF cooperative acoustic navigation on simulated data with acoustic range observations. The true position is plotted as a solid blue line, the CEKF position estimate is plotted as a dashed blue line with covariance ellipses plotted at acoustic TOA with an arrow pointing along the acoustic path.

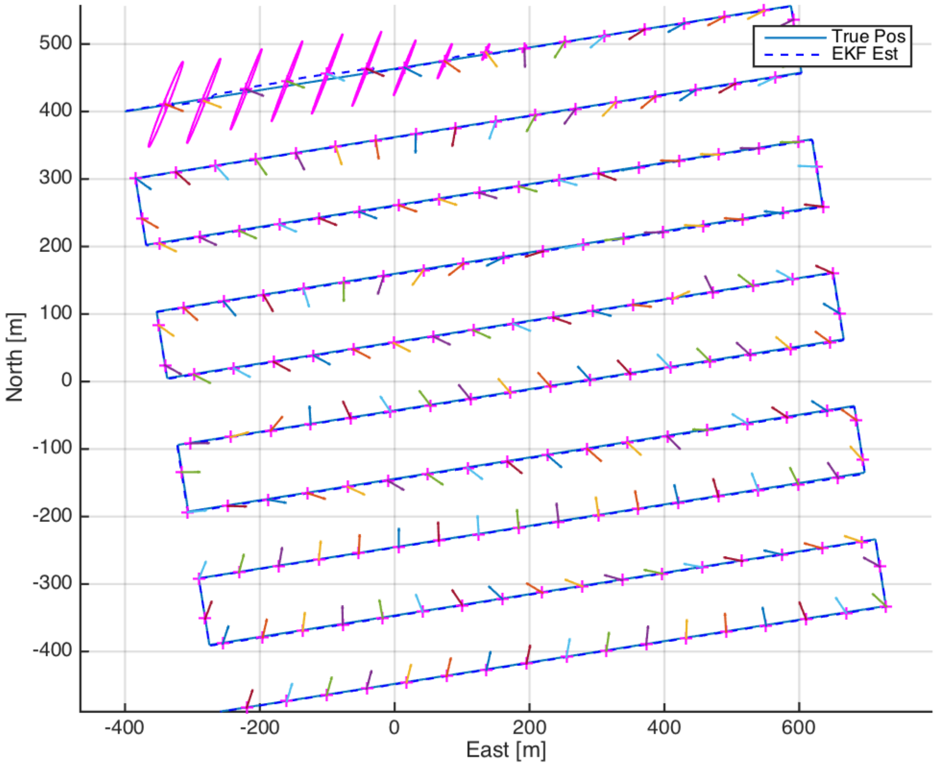

Figure 2.3: Vehicle XY position estimate from the CEKF cooperative acoustic navigation on simulated data with acoustic range and acoustic range-rate observations. The true position is plotted as a solid blue line, the CEKF position estimate is plotted as a dashed blue line with covariance ellipses plotted at acoustic TOA with an arrow pointing along the acoustic path.

realizations prevents us from drawing broad conclusions based on these results alone.

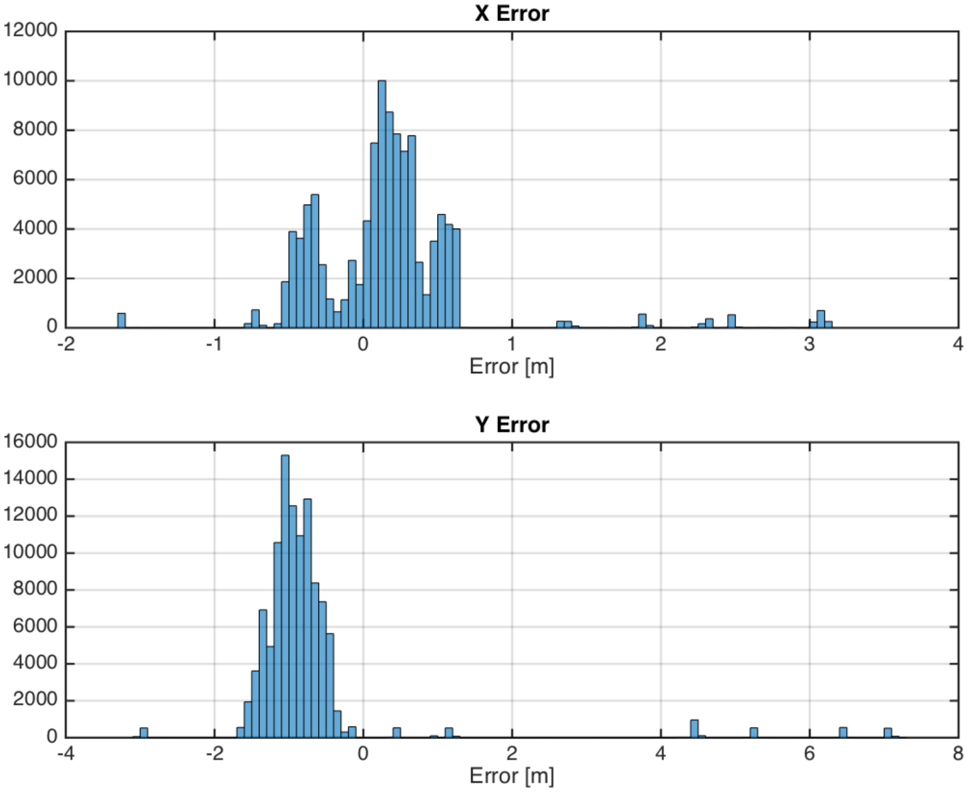

Figure 2.4: Error histogram in the X- and Y-directions from the CEKF in simulation using the kinematic model and DVL with acoustic range observations. The figure indicates the noise statistics may not be unimodal in the X direction and may not be zero-mean in the Y direction.

Figure 2.6 shows the XY error magnitude, i.e., the magnitude of the difference between the EKF-estimated and true XY position, for both range-only and combined range and range-rate observations. It should be noted that all other simulated measurements were held constant during this comparison; the only change was the addition of range-rate observations.

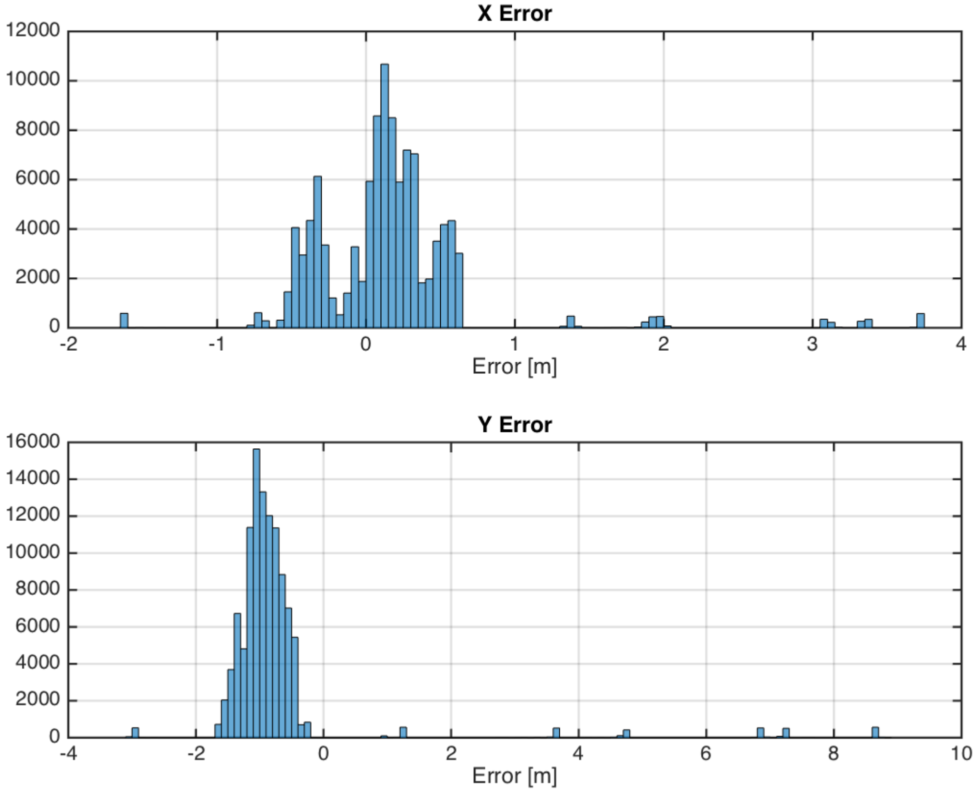

Figure 2.5: Error histogram in the X- and Y-directions from the CEKF in simulation using the kinematic model with DVL with acoustic range and acoustic range-rate observations. The figure indicates the noise statistics may not be unimodal in the X direction and may not be zero-mean in the Y direction, and that the addition of range-rate observations does not appear to impact the error histogram.

Figure 2.6: XY error magnitude versus mission time from the CEKF on simulated data with the kinematic model and a DVL. The navigation error from the CEKF using acoustic range-only observations is plotted in black, and the navigation error from the CEKF using acoustic range and acoustic range-rate observations is plotted in blue. This figure indicates that the addition of acoustic range-rate observations to acoustic range observations may not offer a significant advantage to the performance of the CEKF using a kinematic model with a DVL.

For the kinematic process model described in Section 2.4 and the observation models described in Section 2.5, the addition of range-rate observations does not appear to offer a significant improvement in CEKF performance with a DVL on this simulated survey mission when utilizing high-accuracy velocity and attitude sensors and reasonable range and range-rate noise statistics.

2.6.2 Results without utilizing a DVL

In this preliminary study, we utilized numerical simulations to investigate the effect of the range-rate observation on the performance of the centralized extended Kalman filter (CEKF) cooperative navigation algorithm described in Section 2.3.

We computed simulated vehicle and ship trajectories and simulated sensor data for each of the navigation sensors by generating simulated measurements with the measurement-noise characteristics outlined in Table 2.2. As discussed later in this section, the sensor for attitude and angular rate reported in Table 2.2 and used in these simulation results is unrealistically accurate, and the navigation performance of the CEKF using the kinematic model without a DVL appears to depend on the accuracy of the attitude sensor.

In the simulation presented here, the vehicle conducts a simulated survey mission of ten 1 km track lines spaced $100\ \mathrm{m}$ apart at a velocity of 1 m/s and a depth of $3\ \mathrm{m}$. The ship circles continuously on a $800\ \mathrm{m}$ radius at a velocity of 2 m/s broadcasting acoustic packets every 10 seconds. The speed of sound was assumed constant at 1500 m/s.

Figure 2.7 shows the true and estimated XY vehicle position from the CEKF utilizing

Table 2.2: Vehicle state measurement sources, resolutions, and accuracies

State	Source	Update Rate	Measurement Std Dev
XY Trans	modem	10 s	variable (range) 0.1m/s (range rate)
Z Trans	Paroscientific	7 Hz	6 cm
Heading	OCTANS	3 Hz	0.10°
Pitch, Roll	OCTANS	3 Hz	0.05°
Ang Vel	OCTANS	3 Hz	0.4-0.6°/s

acoustic range measurements with the filter's covariance plotted every 60 s. Figure 2.8 shows the true and estimated two-dimensional vehicle position from the CEKF utilizing acoustic range and range-rate measurements with the filter's covariance plotted every 60 s. In both figures, the arrows point from the vehicle to the ship with the length scaled by the angle of the acoustic path from vertical.

Figures 2.9 and 2.10 show histograms of the estimation error (i.e., the difference between the estimated vehicle position and the true vehicle position) in the X- and Y-directions. These histograms indicate the X- and Y- estimation errors of the CEKF are approximately zero-mean and Gaussian.

Figure 2.11 shows the XY error magnitude, i.e., the magnitude of the difference between the EKF-estimated and true XY position, for both range-only and combined range

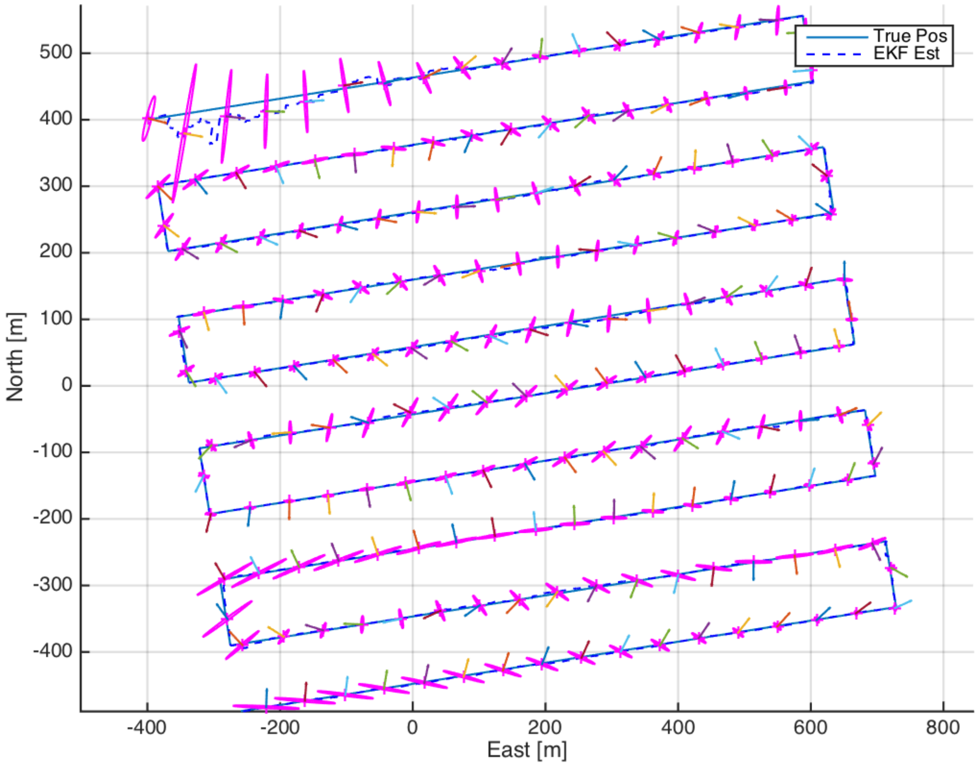

Figure 2.7: XY vehicle position estimate from the CEKF on simulated data using the kinematic model and no DVL with a high-accuracy attitude and angular-rate sensor using acoustic range only observations. The CEKF using a kinematic model without a DVL exhibits poor performance and even instability in simulation when the vehicle is equipped with an attitude sensor typical of low-cost UVs.

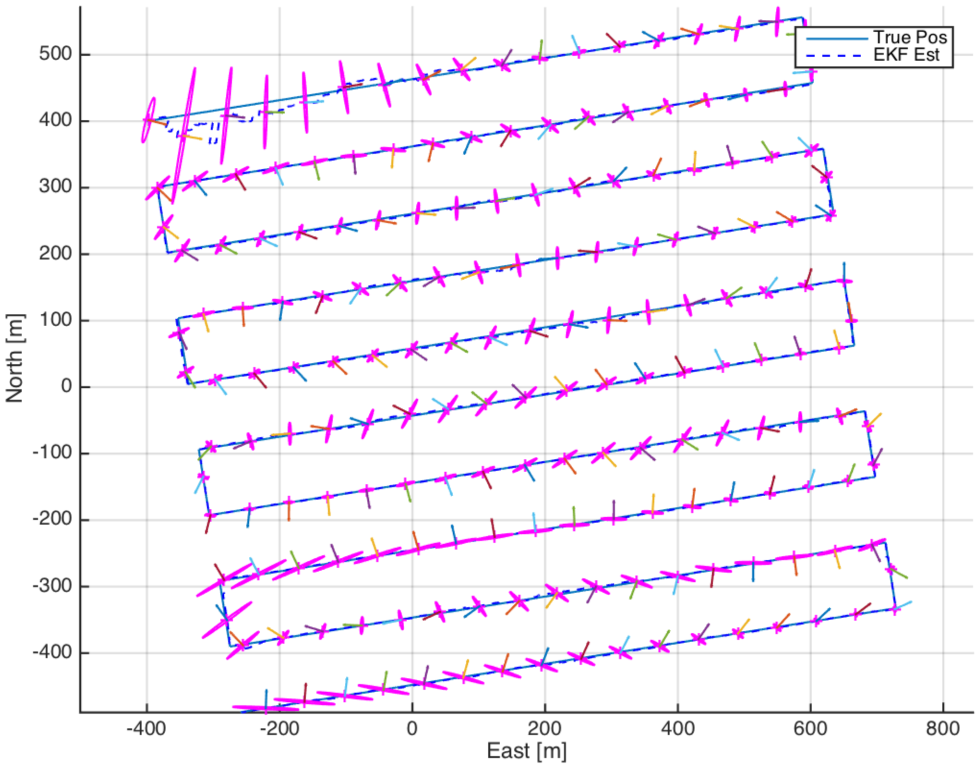

Figure 2.8: XY vehicle position estimate from the CEKF on simulated data using the kinematic model and no DVL with a high-accuracy attitude and angular-rate sensor using acoustic range and acoustic range-rate observations. This figure indicates that the addition of range-rate observations may not significantly improve the performance of the CEKF. As with the previous figure, the CEKF using a kinematic model without a DVL exhibits poor performance and even instability in simulation when the vehicle is equipped with an attitude sensor typical of low-cost UVs.

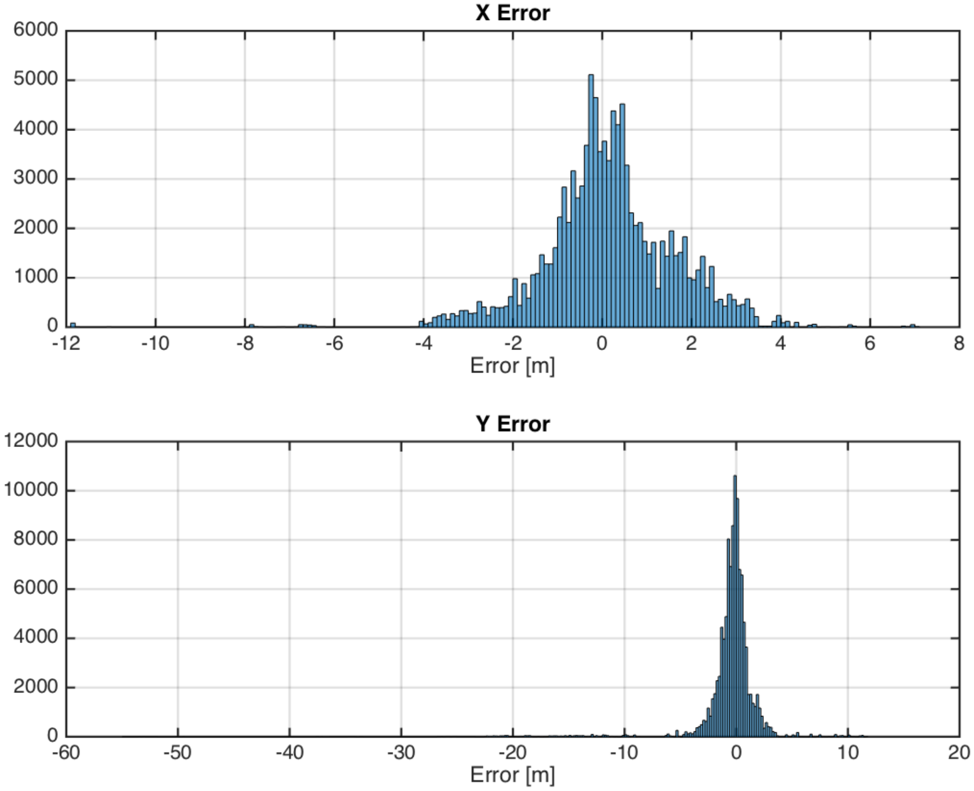

Figure 2.9: Error histogram in the X- and Y-directions from the CEKF using kinematic model without DVL and high-end attitude and angular-rate sensor with acoustic range-only observations. This figure indicates that the error statistics are approximately zero-mean and Gaussian.

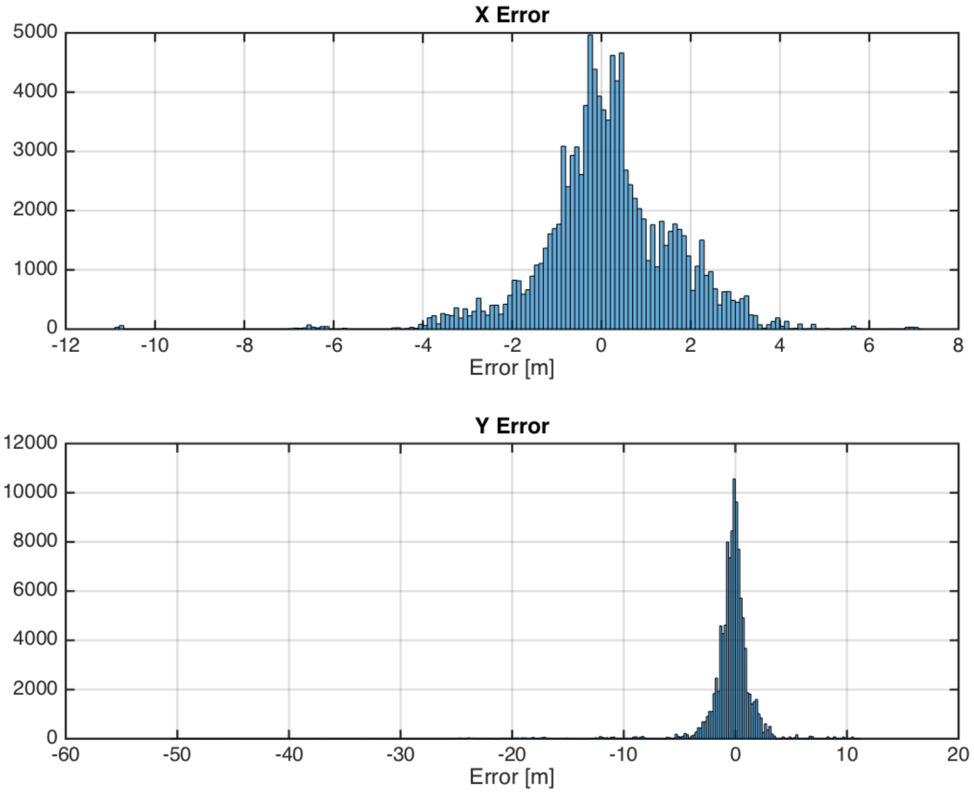

Figure 2.10: Error histogram in the X- and Y-directions from the CEKF using kinematic model without DVL and high-end attitude and angular-rate sensor with acoustic range and acoustic range-rate observations. This figure indicates that the error statistics are approximately zero-mean and Gaussian.

and range-rate observations. It should be noted that all other simulated measurements were held constant during this comparison; the only change was the addition of range-rate observations.

For the kinematic process model described in Section 2.4 and the observation models described in Section 2.5, the addition of range-rate observations does not appear to offer a significant improvement in CEKF performance in the absence of a DVL on this simulated survey mission when utilizing high-accuracy attitude and depth sensors with reasonable range and range-rate noise statistics.

We investigated in simulation the performance of this cooperative navigation approach for the case when the underwater vehicle has degraded range measurements. Poor acoustic range measurements could be caused by inaccuracies in the speed of sound characterization, timing errors in the precision clocks, or the lack of precision clocks altogether. Figure 2.12 shows the XY error magnitude for both range-only and combined range and range-rate observations for noisy range measurements. For the noise statistics and geometry reported here, the addition of range-rate observations appears to offer modest improvements in the steady-state response and a significantly smaller error in the transient response of CEKF compared to range-only navigation.

Additionally, we considered the situation where the CEKF was subject to an initialization error on the order of $150\ \mathrm{m}$. For the cases we examined, the addition of range-rate observations did not appear to significantly improve the convergence time, transient response, or steady-state error of the CEKF.

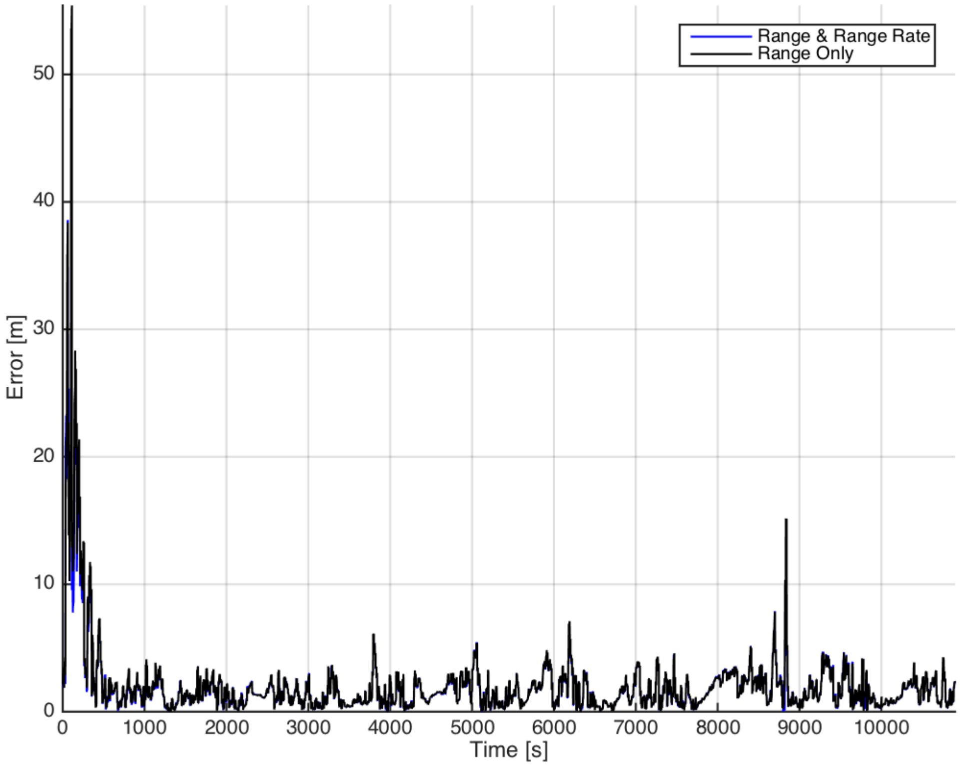

Figure 2.11: XY error magnitude of the CEKF on simulated data using the kinematic model and a high-accuracy attitude and angular-rate sensor without a DVL with acoustic range-only and acoustic range-rate observations as a function of mission time. The navigation error of the CEKF using range-only observations is plotted in black, and the navigation error of the CEKF using range-only observations is plotted in blue. As noted previously, the CEKF goes unstable with a kinematic model and no DVL when the UV is equipped with an attitude sensor typically available on a low-cost UV, and these results are only valid when using a high-end attitude and angular-rate sensor that would typically be too large and expensive for a low-cost UV operating without a DVL. The noise statistics for the acoustic measurements used in this figure are $\sigma_{rng} = 1$ m and $\sigma_{RR} = 0.1$ m/s, which represents the typical accuracy of these measurements. This figure indicates that the addition of acoustic range-rate observations to acoustic range observations does not appear to significantly improve the performance of the CEKF utilizing a kinematic model with a high-accuracy attitude and angular-rate sensor without a DVL.

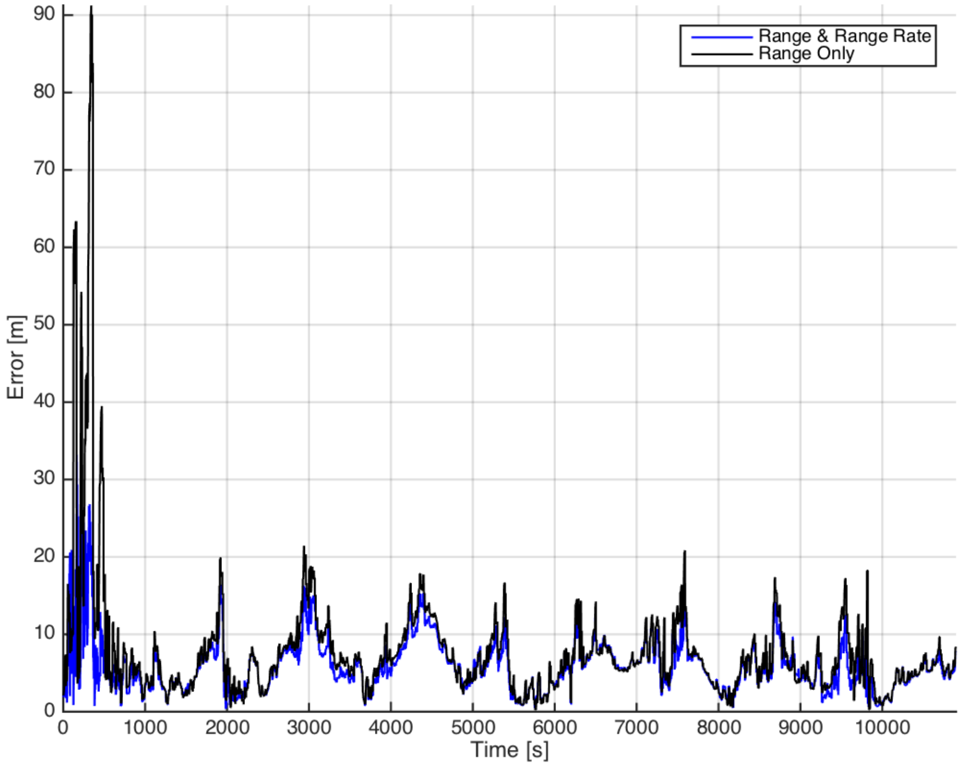

Figure 2.12: XY error magnitude of the CEKF on simulated data using the kinematic model and a high-accuracy attitude and angular-rate sensor without a DVL with acoustic range-only and acoustic range-rate observations as a function of mission time. The navigation error of the CEKF using range-only observations is plotted in black, and the navigation error of the CEKF using range-only observations is plotted in blue. As noted previously, the CEKF goes unstable with a kinematic model and no DVL when the UV is equipped with an attitude sensor typically available on a low-cost UV, and these results are only valid when using a high-end attitude and angular-rate sensor that would typically be too large and expensive for a low-cost UV operating without a DVL. The noise statistics for the acoustic measurements used in this figure are $\sigma_{rng} = 20$ m and $\sigma_{RR} = 0.1$ m/s, which represent poor acoustic range measurements and accurate acoustic range-rate measurements. There are several realistic scenarios that could result in poor range measurements without affecting the range-rate measurements, such as inaccurate or poorly synchronized clocks or bad estimates of the speed of sound in water. This figure indicates that the addition of acoustic range-rate observations to acoustic range observations may improve the convergence time of the CEKF algorithm utilizing a kinematic model with a high-accuracy attitude and angular-rate sensor without a DVL when the acoustic range measurements are poor.

Note that these results are for a UV equipped with a high-end fiber optic gyrocompass (FOG), which is exceptionally accurate, as shown in Table 2.2. However, such an instrument would be unreasonable to install on a low-cost, torpedo-shaped UV for reasons of cost, size, and power.

We attempted to investigate the situation when the UV was not equipped with a high-end gyroscope providing extremely accurate attitude and angular-rate measurements, but instead equipped with a low-end 3-axis compass providing attitude measurements with a standard deviation of 1° in roll, pitch, and heading. However, we discovered the CEKF utilizing a kinematic model and a low-end compass can go unstable in the absence of DVL measurements. This instability and poor performance of the CEKF utilizing a kinematic model with a low-end compass and no DVL are shown in the numerical simulation and experimental results reported in Chapter 3, specifically Figure 3.1 and Figure 3.5. We conjecture this instability is caused by the constant-velocity kinematic process model. The problem of cooperative acoustic navigation of low-cost UVs without a DVL using a dynamic process model is the subject of Chapter 3.

2.7 Summary

This chapter reviews the CEKF formulation of cooperative acoustic navigation, first presented in [84], including the state description, kinematic process models, and observation models. An observation model for acoustic range-rate measurements was developed.

The results presented in Section 2.6 show that the addition of range-rate observations to acoustic range observations does not appear to significantly improve the convergence time, transient response, or steady-state error of the CEKF with or without a DVL. We investigated the situation when the acoustic range measurements are poor but the acoustic range-rate measurements are still valid and concluded that range-rate observations may offer modest improvements in the steady-state response and a significantly smaller error in the transient response of CEKF compared to range-only navigation in this scenario.

We also observed instability of the CEKF when utilizing the kinematic UV process model with a low-end attitude sensor and no DVL. We conjecture this instability is caused by the constant-velocity kinematic process model, motivating the use of a dynamic UV process model in the CEKF, which is reported in Chapter 3.

Chapter 3

Cooperative Acoustic Navigation with a Dynamic UV Process Model

This chapter reports the development and simulation plus experimental evaluation of a 6 DOF, second-order nonlinear dynamic UV model for use in the CEKF without a Doppler velocity log. We used JHU's Ocean Server Iver3 AUV (L3 OceanServer, Fall River, MA, USA) to conduct the experimental evaluation.

The idea of using a dynamic process model was motivated by the results in Section 2.6 where we observed poor performance and even instability of the CEKF simulation in certain geometries between the ship and submerged vehicle when using a kinematic model with a low-accuracy attitude sensor without velocity corrections from a DVL.

This chapter is organized as follows:

Section 3.1 details a commonly-used dynamic model for UV motion and describes the particular structure of the parameters used in the results section.

Section 3.2 reports simulation results (3.2.1) and experimental results (3.2.2). Experimental data were collected with the JHU Iver3 AUV deployed in the Chesapeake Bay. There appears to be good agreement between simulation and experimental data, which provides some level of validation of the simulation results.

3.1 Dynamic Model

This section reports the second-order dynamic process model used for cooperative acoustic navigation with out a DVL. The dynamical process model described herein is for a generic UV with diagonal mass and drag matrices; for the control inputs described in 3.1.2.1, we assume the vehicle is torpedo-shaped AUV with a propeller and control surfaces at the aft end. We chose to use diagonal mass and drag matrices because the JHU Iver3 AUV is roughly symmetric about each of the principal axes; the force (hydrodynamic lift and drag) from the fins and propeller are modeled separately so their effect should not considered in the mass or drag matrices.

Additionally, the Iver3 AUV is a torpedo-shaped vehicle and therefore experiences minimal coupling between DOF during forward flight.

The dynamic model of submerged UV motion presented herein applies only when the UV is fully submerged; the model does not account for effects caused by the water's free surface.

3.1.1 State Description

We utilize the same state description detailed in Section 2.3.2, with the addition of ξ as the vector of UV control inputs. For a torpedo-shaped vehicle with k propellers and i aft control surfaces, this is

$$\xi = \left| \begin{matrix} \omega_{p_k} \\ \delta_i \end{matrix} \right| \in \mathbb{R}^{k+i}, \tag{3.1}$$

where ω_{p_k} is angular velocity of the k^{th} propeller and δ_i is the commanded angle of the i^{th} fin.

3.1.2 Dynamic Process Model

The form of the second-order, nonlinear dynamics for an UV is well understood and has been since the 1950s [72]. Several sources develop the equations from first principles, including [24, 58].

$$M\dot{v} + C(v)v + D(v)v + \mathcal{G}(\varphi) = \tau(\varphi, v, \xi), \tag{3.2}$$

where $v \in \mathrm{I\!R}^6$ is a vector containing the linear and angular body velocity, $v = |v_1 v_2 v_3 v_4 v_5 v_6|^T$. For convenience, we define the body linear velocity $\nu = |v_1 v_2 v_3|^T \in \mathrm{I\!R}^3$ and the body angular velocity $\omega = |v_4 v_5 v_6|^T \in \mathrm{I\!R}^3$. $\dot{v} \in \mathrm{I\!R}^6$ is the time derivative of body velocity, $\dot{v} = |\dot{v}_1 \dot{v}_2 \dot{v}_3 \dot{v}_4 \dot{v}_5 \dot{v}_6|^T$. The vector φ is the body attitude vector.

We combine the kinematics, (2.23) and (3.2) in state-space representation for use in the

CEKF

$$\dot{x}_v = \begin{bmatrix} 0 & K(\varphi) \\ 0 & -M^{-1}\big(D(x_v) + C(M, x_v)\big) \end{bmatrix} x_v \; + \begin{vmatrix} 0 \\ M^{-1}\big(\tau(x_v, \xi) - \mathcal{G}(x_v)\big) \end{vmatrix} + \begin{vmatrix} 0 \\ \mathbb{I} \end{vmatrix} w_v, \tag{3.3}$$

where

- $K(\varphi) : \mathbb{R}^3 \to \mathbb{R}^{6\times 6}$ is the kinematics matrix, as defined in Section 2.4,
- $M \in \mathbb{R}^{6\times 6}$ is the positive definite symmetric (PDS) inertia matrix,
- $D(x_v) : \mathbb{R}^6 \to \mathbb{R}^{6\times 6}$ is the negative definite symmetric (NDS) hydrodynamic drag matrix,
- $C(x_v) : \mathbb{R}^6 \to \mathbb{R}^{6\times 6}$ is the centripetal and Coriolis matrix,
- $\tau(x_v, \xi) : \mathbb{R}^6 \times \mathbb{R}^{k+i} \to \mathbb{R}^6$ is a vector of the forces and moments from the control inputs,
- $\mathcal{G}(\varphi) : \mathbb{R}^3 \to \mathbb{R}^6$ is a vector of restoring forces and moments, and
- $w_v \sim \mathcal{N}(0, Q_v)$ and $w_s \sim \mathcal{N}(0, Q_s)$ are zero-mean Gaussian process noise terms.

The inertia matrix, M, is a positive definite symmetric (PDS) matrix composed of the sum of the rigid-body inertia and added inertia.

$$M = M_{RB} + M_A = \begin{bmatrix} M_{11} & M_{12} \\ M_{21} & M_{22} \end{bmatrix} \tag{3.4}$$

$$= \text{diag}(m, m, m, I_{xx}, I_{yy}, I_{zz}) + \text{diag}(X_{\dot{u}}, Y_{\dot{v}}, Z_{\dot{w}}, K_{\dot{p}}, M_{\dot{q}}, N_{\dot{r}}) \tag{3.5}$$

$$= \text{diag}(m_{11}, m_{22}, m_{33}, m_{44}, m_{55}, m_{66}) \tag{3.6}$$

The drag matrix, $D(x_v)$, is a negative definite symmetric (NDS) matrix composed of the product of the quadratic drag coefficients and their respective velocities, i.e.,

$$\begin{aligned} D(x_v) &= -\,\text{diag}(X_{u|u|}|u|, Y_{v|v|}|v|, Z_{w|w|}|w|, K_{p|p}|p|, M_{q|q}|q|, N_{r|r}|r|) \\ &= \text{diag}(|v|)\ \text{diag}\Big([d_{11}, d_{22}, d_{33}, d_{44}, d_{55}, d_{66}]\Big) \end{aligned} \tag{3.7}$$

In constructing this drag matrix, we assume that there is no coupling between DOFs, that the vehicle is symmetric about the x, y, and z axes, and that linear drag terms have a small effect compared to their quadratic counterparts, which is discussed in [51]. Note that the drag matrix inherently captures the effects of what many authors refer to as *body lift*. The diagonal terms d_{22} and d_{33} correspond to a body lift force in the y and z directions, respectively.

We parameterize the Coriolis matrix $C(M, v)$ from M as

$$C(M, v) = \begin{bmatrix} 0 & -J\left(M_{11}\nu + M_{12}\omega\right) \\ -J\left(M_{11}\nu + M_{12}\omega\right) & -J\left(M_{21}\nu + M_{22}\omega\right) \end{bmatrix} \tag{3.8}$$

where $J()$ is the skew-symmetric operator.

The buoyancy vector, $\mathcal{G}(\varphi)$, is defined as

$$\mathcal{G}(\varphi) = \begin{vmatrix} R^T(\varphi)e_3 g_c g \\ -J(b)R^T(\varphi)\rho\nabla g_c, \end{vmatrix} \tag{3.9}$$

where $e_3 = \begin{vmatrix} 0 & 0 & 1 \end{vmatrix}^T \in \mathbb{R}^3$, $g_c \in \mathbb{R}^3$ is the gravitational acceleration scalar with units of m/s^2, $g = (m - \rho\nabla) \in \mathbb{R}^3$ is the net buoyancy (i.e., wet weight) in kilograms, and $b \in \mathbb{R}^3$ is the vector from the center of buoyancy to the center of gravity in meters.

3.1.2.1 Control Inputs

We must define the nonlinear function that maps the vehicle's control inputs, ξ, into forces and moments on the vehicle. To start, we define the following frames for each fin:

- V – Vehicle frame
- F – Fin frame at commanded angle, δ, with the x-axis along the chord line of the fin and the y-axis pointing away from the center line of the vehicle
- F_0 – Fin Frame at $\delta = 0$
- W – Frame corresponding to flow across the fin

Note that the commanded fin angle, δ, is not necessarily the fin's angle of attack to incident flow, α, so the F and W frames are generally not coincident. The position of the center of pressure (CP) of the i^{th} fin in the vehicle frame is ${}^V\boldsymbol{p}_i \in \mathbb{R}^3$ is the vector from the vehicle's center of gravity (CG) to the CP of the i^{th} fin, and ${}^V\boldsymbol{\phi}_i \in \mathbb{R}$ is the angular position of the i^{th} fin in the vehicle frame. We define the transformations between coordinate frames of each fin as

$$ {}^{V}_{F}\boldsymbol{R}_i = {}^{V}_{F_0}\boldsymbol{R}_i \, {}^{F_0}_{F}\boldsymbol{R}_i \in \mathbb{R}^{3\times 3} \tag{3.10} $$

$$ {}^{V}_{W}\boldsymbol{R}_i = {}^{V}_{F}\boldsymbol{R}_i \, {}^{F}_{W}\boldsymbol{R} \in \mathbb{R}^{3\times 3} \tag{3.11} $$

where ${}^{V}_{F}\boldsymbol{R}_i$ is the transformation from the fin frame to the vehicle frame and ${}^{V}_{F}\boldsymbol{R}_i$ is the transformation from the flow frame to the vehicle frame. The individual transformations are defined as

$$ {}^{V}_{F_0}\boldsymbol{R}_i = \boldsymbol{R}_x({}^{V}\boldsymbol{\phi}_i) \tag{3.12} $$

$$ {}^{F_0}_{F}\boldsymbol{R}_i = \boldsymbol{R}_y(\delta_i) \tag{3.13} $$

$$ {}^{F}_{W}\boldsymbol{R}_i = \boldsymbol{R}_y^T(\alpha_i), \tag{3.14} $$

where (3.12) is assumed because, for the vehicle used in Section 3.2 (and many other UVs), the x-axis of the fin frame aligns with the x axis of the vehicle frame. The velocity of the i^{th} fin through the water at the fin CP in vehicle coordinates is

$$ {}^{V}\dot{\boldsymbol{p}}_i = v + J(\omega)\, {}^{V}\boldsymbol{p}_i. \tag{3.15} $$

Next, we rotate the velocity into the fin frame F

$$ {}^{F}\dot{\boldsymbol{p}}_i = {}^{V}_{F}\boldsymbol{R}_i^T \, {}^{V}\dot{\boldsymbol{p}}_i. \tag{3.16} $$

Assuming flow along the span of the airfoil does not affect the lift or drag, we use a projection matrix to find the flow along the x and z axes

$$ {}^{F}\dot{\boldsymbol{p}}_{xz_i} = \begin{bmatrix} 1 & 0 & 0 \\ 0 & 0 & 0 \\ 0 & 0 & 1 \end{bmatrix} {}^{F}\dot{\boldsymbol{p}}_{i}, \tag{3.17} $$

from which we can find the angle of attack, α, as

$$ \alpha_i = \text{atan2}\left(\frac{-{}^{F}\dot{\boldsymbol{p}}_{z_i}}{{}^{F}\dot{\boldsymbol{p}}_{x_i}}\right), \tag{3.18} $$

where atan2 is the four-quadrant arctangent function. The lift and drag coefficients, $C_L(\alpha_i)$ and $C_D(\alpha_i)$, respectively, are a function of the angle of attack. We then compute the hydrodynamic lift and drag force

$$ L(\alpha_i) = \frac{1}{2}\rho A C_L(\alpha_i)||{}^{F}\dot{\boldsymbol{p}}_{xz_i}||^2 \tag{3.19} $$

$$ D(\alpha_i) = \frac{1}{2}\rho A C_D(\alpha_i)||{}^{F}\dot{\boldsymbol{p}}_{xz_i}||^2, \tag{3.20} $$

where A is the surface area of the fin. The force vector in the flow frame, W, is ${}^{W}\mathbf{f} = -\begin{vmatrix} D & 0 & L \end{vmatrix}^T$. Thus, the force vector from the i^{th} fin in the vehicle frame is

$$ {}^{V}\mathbf{f}_i = {}^{V}_{W}\boldsymbol{R}_i \; {}^{W}\mathbf{f}_i \;, \tag{3.21} $$

and the force and moment vector from is

$$ \boldsymbol{\tau}_i = \begin{vmatrix} {}^{V}\mathbf{f}_i \\ J({}^{V}\boldsymbol{r}_i) \; {}^{V}\mathbf{f}_i \end{vmatrix}. \tag{3.22} $$

The total force and moment vector on the vehicle with a total of N control surfaces is thus

$$ \boldsymbol{\tau} = \sum_{i}^{N} \boldsymbol{\tau}_i + \begin{vmatrix} \beta_p \omega_p^2 & \mathbf{0}_{1\times 5} \end{vmatrix}^T, \tag{3.23} $$

where β_p is the propeller thrust coefficient such that

$$T = \beta_p \omega_p^2 \tag{3.24}$$

is the axial thrust of the propeller. This simplified thruster model is a reasonable assumption because we are modeling a ducted propeller with a high jet velocity compared to the advance velocity of the vehicle.

3.1.3 Trackline-Following Controller

For UVs performing large-area survey missions, it is common for the operator to specify in advance an XY "lawnmower pattern" of survey lines for the vehicle to follow while maintaining constant depth or terrain-following in the Z-dimension. Moreover, survey-class underwater vehicles are often underactuated and must vary their pitch and heading, respectively, to achieve a desired depth or translational position. Thus, this problem is not the conventional robotics trajectory-tracking problem in which the desired position and velocity is completely parametrized a-priori as a function of time. In the simulations, we implemented a commonly employed approach to trackline following: a proportional controller to compute the forward thrust and a proportional derivative (PD) controller to compute the fin angles required to follow the trackline. In the experimental data, JHU's Ocean Server Iver3 AUV used a proprietary controller provided by the manufacturer, with the recorded propeller speed and four fin position.

3.1.3.1 Error Coordinates

We define the error coordinates as

$$\boldsymbol{e} = \boldsymbol{s}_e - \boldsymbol{s}_d \tag{3.25}$$

$$\dot{\boldsymbol{e}} = \dot{\boldsymbol{s}}_e - \dot{\boldsymbol{s}}_d = \boldsymbol{R}(\boldsymbol{\varphi}_e)\boldsymbol{\nu}_e - \boldsymbol{R}(\boldsymbol{\varphi}_d)\boldsymbol{\nu}_d, \tag{3.26}$$

where $s \in \mathbb{R}^3$ is the 3 DOF position (as defined in Section 2.3.2) and the subscript e denotes the value estimated by the CEKF and the subscript d denotes the value desired by the trajectory-generation algorithm.

Next, we find the unit vector along the direction of the trackline and use a projection matrix to obtain the direction perpendicular to the trackline

$$\boldsymbol{u}_{ct} = \begin{bmatrix} 0 & -1 & 0 \\ 1 & 0 & 0 \\ 0 & 0 & 0 \end{bmatrix} \frac{\dot{\boldsymbol{s}}_d}{||\dot{\boldsymbol{s}}_d||_2}. \tag{3.27}$$

The crosstrack error is the inner product of the crosstrack and alongtrack unit vectors, respectively, and the error is

$$d_{ct} = \boldsymbol{u}_{ct}^T \boldsymbol{e} \tag{3.28}$$

$$d_z = \begin{vmatrix} 0 & 0 & 1 \end{vmatrix}^T \boldsymbol{e}. \tag{3.29}$$

3.1.3.2 PD Controller

We use Dana Yoerger's *kappa* algorithm to compute the reference pitch and heading.

$$\psi_r = \psi_d - \kappa_\psi d_{ct} \tag{3.30}$$

$$\theta_r = \theta_d - \kappa_\theta d_z, \tag{3.31}$$

where κ, i.e., the angle at which the vehicle drives towards the track line, is saturated in pitch and heading at ±30° and ±45°, respectively. The rate of change of the reference heading, $\dot{\psi}_r$, and the reference pitch, $\dot{\theta}_r$, are both assumed zero.

We used a PD control law to compute desired pitch moment and yaw moment, respectively

$$M_{y_d} = K_{p_y}\left(\theta_r - \theta_e\right) + K_{d_y}\left(\dot{\theta}_r - q_e\right) \tag{3.32}$$

$$M_{z_d} = K_p\left(\psi_r - \psi_e\right) + K_d\left(\dot{\psi}_r - r_e\right) \tag{3.33}$$

where, as defined in Section 2.3.2, θ is the pitch, ψ is the heading, p and r are the vehicle's heading and pitch rate, respectively, in body coordinates, K_p is the proportional gain, and K_d is the derivative gain.

To compute the desired thrust, we used a proportional control law on the difference between the desired and estimated velocity, and we feed forward the total drag on the vehicle in the x-direction, which yields

$$F_{x_d} = K_p\left(u_d - u_e\right) - \begin{vmatrix} 1 \\ 0_{5\times 1} \end{vmatrix}^T \left[\Big(\boldsymbol{C}(v) + \boldsymbol{D}(v)\Big)v - \sum_{i=1}^{N} \boldsymbol{\tau}_i\right], \tag{3.34}$$

where, again as defined in Section 2.3.2, u is the body velocity in the x direction and $\boldsymbol{\tau}_i$ is the sum of the fin forces, as defined in (3.22).

3.1.4 Fin Allocation Algorithm

To find the desired angle for each fin, we used a nonlinear constrained optimization algorithm to minimize the difference between the actual and desired moment on the vehicle. For simplicity, we assumed the desired pitch and yaw moments were decoupled from roll, i.e., that the vertical fins influence only the yaw moment and the horizontal fins influence only the pitch moment. Note that this assumption was only used for determining the desired fin angles; the achieved fin moment was computed for each fin individually using the current state, as described in Section 3.1.2.1. This simple algorithm has the obvious disadvantage that if the vehicle is substantially rolled while turning, the horizontal fins will contribute to the yaw moment, but the fin allocation algorithm will not use them to achieve the desired yaw moment. We did implement and evaluate an algorithm for fin allocation in 6 DOF, but we found there is a substantial penalty in computational efficiency. The run time for simulations with 6 DOF fin allocation was 2-10x longer with only marginally better performance than the decoupled approach described previously. For this reason, we chose to employ the decoupled approach in the simulation results reports in Section 3.2.1.

3.2 Results for Cooperative Acoustic Navigation with a Dynamic UV Model

This section reports results from a numerical simulation and experimental data collected with the JHU Iver3 AUV operating in the Chesapeake Bay. The centralized extended Kalman filter (CEKF) formulation of cooperative acoustic navigation was used to post-process the simulated and experimental data. Comparisons between the kinematic plant-process model and dynamic plant-process model without a DVL are drawn.

3.2.1 Simulation Results: Cooperative Acoustic Navigation with a Dynamic UV Process Model Utilizing Acoustic Range Only Observations

First, we utilized a numerical simulation to investigate the effect of the dynamic model on the performance of the CEKF formulation of cooperative navigation algorithm described in Section 2.3. We simulated a submerged vehicle with feedback control following a continuous reference trajectory. We generated simulated sensor data for each of the navigation sensors with the measurement-noise characteristics outlined in Table 3.1. These simulated data were then post-processed with a CEKF to compare the kinematic and dynamic process models.

Table 3.1: Simulation measurement sources, resolutions, and accuracies for use in cooperative acoustic navigation simulations

State	Source	Update Rate	Measurement Std Dev
XY Trans	modem	30 s	1 m (range) 0.1m/s (range rate)
Z Trans	Paroscientific	7 Hz	6 cm
Heading, Pitch, Roll	Iver3 compass	3 Hz	1°
Trans Velocity	300 kHz RDI DVL	5 Hz (when used)	0.01 m/s (when used)

In the simulation presented here, the vehicle conducted a simulated survey mission of ten $1\ \mathrm{km}$ tracklines spaced $100\ \mathrm{m}$ apart at a velocity of $1\ \mathrm{m/s}$ and a constant depth of $3\ \mathrm{m}$. The ship circled continuously on a $600\ \mathrm{m}$ radius at a velocity of $2\ \mathrm{m/s}$ broadcasting the first acoustic packet after $60\ \mathrm{s}$, and then regularly at $30\ \mathrm{s}$ intervals. The speed of sound was assumed constant at $1500\ \mathrm{m/s}$.

Figures 3.1 and 3.2 show the true and estimated XY vehicle position with the kinematic model and the dynamic model, respectively, with the filter's covariance plotted at every acoustic update. The arrows point from the vehicle to the ship along acoustic path with the length scaled by the angle from vertical.

Fig. 3.3 shows the XY error magnitude, i.e., the magnitude of the difference between the EKF-estimated and true position, for the dynamic model without the DVL, the kine-

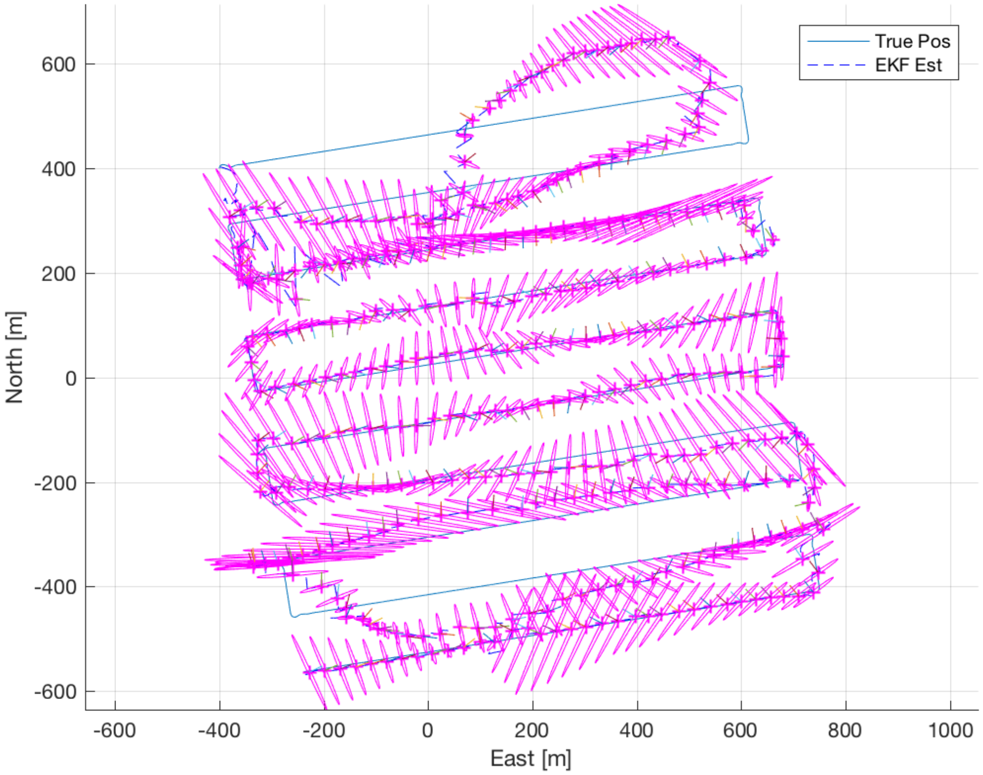

Figure 3.1: Vehicle XY Position from CEKF cooperative acoustic navigation algorithm using the kinematic model without a DVL and noise sensors similar to that of the JHU Iver3 AUV. Note that the position estimate is very poor with the kinematic model and no DVL when using an attitude sensor typically available on low-cost UVs.

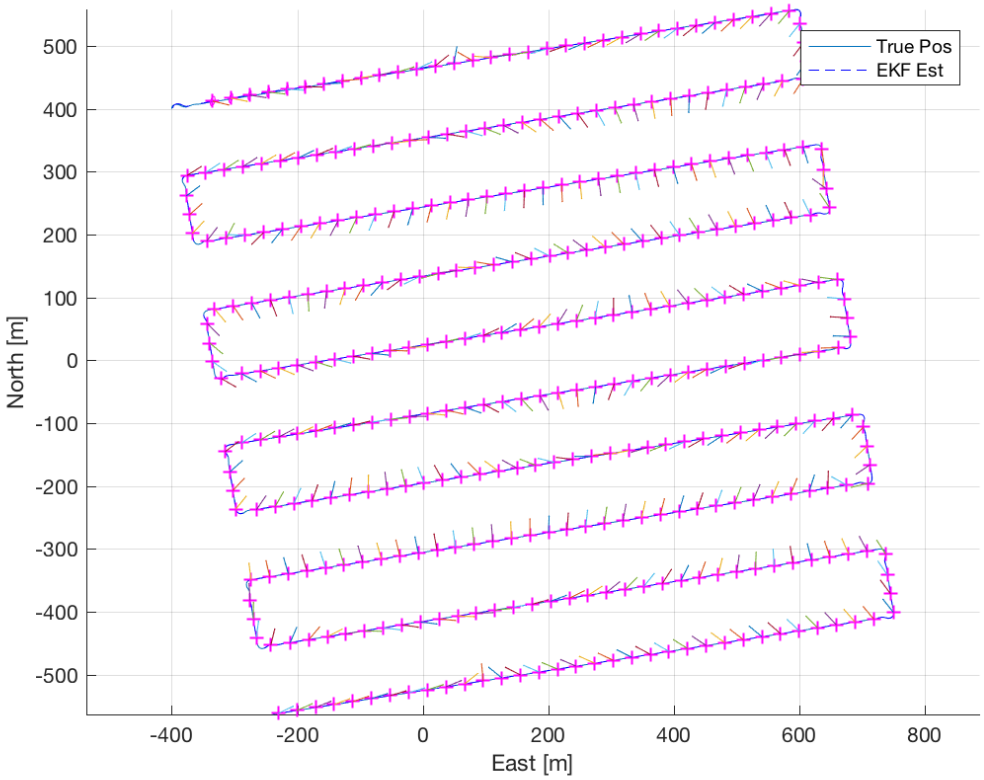

Figure 3.2: Vehicle XY Position from CEKF cooperative acoustic navigation algorithm using the dynamic model without a DVL and noise sensors similar to that of the JHU Iver3 AUV. When the vehicle does not have access to a DVL and is using an attitude sensor typically available on low-cost UVs, the CEKF with the dynamic model performs quite well and does not exhibit the instabilities seen with the CEKF utilizing the kinematic model.

matic model without the DVL, the kinematic model with the DVL, and the vehicle dead reckoning (DR) with the compass and DVL. All initial conditions and simulated measurements, when used, were held constant in this comparison.

For the noise statistics and geometry reported herein, and the observation models described in Section 2.5, the dynamic UV model appears to offer a significant improvement in CEKF navigation performance in the absence of a DVL on this simulated survey mission when utilizing attitude and depth sensors with realistic noise statistics. In fact, the simulation suggested that the navigational accuracy of the CEKF with dynamic model may even perform on par with that of the CEKF with kinematic model and DVL in the absence of ambient water currents. However, the simulation does not account for various real-world phenomena, so we validated the simulation by collecting experimental data.

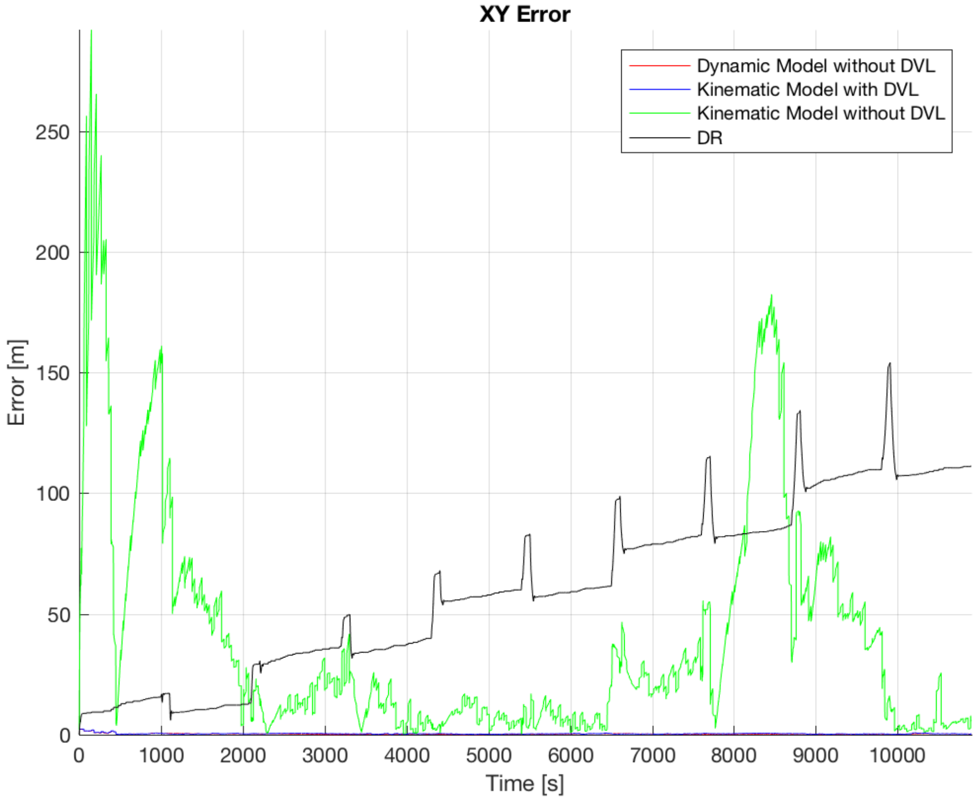

Figure 3.3: Simulated XY Error magnitude versus mission time. The error with the kinematic model with the DVL and the dynamic model without the DVL is quite small in comparison, less than 5 meters, so it is hard to see those two signals. We conclude that the dynamic model without a DVL offers a significant advantage over the kinematic model without a DVL and it may outperform the DR solution, especially as mission length increases. Note that this simulation was conducted without environmental disturbances, such as water currents.

3.2.2 Experimental Results: Cooperative Acoustic Navigation with a Dynamic UV Process Model Utilizing Acoustic Range Only Observations

Following the encouraging results of the simulation, we conducted a set of preliminary experiments to evaluate this navigation approach in actual practice with JHU's Iver3 AUV (L3 OceanServer, Fall River, MA, USA), shown in Fig. 3.4, in the Chesapeake Bay.

This section reports experimental results for cooperative acoustic navigation comparing the navigation performance of the CEKF utilizing a dynamic UV process model without a DVL to the kinematic process model with and without a DVL.

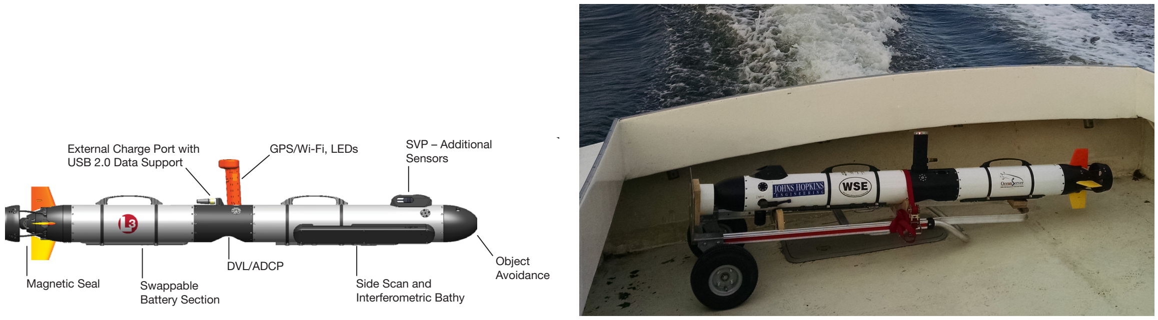

(a) Iver3 general diagram (Image Credit: L3 OceanServer).

(b) JHU Iver3-3026 about to be deployed from a small boat.

Figure 3.4: The Iver3 AUV is an underactuated AUV whose control authority is provided by the commanded rotational speed of its ducted propellor and commanded angles for the four red/yellow fins, all located at the stern of the vehicle. The 100 m depth-rated Iver3 is one of a number of commercially available small AUVs designed for oceanographic survey operations including biological, physical-oceanographic, and hydrographic survey missions.

3.2.2.1 Experiment Particulars

Table 3.2 lists the noise characteristics of the sensors on board the JHU Iver3 AUV. We also used the Iver3-reported commanded motor speed and commanded fin angles in the model described in Section 3.1. For this experiment, the Iver3 was programmed to run a lawnmower pattern with six $300\ \mathrm{m}$ legs spaced $50\ \mathrm{m}$ at a $2.5\ \mathrm{m}$ depth traveling at an advance velocity of $1.3\ \mathrm{m/s}$. The surface ship and the Iver3 AUV were each equipped with 25 kHz WHOI Micromodems [70], each equipped with precision Microsemi Quantum chip-scale atomic clocks (Microsemi Corporation, Aliso Viejo, CA, USA) and a precision-timing GPS units to synchronize the clocks to GPS UTC time. Vehicle and ship modems were programmed to repeat the 30-second time-division multiple access (TDMA) cycle listed in Table 3.3. The realtime location of the surface ship's modem transducer was instrumented with a GPS unit located vertically above the acoustic modem's transducer.

Table 3.2: JHU Iver3 measurement sources, resolutions, and accuracies used in the CEKF post-processing of experimental data

State	Source	Update Rate	Measurement Std Dev
XY Trans	modem	60 s	1 m
Z Trans	OceanServer	1 Hz	0.1 m
Hdg, Pitch, Roll	OceanServer	1 Hz	1°
Trans Velocity	300 kHz RDI DVL	5 Hz (when used)	0.01 m/s (when used)

Table 3.3: Acoustic Modem TDMA Cycle

Time	Action
00 s	OWTT data packet+range uplink AUV to Ship
05 s	OWTT data packet+range downlink Ship to AUV
10 s	OWTT data packet+range downlink Ship to AUV
15 s	OWTT data packet+range downlink Ship to AUV
20 s	TWTT range ping AUV to Ship, with Ship to AUV reply
30 s	Begin new TDMA cycle

3.2.3 Dynamic Model Parameters

We tuned the parameters for the dynamic model by hand so the translational velocities of the model would match the translational velocities reported by the DVL, especially in the x-direction. We report principled methods for estimating the dynamic-model parameters in Chapter 4.

3.2.3.1 Experimental Results

Fig. 3.6 shows the vehicle and ship position estimates from the CEKF algorithm with the dynamic UV process model without the DVL. Fig. 3.5 shows the vehicle and ship position estimates from the CEKF algorithm with the purely kinematic process model without the DVL. Fig. 3.7 shows the estimated vehicle and ship position for the “gold standard” case of a vehicle equipped with DVL and where the CEKF employed a kinematic process model. For these three plots, the solid line is the waypoint trackline the vehicle attempted to follow, the dashed line is the CEKF position estimate of the Iver3 AUV, the dotted line is the CEKF position estimate of the surface ship, and the red triangle is the first valid GPS fix after the vehicle surfaced.

The vehicle position estimate arising from the kinematic process model without a DVL is extremely poor, while the position estimate utilizing the dynamic process model without a DVL is similar to the position estimate obtained by the “gold standard” approach of employing a DVL and a kinematic process model.

We note that the CEKF estimate of the submerged vehicle’s position using utilizing either the kinematic process model with DVL and dynamic process model without the DVL diverges from the trackline. We believe this divergence occurs because the vehicle’s true position diverges from the trackline, as evidenced by the position of the CEKF estimate being coincident with the first valid GPS fix, shown in Fig. 3.7.

Given that this is an actual experiment with a submerged vehicle (no GPS), we do not have access to the true vehicle positions and are therefore unable to compare the navigation error—i.e., the difference between the true XY position of the vehicle and the CEKF estimate—of the kinematic model with DVL to that of the dynamic model without the DVL. Fig. 3.8 shows the magnitude of the difference of the XY position between the CEKF utilizing the dynamic model without a DVL and the CEKF utilizing the kinematic

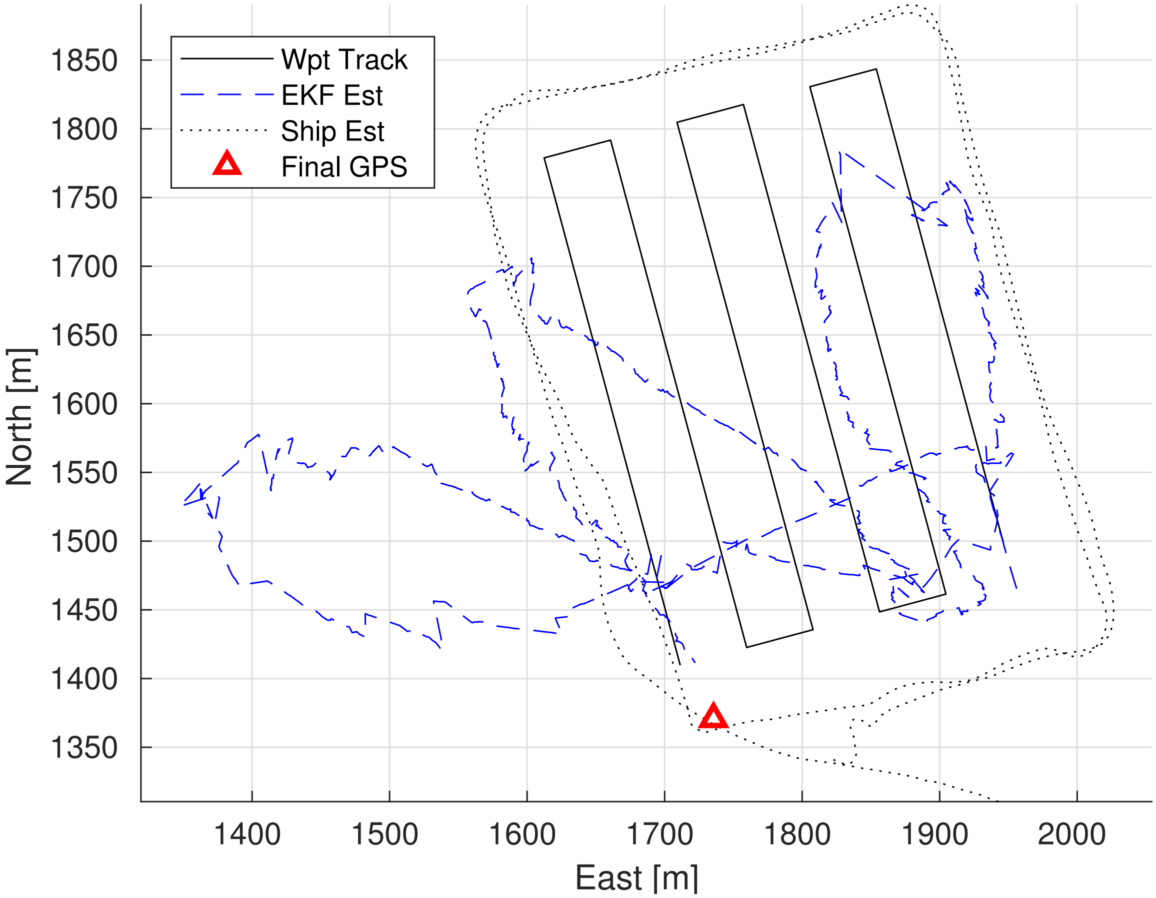

Figure 3.5: Ship and Vehicle XY position estimate from the CEKF without a DVL using the kinematic process model on experimental data collected with the JHU Iver3 AUV in the Chesapeake Bay. The dotted black line is the CEKF estimate of the ship track using GPS, and the dashed blue line is the CEKF estimate in post-processing. The Iver3 AUV attempted to follow a waypoint track, plotted as a solid black line, using its internal DR position estimate and a proprietary closed-loop controller. We conclude that the CEKF goes unstable with a kinematic model in the absence of frequent, high-accuracy velocity observations from a DVL when the vehicle is equipped with an attitude sensor typical of low-cost UVs such as the Iver3 AUV.

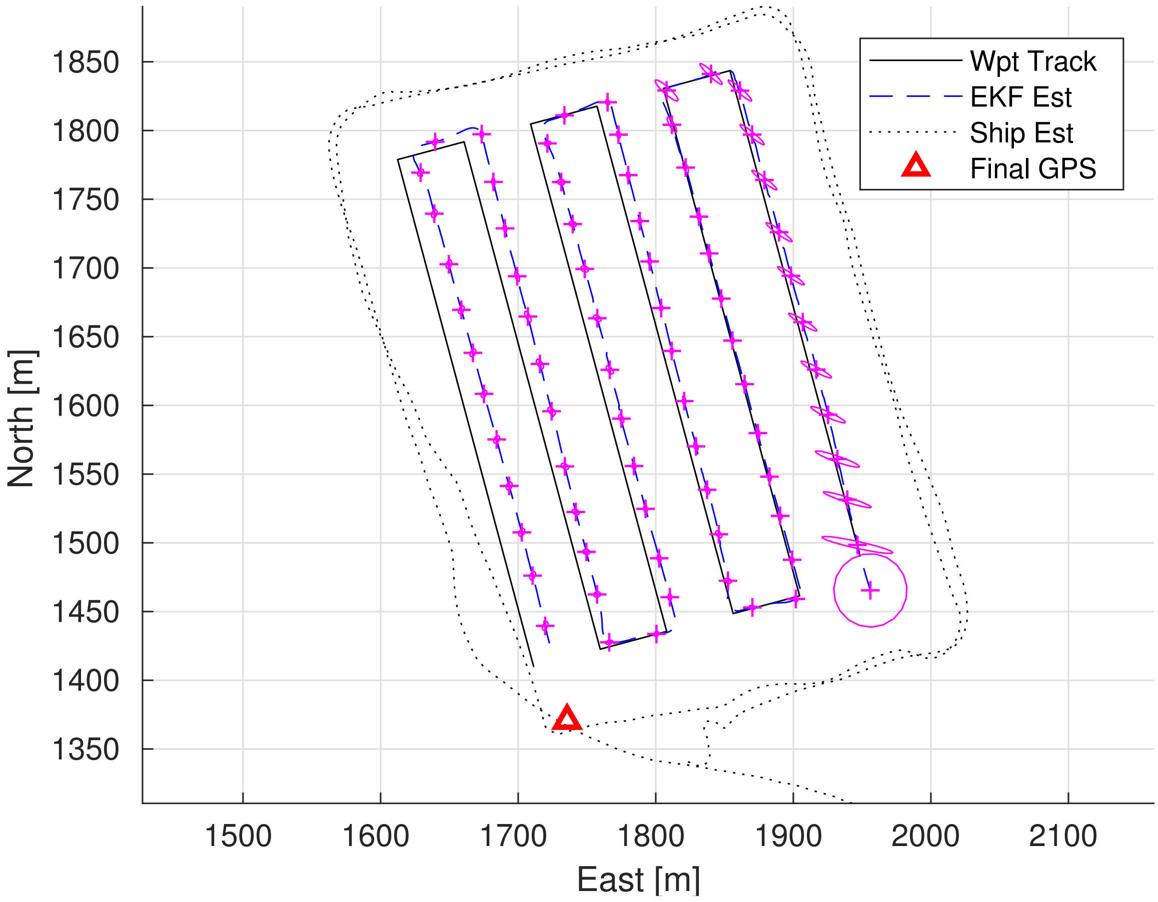

Figure 3.6: Ship and Vehicle XY Position Estimate from the CEKF without a DVL using the dynamic process model on experimental data collected with the JHU Iver3 AUV in the Chesapeake Bay. The dotted black line is the CEKF estimate of the ship track using GPS, and the dashed blue line is the CEKF estimate in post-processing. The Iver3 AUV attempted to follow a waypoint track, plotted as a solid black line, using its internal DR position estimate and a proprietary closed-loop controller. The first valid GPS fix upon surfacing is plotted as a red triangle. When the vehicle is equipped with sensors typical of low-cost UVs such as the Iver3 AUV, the CEKF estimate using a dynamic model without a DVL offers a stable position estimate, in contrast to the kinematic model without a DVL. The true position track is not the solid line, and we believe the vehicle's actual location was not on the trackline. As a measure of validity, the CEKF position estimate is coincident with the Iver3 AUV GPS fix upon surfacing.

model with a DVL, as well as the magnitude of the difference of the XY position between the Iver3-reported dead-reckoned (DR) track and the CEKF utilizing the kinematic model with a DVL. We omitted the CEKF estimate using kinematic model without a DVL for reasons of plot scale and readability.

3.2.4 Experimental Results: Cooperative Acoustic Navigation with a Dynamic UV Process Model Utilizing Acoustic Range and Acoustic Range-Rate Observations

In Section 2.6, we concluded that the addition of range-rate observations to acoustic range observations does not significantly improve the accuracy of the CEKF algorithm with a kinematic process model, either with a DVL (2.6.1) or without a DVL (2.6.2). In this section, we revisit the effect of adding acoustic range-rate observations to acoustic range observations on the navigation solution of the CEKF algorithm with a dynamic process model without a DVL.

As in Section 3.2.2, because this is an actual experiment with a submerged vehicle (no GPS), we do not have access to the true vehicle positions via a separate external positioning system, such as LBL, so we are unable to calculate the actual navigation error (i.e., the magnitude of the distance to the *true* XY vehicle position) of the CEKF. Instead, we use

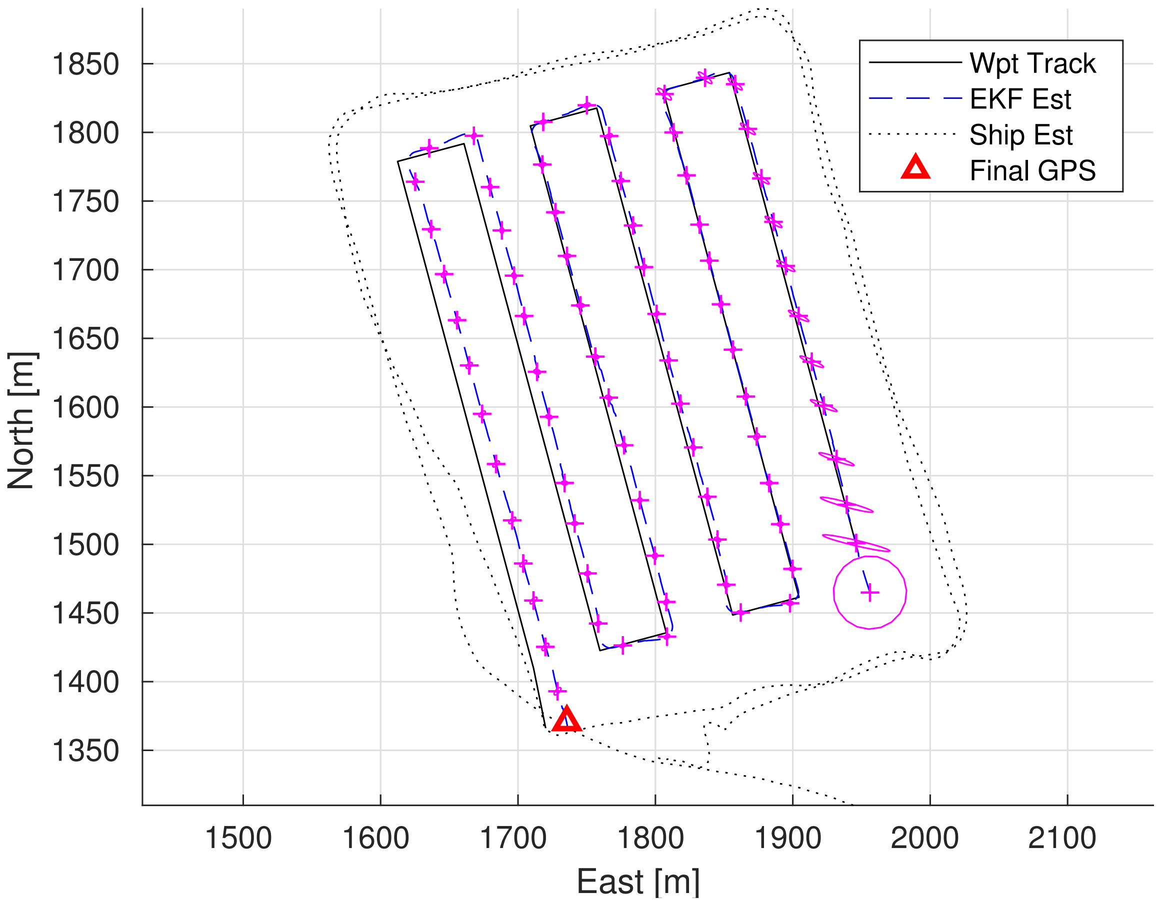

Figure 3.7: Ship and Vehicle XY Position Estimate from the CEKF with a DVL using the kinematic process model on experimental data collected with the JHU Iver3 AUV in the Chesapeake Bay. The dotted black line is the CEKF estimate of the ship track using GPS, and the dashed blue line is the CEKF estimate in post-processing. The Iver3 AUV attempted to follow a waypoint track, plotted as a solid black line, using its internal DR position estimate and a proprietary closed-loop controller. The first valid GPS fix upon surfacing is plotted as a red triangle. When the vehicle is equipped with sensors typical of low-cost UVs such as the Iver3 AUV, the CEKF estimate using a dynamic model without a DVL offers a stable position estimate, in contrast to the kinematic model without a DVL. The true position track is not the solid line, and we believe the vehicle's actual location was not on the trackline. As a measure of validity, the CEKF position estimate is coincident with the Iver3 AUV GPS fix upon surfacing.

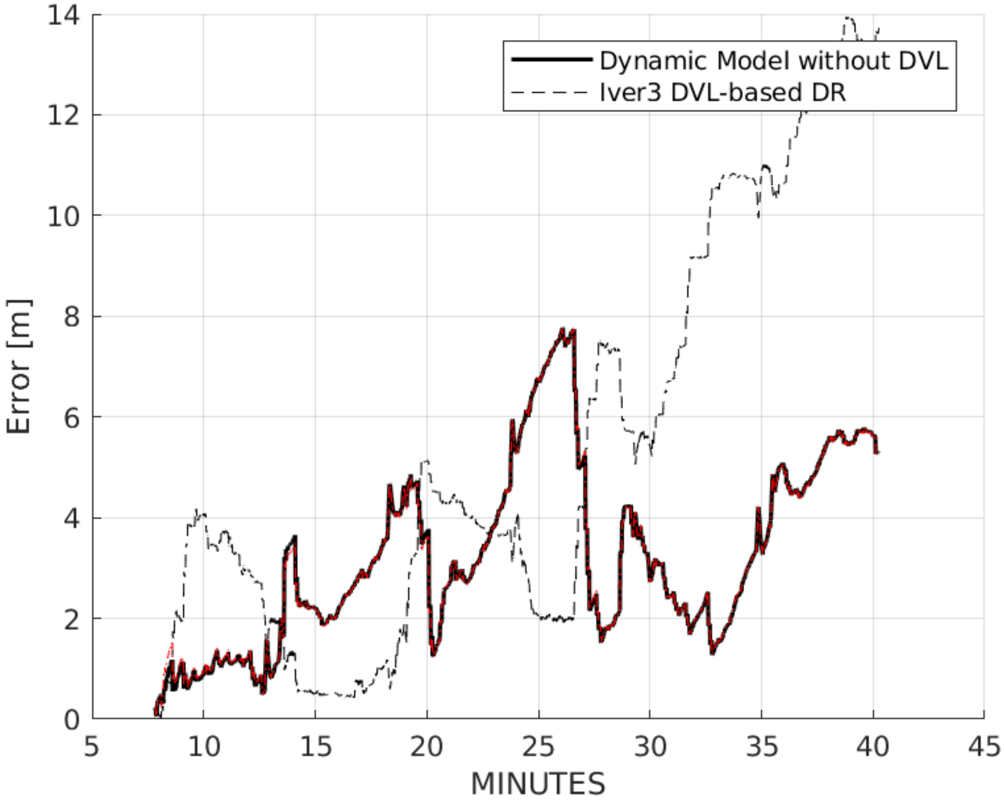

Figure 3.8: XY Position Error Magnitude from CEKF with kinematic model and DVL. We do not have access to true position underwater, so we use the difference from the previous gold standard which is the CEKF estimate using the kinematic model with the DVL. For scale and readability reasons, the unstable CEKF estimate using the kinematic model without the DVL is omitted from the figure. This figure shows that the CEKF position estimate with a dynamic model without a DVL performs quite well and stays within 8 m of the CEKF position estimate using the kinematic model with a DVL. The figure also illustrates the advantage of cooperative acoustic navigation in providing bounded-error position estimates, even without a DVL, compared to dead reckoning.

the previous “gold standard” of the CEKF utilizing the kinematic model with a DVL as the “truth” because it is the closest signal we have to truth and it is independent of the dynamic model; henceforth all mentions of navigation error are relative to this standard.

Fig. 3.9 compares the navigation error of the CEKF utilizing the dynamic model without a DVL with and without the range-rate observations. Fig. 3.9 indicates that the addition of range-rate observations adds little value in the presence of accurate range observations and a dynamic process model with accurate model coefficients, low process noise, and minimal external disturbances, namely water currents.

Similar results are achieved with variations on the process noise and model parameters. Fig. 3.10 reports the error with the process noise doubled, and Fig. 3.11 reports the error with the mass and quadratic drag coefficients accurate to within 95% of the original values. Note that the magnitude of the ambient water-current velocity was small during these reported experiments.

We note the following observations:

First, the CEKF covariance associated with the ship velocity must be lower than the UV’s velocity covariance, otherwise the relative-velocity correction is applied to the surface vessel’s velocity, rather than the submerged vehicle’s velocity.

Second, and perhaps most importantly, the velocity covariance of a purely kinematic model will, in absence of observations to correct position and/or velocity errors, grow unbounded with time, but the velocity covariance of a dynamical model with quadratic drag, (3.2), will converge to a steady-state value that depends on the process noise. Infrequent

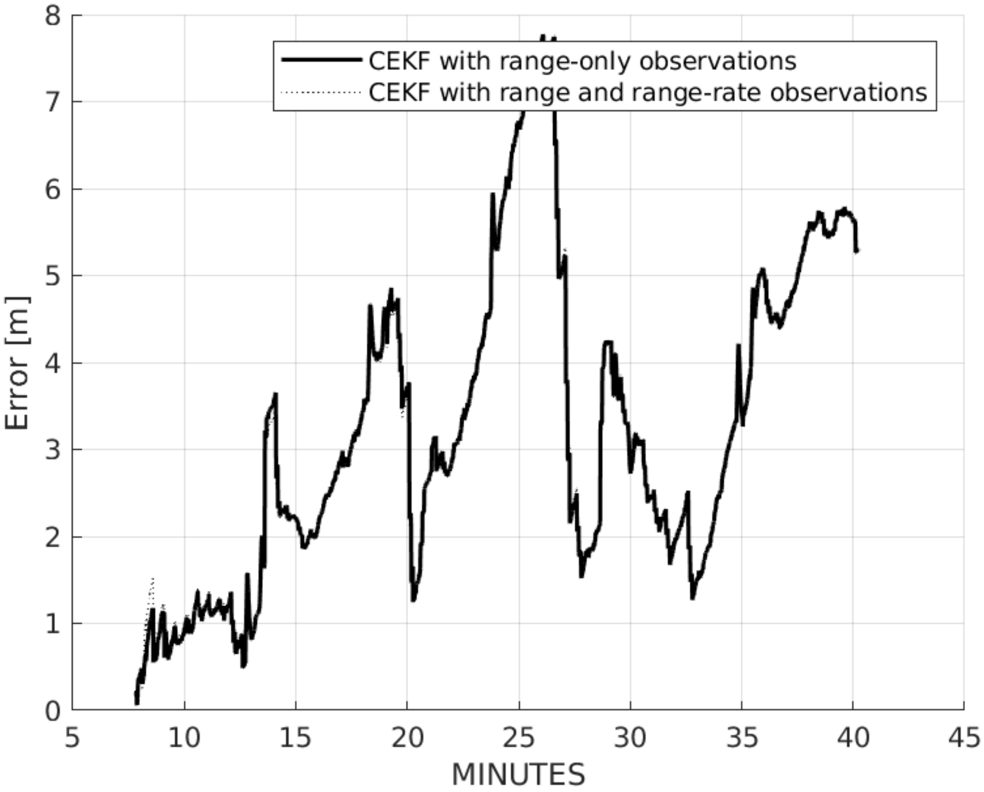

Figure 3.9: XY Position Error Magnitude from the CEKF with dynamic model and no DVL using experimental data collected with the Iver3 AUV. The purpose of this graph is to compare the position estimate using acoustic range and range-rate to the CEKF using acoustic range-only observations. The two signals are indistinguishable, indicating the addition of acoustic range-rate observations to acoustic range observations does not significantly improve the navigation solution from the CEKF with a dynamic model without velocity observations from a DVL.

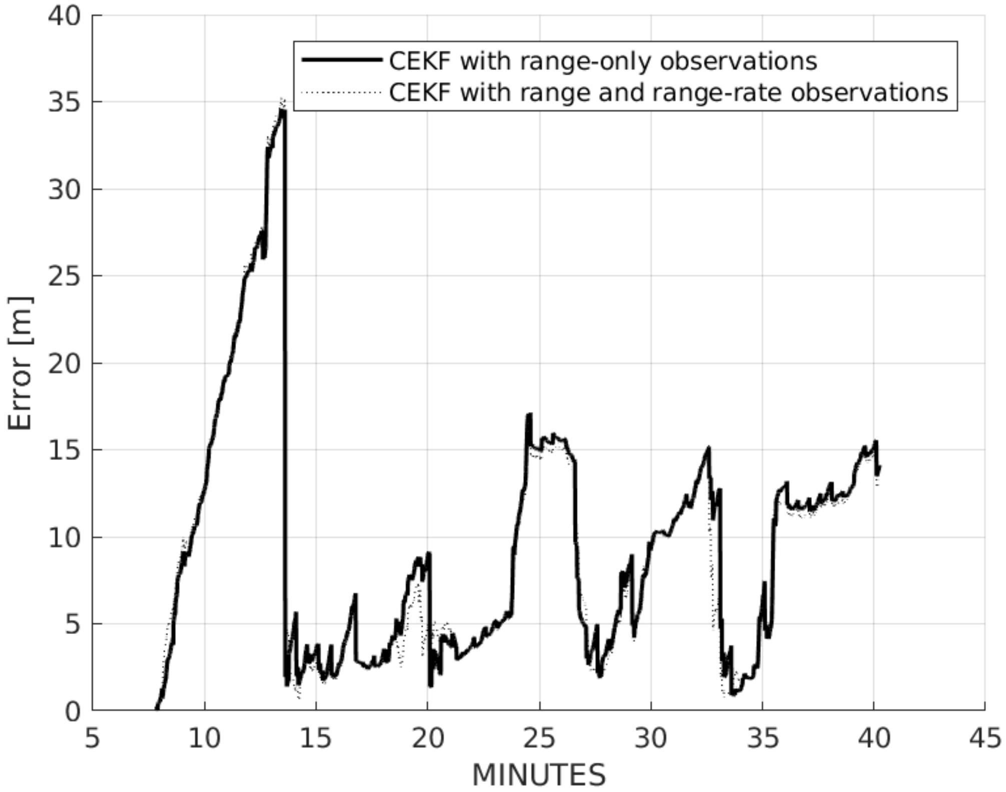

Figure 3.10: XY Position Error Magnitude from the CEKF with dynamic model **utilizing high process noise** and no DVL using experimental data collected with the Iver3 AUV. The purpose of this graph is to compare the position estimate using acoustic range and range-rate to thta using acoustic range-only observations in the context of high process noise in the CEKF. The two signals are indistinguishable, indicating the addition of acoustic range-rate observations to acoustic range observations does not significantly improve the navigation solution from the CEKF with a dynamic model using a high process-noise value without velocity observations from a DVL.

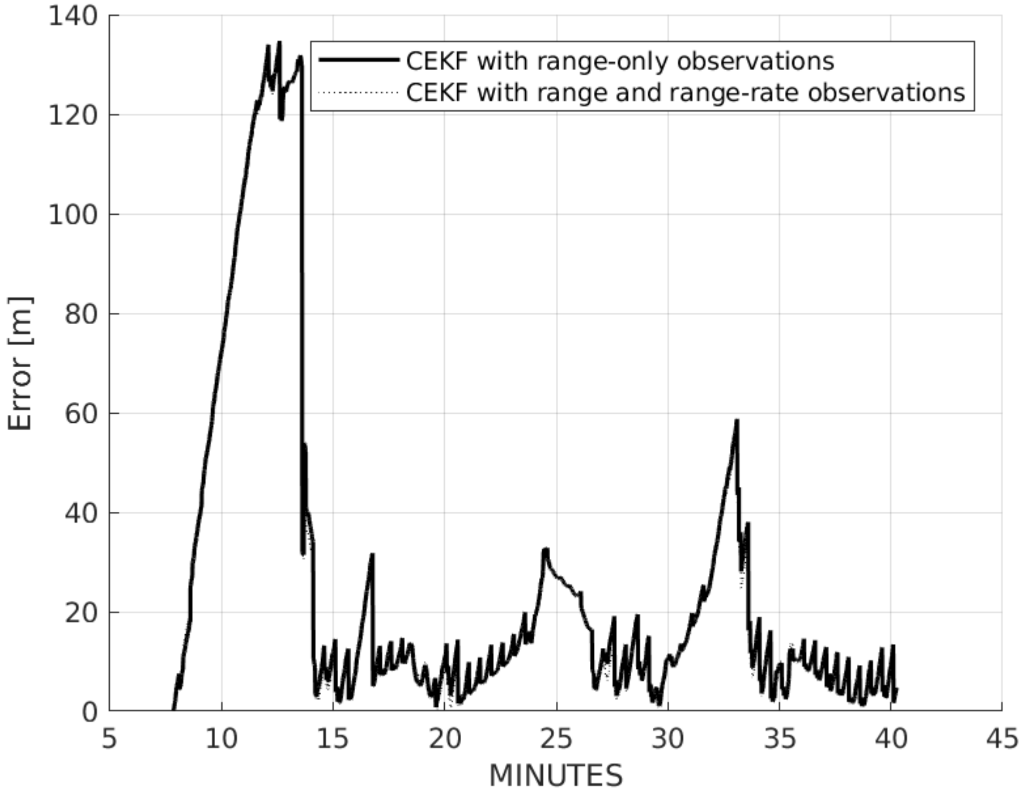

Figure 3.11: XY Position Error Magnitude from the CEKF with dynamic model **with model coefficients that have a random error with a standard deviation of 5% of the true model-parameter value** and no DVL using experimental data collected with the Iver3 AUV. The purpose of this graph is to compare the position estimate using acoustic range and range-rate to the CEKF using acoustic range-only observations in the context of high process noise in the CEKF. The two signals are indistinguishable, indicating the addition of acoustic range-rate observations to acoustic range observations does not significantly improve the navigation solution from the CEKF with a dynamic model using degraded model coefficients without velocity observations from a DVL. A second key point is how poor the error is with minor model inaccuracies.

velocity corrections will have little net effect—velocity observations with a measurement covariance lower than the velocity covariance that are applied infrequently will shrink the covariance at instant the measurement is applied but the velocity covariance rapidly returns to its steady-state value. However, when operating in areas with high ambient water currents, it is possible that range-rate observations may help with the estimation of a velocity-bias term, if such a term were included in the CEKF state. Estimating ambient water currents as a bias term included in the CEKF state is a potential area for future research.

3.3 Summary

This chapter detailed a second-order nonlinear dynamical model of UVs, including a development of the nonlinear actuation function to map the commanded fin angle and propeller speed to an overall force-moment vector on the UV, for use in cooperative acoustic navigation of UVs without a DVL.

Simulation and experimental results were reported utilizing the JHU Iver3 AUV. The results suggest that a dynamic model without a DVL outperforms a kinematic model without a DVL and may outperform DVL-based dead reckoning when the magnitude of the water-current velocity is small. The experimental results appear to corroborate the simulation effort, lending validity to the simulation for future research.

We note, however, that the accuracy of the CEKF navigation solution utilizing the dynamic UV model without a DVL depends entirely on the accuracy of the dynamical model to estimate the vehicle's velocity, particularly in the forward direction. In the absence of external velocity corrections from a DVL, the CEKF relies entirely on the dynamic UV model for velocity predictions. The ability of the dynamic process model to predict the vehicle's velocity depends entirely on the model structure and model parameters. Chapter 4 details two novel approaches to parameter estimation for UV dynamical process models.

Finally, we reported an experimental evaluation of the effect of adding (relative) velocity corrections in the form of acoustic range-rate observations to the CEKF when utilizing a dynamic model without a DVL. We concluded that the addition of infrequent velocity observations, such as those provided by acoustic range rate, does not appear to improve the performance of the CEKF algorithm with a dynamic model.

Chapter 4

Parameter Identification of Dynamic Process Models for Underactuated UVs

Current approaches to model-based navigation, model-based control, and model-based fault detection for UVs are limited by accurate knowledge of the parameters for the dynamic process model employed by the model-based algorithms. While the general form of UV dynamical plant models has been understood since the 1950s [72], the dynamic-model parameters—i.e., parameters for terms including mass, added mass, hydrodynamic drag, buoyancy, and control actuators—are impossible to determine analytically and are not provided by UV manufacturers. Thus, these terms must be determined experimentally.

Our goal is a low-cost, low-effort approach to parameter estimation that can be applied whenever the vehicle configuration is substantially modified. Thus, we attempt to estimate UV parameters from data obtained in full-scale experimental trials of UVs in controlled motion.

Identifying dynamic-model parameters from data obtained in controlled free motion trials requires the UV operate under a control law: either open-loop control or closed-loop control. Closed-loop control has the advantage that the UV will not go unstable (e.g., tumble) and operates in a known trajectory, but 1) it requires a closed-loop controller to be implemented, 2) the UV motion is more gentle, which may not be sufficiently exciting in all DOF, and 3) the control inputs may be saturated, which can indirectly cause problems for the parameter identification algorithms.

Open-loop control, such as a fin angles that are sum of sinusoids utilized here in simulation, has the advantage that more UV motion can be generated, which can be helpful for parameter estimation, and the control inputs are smooth, but has the disadvantage that the vehicle might tumble, run aground, or breach the surface.

For experimental work, which is beyond the scope of this thesis, we would start with the JHU Iver3 AUV using the manufacturer's proprietary closed-loop controller from the frontseat CPU. If there was insufficient motion for the parameters to be uniquely observable, we would try open-loop control by commanding fin angles and propeller rotational speed from the backseat CPU.

Specifically, this chapter addresses parameter identification for UV plants of the form 3.2 rewritten as

$$0 = M\dot{v} + C(v)v + D(v)v + \mathcal{G}(\varphi) - \tau(\varphi, v, \xi), \tag{4.1}$$

This chapter is organized as follows:

Section 4.1 reviews the literature on parameter identification of UV in controlled free motion.

Section 4.2 reports noise statistics on the instruments available on the JHU Iver3 AUV.

Section 4.3 reports a novel least-squares based algorithm, termed nullspace-based least squares (NBLS), for identifying simultaneously the plant parameters and the actuator parameters for second-order, underactuated, rigid-body UV plants in 6 DOF. Simulation results, including a noise sensitivity analysis, are reported. Anecdotal simulation results applying an estimated parameter vector to cooperative acoustic navigation are also included. This work was first published in [31]. Coauthor Tyler Paine contributed to the development of the NBLS algorithm. We collaborated on the mathematical formulation of the NBLS algorithm, and he took the lead on coding the NBLS algorithm, utilized to obtain the simulation results reported in [31].

Section 4.4 reports an extension to the AID algorithm for identifying simultaneously the plant parameters and the actuator parameters for second-order, underactuated, rigid-body UV plants in 6 DOF.

The AID approach for UVs in 6 DOF was developed by Christopher McFarland with the assumption that the control actuator parameters were known [52]. The AID algorithm reported by McFarland was extended by Tyler Paine to include the control-actuator parameters as part of the AID state [58]. An analytical stability proof of this extension to estimate simultaneously the plant-model parameters and control-actuator parameters in 6 DOF was reported in Paine's masters thesis utilizing scalar gains [58]. Paine and Harris contributed equally to the publication of this AID extension to estimate simultaneously the plant and control parameters with an analytic stability proof using scalar gains and a preliminary simulation effort conducted with the forward simulation and AID done in a loop [77]. However, preliminary anecdotal simulation efforts in post-processing the simulated data by the author indicated poor parameter convergence with scalar gains. This thesis extends Paine's stability proof to utilize diagonal gain matrices rather than scalar gains. This thesis also reports simulation results in 6 DOF with realistic sensor noise, as well as a measurement-noise sensitivity analysis.

4.1 Literature Review

Several types of identification methods for UV model parameters have been reported. Identification methods largely fall into one of the following categories: least squares, adaptive estimation, Kalman filter (KF) variants, and machine learning (ML) or neural network (NN) techniques.

Hegrenaes *et al.* report a constrained least-squares method in [34] for 3 DOF parameter identification of an underactuated UV. The method simultaneously identifies the model parameters and the control-surface parameters as defined in [72]. The authors report a cross validation with experimental results.

Experimental parameter identification for underactuated gliders are reported by Graver *et al.* in [29], but only parameters that are observable in steady glide are estimated, eliminating the need for body-acceleration signals. Least-squares parameter identification methods for fully actuated UVs were studied extensively in [50] and [56]. Martin and Whitcomb in [50] report experimental identification and validation of a fully coupled 6 DOF model of a fully actuated UV using both total least squares and ordinary least squares, but this method requires prior knowledge of the thruster dynamics. Ridao *et al.* in [63] compares experimental identification of a fully actuated, decoupled 3 DOF vehicle parameters using least squares and a second method which involves numerical integration to avoid differentiating the body velocities. However, with a sufficiently small time step, the two reported methods appear to be mathematically equivalent and subject to the same noise and numerical inaccuracies [58].

AIDs for fully-actuated multi-DOF UV plant models were first reported by Smallwood and Whitcomb in [71], but this AID was limited to fully diagonal plant models in which the dynamics of each degree of freedom is fully decoupled and independent from the dynamics of other degrees of freedom. McFarland and Whitcomb in [52] report an AID for fully coupled, fully actuated 6 DOF UV plant models which is the foundation for the extension reported in this thesis. Neither AID requires body acceleration signals which may offer an advantage over other parameter estimation methods such as LS approaches, all of which require linear and angular acceleration signals. Both papers provide Lyapunov stability proofs, and experimental results for a fully actuated UV are compared with those from the LS method. In [57], Paine and Whitcomb reported an extension of the AID reported in [71] to 3 DOF underactuated UV plant models, including a simulation study with Gaussian noise.

UV parameter identification using Kalman Filter and its variants are reported in [76] and [66]. [76] reports an extended Kalman filter (EKF) estimation of 1 DOF dynamics of an underactuated, torpedo-shaped body using experimental data. In [66] Sabet *et al.* identify some dynamical model parameters of a 6 DOF torpedo-shaped UVs in simulation using the cubature Kalman filter and the transformed unscented Kalman filter. The authors estimate control-input coefficients for the control surfaces as formulated in [72] but assume the thrust coefficient and mass terms are known.

ML and NN based identification methods have been recently reported for UVs in [38,68,79,87–89]. In [87], Wehbe *et al.* reports a study of several ML methods for identifying the decoupled drag in the sway and yaw DOF of a torpedo shaped UV. They conclude that kernel-based nonlinear estimators yield better estimations for hydrodynamic damping terms of UV than NN or least squares approaches. Wehbe and Krell in [88] report a method that uses support vector regression to model the non-linear dynamical UV plant with only control inputs and observed state outputs. They report experimental results in 3 DOF and compare performance with two least squares approaches. [79] reports a neural network augmented identification of the coupled damping matrix that is robust to noise and correctly adapts to time-varying drag dynamics with online learning. The authors report a simulation, but no experimental data. Wu *et al.* in [89] report a symbolic regression method based on a genetic algorithm for UV parameters. Using simulated 6 DOF data, the authors compare identification using a symbolic regression and Levenberg-Marquardt least squares.

Another genetic algorithm is reported in [68] and simulation results are reported for a 3 DOF UV (pitch, yaw, and roll). Online reinforcement learning is proposed by Karras *et al.* in [38] to identify the parameters of an underactuated UV. The method is derivative-free, and 4 DOF (x, y, z, heading) experimental results are reported. All ML/NN approaches reviewed assume knowledge of thruster and control-input models except for [88], where their ML algorithm learns an unknown nonlinear multivariate that maps body velocity and raw actuator inputs to vehicle body accelerations. Additionally, in most cases, significant computational time and training data are needed to complete estimates using ML and NN methods.

4.2 Iver3 Measurement Sources and Noise Statistics

The goal of this chapter is parameter estimation for underactuated, torpedo-shaped UVs in 6 DOF with realistic sensor noise. As a test platform, we utilized the JHU Iver3 AUV, which is a typical low-cost, torpedo-shaped commerical off-the-shelf (COTS) autonomus underwater vehicle (AUV) with a standard sensor suite. Because the sensors onboard the JHU Iver3 AUV are standard COTS sensors, we believe these sensors represent a standard sensor suite on a COTS torpedo-shaped AUV. Table 4.1 lists the measured signals and sources available on the JHU Iver3 AUV.

Note that we have two separate ways to measure the vehicle's linear acceleration: 1)

Table 4.1: Signals and Sources

DOF	Measured Signal	Source
Attitude	$rph \in \mathbb{R}^3$	Iver compass
Linear Vel	${}^b v_{dvl} \in \mathbb{R}^3$	RDI Explorer DVL
Angular Vel	${}^m \omega_m \in \mathbb{R}^3$	Microstrain 3DM-GX-25
Linear Accel	${}^m a_m \in \mathbb{R}^3$	Microstrain 3DM-GX-25
Linear Accel	${}^b \dot{v}_{dvl} \in \mathbb{R}^3$	DVL (differentiated)
Angular Accel	${}^m \dot{\omega}_m \in \mathbb{R}^3$	Microstrain (differentiated)

differentiate the DVL body velocity signal and 2) transform the Microstrain linear acceleration signal (which includes the gravity vector) from instrument frame to body frame. This acceleration transformation is discussed in Section 4.2.2. In practice, we chose to differentiate and low-pass filter the DVL data to obtain the acceleration signal, for reasons discussed in 4.2.2.

4.2.1 Measurement Noise Statistics

This section reports noise statistics for the instruments mounted in the Iver3 AUV collected with a static test with the Iver3 sitting stationary on the bench.

4.2.1.1 Iver3 Compass

Table 4.2 shows the measured noise statistics for the magnetic compass on board the JHU Iver3 AUV in a static bench-top test. Figure 4.1 shows the measured signals of roll, pitch, and heading of the magnetic compass on board the JHU Iver3 AUV. Figure 4.2 show a histogram of the measured roll, pitch, and heading precision.

The heading accuracy of the Iver3 compass is typically $5°$-$10°$ root mean square error (RMS) before calibrating the compass; after hard-iron and soft-iron calibration, the error is approximately $1°$-$2°$ RMS, but it is difficult to evaluate the calibrated heading accuracy.

Table 4.2: Iver3 Compass Measured Noise Statistics

DOF	Standard Deviation
Roll	$0.0555°$
Pitch	$0.0503°$
Heading	$0.1488°$

4.2.1.2 Teledyne RDI Explorer DVL

We recorded velocity measurements with the Teledyne RDI Explorer 600 kHz phased-array DVL installed on the JHU Iver3 AUV with the vehicle suspended stationary in a still tank. The sensor readings were identically zero mean and zero standard deviation. Correspondence with Teledyne RDI engineering support team confirmed these results are

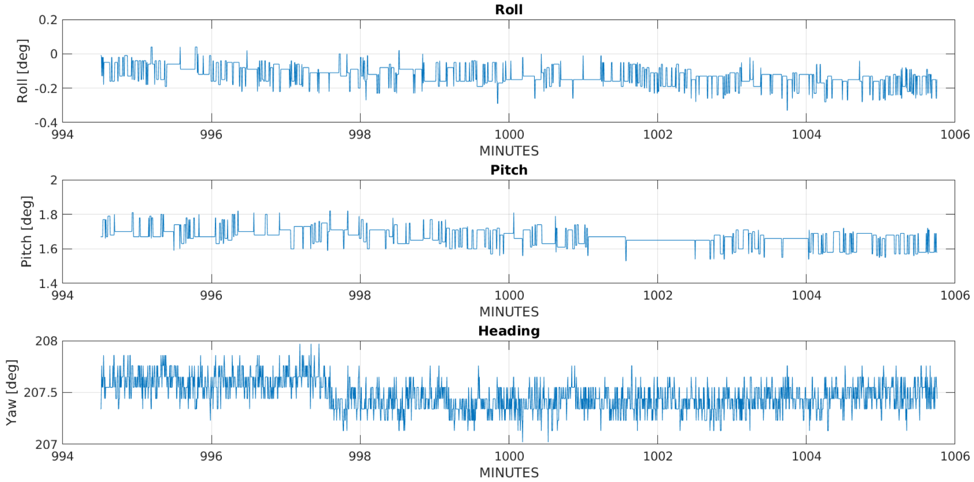

Figure 4.1: Iver3 Compass Static Angular Position. Note that the this is a static benchtop test for precision of a calibrated compass, but we do not attempt to determine the true accuracy or bias of the compass, especially in the heading DOF.

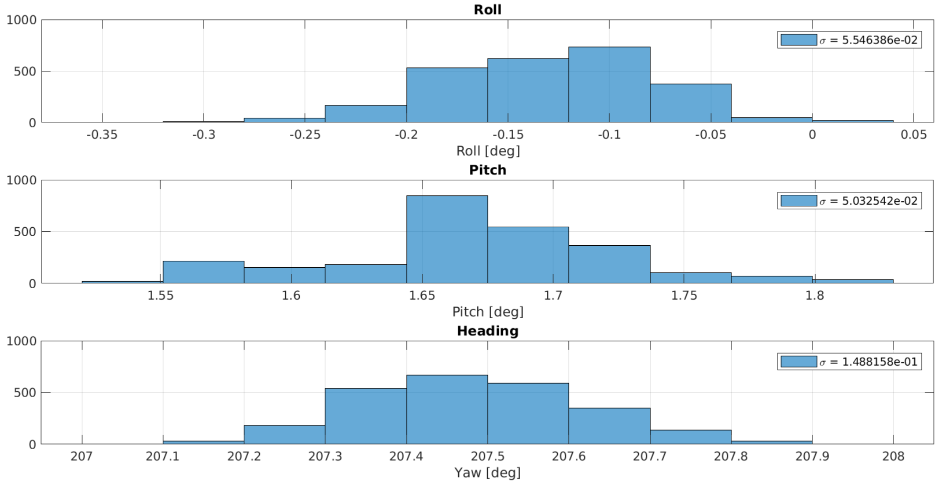

Figure 4.2: Iver3 Compass Static Benchtop Test Attitude Histogram

expected in a completely stationary test. We were referred to the specifications sheet for the sensor measurement-noise statistics as a function of advance velocity.

As per the specifications sheet provided by Teledyne RDI, the Explorer phased-array DVL has the precision in bottom tracking mode as listed in Table 4.3.

Table 4.3: Teledyne RDI Explorer DVL Precision in Single-Ping Bottom Lock, per the Manufacturer Specification Sheet

Advance Velocity	Standard Deviation
1 m/s	1 cm/s
3 m/s	1.8 cm/s
5 m/s	2.6 cm/s

4.2.1.3 Microstrain

We recorded angular velocity and linear acceleration measurements using a Microstrain 3DM-GX-25 attitude and heading reference sensor (AHRS) mounted in the nose cone of the Iver AUV. The sensor is rated to the standard angular-rate range (±300°/s) and translational-acceleration range (±8g). Also note that the noise statistics depend on the sampling rate; we set the sensor sampling rate to 10Hz.

Table 4.4 reports the standard deviation of the Microstrain mounted in the Iver3 during a static benchtop test. Figure 4.3 shows the angular-rate signals recorded by the Microstrain 3DM-GX-25 during the benchtop test. Figure 4.5 shows the translational-acceleration signals recorded by the Microstrain 3DM-GX-25 during the benchtop test.

Figure 4.4 and Figure 4.6 show histograms of the noise statistics for the Microstrain angular velocity and linear acceleration measurements, respectively.

Table 4.4: Microstrain 3DM-GX-25 Measured Noise Statistics

DOF	Mean	Standard Deviation
ω_x	$-0.0664°$	$0.0094°/s$
ω_y	$0.0343°$	$0.0090°/s$
ω_z	$-0.0023°$	$0.0090°/s$
Surge Acceleration	$-0.0936\ m/s$	$0.4445\ mm/s^2$
Sway Acceleration	$-0.1024m/s$	$0.5275\ mm/s^2$
Heave Acceleration	$-9.8059m/s$	$0.4803\ mm/s^2$

4.2.2 Linear Acceleration Coordinate Transformation

The Microstrain AHRS is mounted in the nose cone of the Iver3 AUV, and as shown in Figure 4.5, the Microstrain's measured translational acceleration includes acceleration due to gravity. Thus, to utilize the Microstrain's measurement of translational acceleration, we must transform the acceleration from the Microstrain instrument frame to the Iver3 body frame and remove the acceleration due to gravity.

Table 4.5 defines the frames used in this derivation.

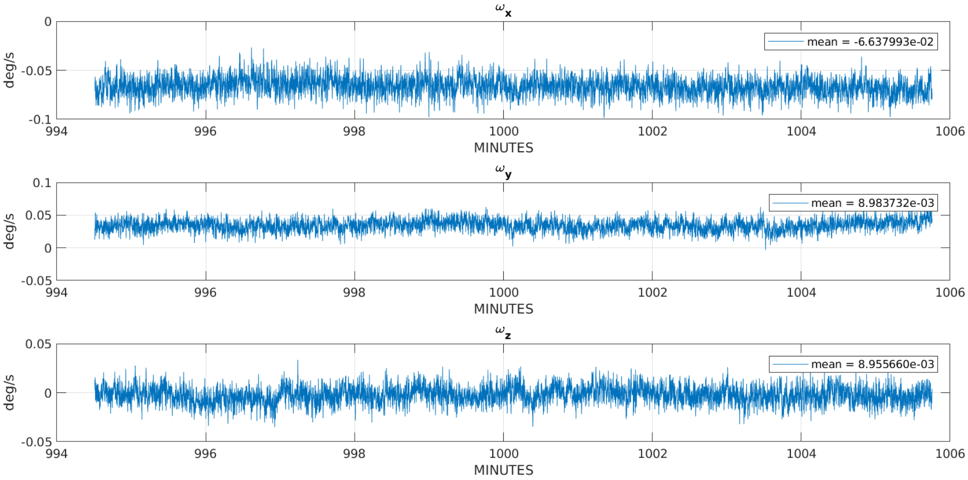

Figure 4.3: Microstrain 3DM-GX-25 AHRS Static Angular Velocity. Note that this figure is during a static test. We expect that the noise statistics will be worse when the instrument is subject to dynamic motion, such as during UV missions.

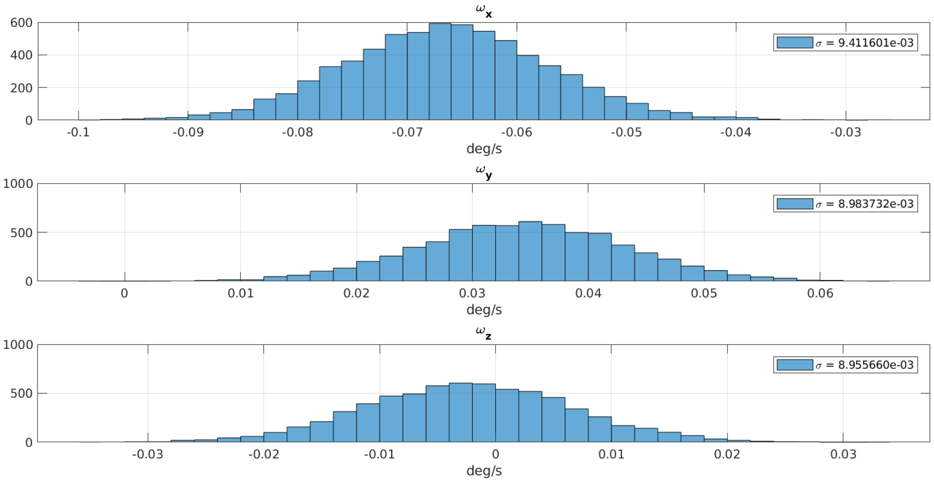

Figure 4.4: Microstrain 3DM-GX-25 AHRS Static Angular Velocity Histogram Note that these noise statistics are in a static benchtop test. We expect that the noise statistics will be worse when the instrument is subject to dynamic motion, such as during UV missions.

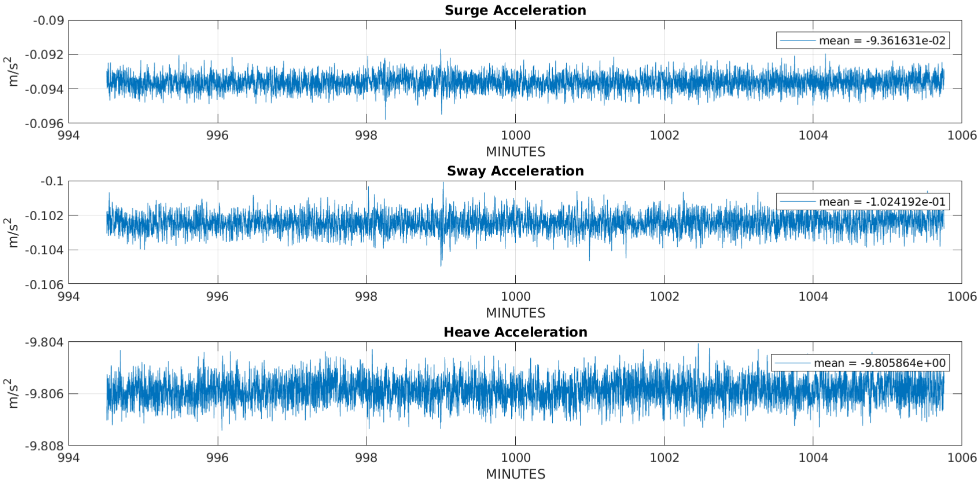

Figure 4.5: Microstrain 3DM-GX-25 AHRS Static Translational Acceleration Measured Data. Note that these noise statistics are in a static benchtop test. We expect that the noise statistics will be worse when the instrument is subject to dynamic motion, such as during UV missions.

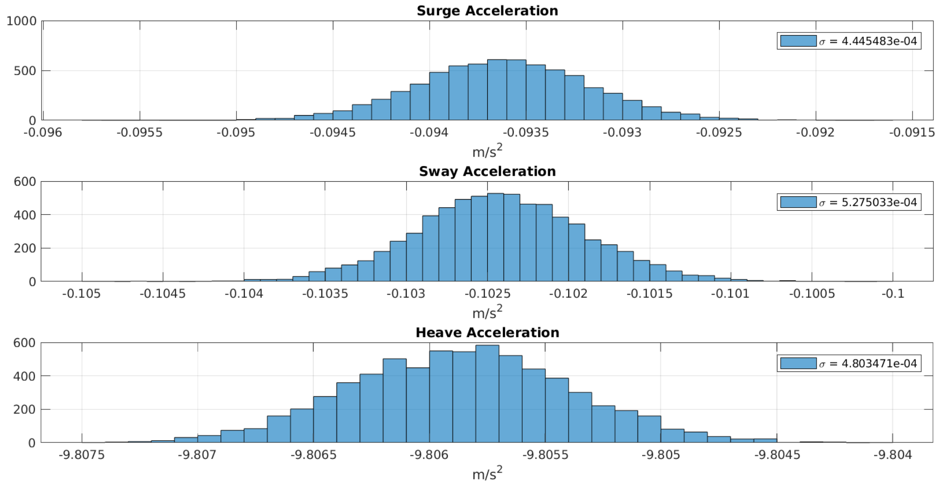

Figure 4.6: Microstrain 3DM-GX-25 AHRS Static Linear Acceleration Histogram. Note that these noise statistics are in a static benchtop test. We expect that the noise statistics will be worse when the instrument is subject to dynamic motion, such as during UV missions.

Table 4.5: Frame Definition

frame	Source
b	body frame
w	world frame
m	microstrain frame
r	vector from cg to microstrain
x	vector from dvl to microstrain

The angular velocity is defined

$$^{b}\omega_b = {}^{b}_{m}R\, {}^{m}\omega_m, \tag{4.2}$$

where ${}^{b}_{m}R = R_x(0)R_y(0)R_z(\pi)$ is the constant rotation matrix from body frame to microstrain frame. We compute the linear body acceleration as the time derivative of the linear body velocity as

$$^{w}v_b = {}^{w}v_m - {}^{w}\omega_b \times {}^{w}r \tag{4.3}$$

$${}^{b}_{w}R(t)\,{}^{w}v_b = {}^{b}_{w}R(t)\left({}^{w}v_m - {}^{w}\omega_b \times {}^{w}r\right) \tag{4.4}$$

$${}^{b}_{w}R(t)\,{}^{w}v_b = {}^{b}_{w}R(t)\,{}^{w}v_m - {}^{b}_{w}R(t)\left({}^{w}\omega_b \times {}^{w}r\right) \tag{4.5}$$

$$\underbrace{{}^{b}_{w}R(t)\,{}^{w}v_b}_{{}^{b}v_b} = {}^{b}_{w}R(t)\,{}^{w}v_m - \left[\underbrace{{}^{b}_{w}R(t)\,{}^{w}\omega_b}_{{}^{b}\omega} \times \underbrace{{}^{b}_{w}R(t)\,{}^{w}r}_{{}^{b}r}\right] \tag{4.6}$$

$${}^{b}v_b = {}^{b}_{w}R(t)\,{}^{w}v_m - \left({}^{b}\omega \times {}^{b}r\right), \tag{4.7}$$

where ${}^{b}_{w}R(t) = R_x\big(\varphi(t)\big)R_y\big(\theta(t)\big)R_z\big(\psi(t)\big)$ is the rotation from world to body frame.

$R_x\big(\varphi(t)\big)$ is the rotation about the body x axis by the roll angle, $\varphi(t)$. $R_y\big(\theta(t)\big)$ is the rotation about the body y axis by the pitch angle, $\theta(t)$. $R_z\big(\psi(t)\big)$ is the rotation about the body z axis by the heading angle, $\psi(t)$. Differentiating with respect to time yields

$$\frac{d}{dt}\left[{}^{b}v_b\right] = \frac{d}{dt}\left[{}^{b}_{w}R(t)^{w}v_m - \left({}^{b}\omega \times {}^{b}r\right)\right] \tag{4.8}$$

$${}^{b}\dot{v}_b = {}^{b}_{w}\dot{R}(t)^{w}v_m + {}^{b}_{w}R(t)^{w}\dot{v}_m - \frac{d}{dt}\left[{}^{b}\hat{\omega}\,{}^{b}r\right] \tag{4.9}$$

$$= {}^{b}\omega \times {}^{b}_{w}R(t)\,{}^{w}v_m + {}^{b}_{w}R(t)\,{}^{w}\dot{v}_m - {}^{b}\dot{\omega} \times {}^{b}r \tag{4.10}$$

$$= {}^{b}\omega \times {}^{b}_{w}R(t)\,{}^{w}v_m + {}^{b}_{w}R(t)^{w}\dot{v}_m - {}^{b}\dot{\omega} \times {}^{b}r \tag{4.11}$$

$$= \left({}^{b}\omega \times {}^{b}v_m\right) + {}^{b}_{w}R(t)^{w}\dot{v}_m - \left({}^{b}\dot{\omega} \times {}^{b}r\right). \tag{4.12}$$

The acceleration is

$${}^{w}a_m = {}^{w}\dot{v}_m + {}^{w}g \tag{4.13}$$

$${}^{m}a_m = {}^{m}_{w}R(t)\left[{}^{w}\dot{v}_m + {}^{w}g_m\right] \tag{4.14}$$

$${}^{w}\dot{v}_m = {}^{w}_{m}R(t)^{m}a_m - {}^{w}g_m, \tag{4.15}$$

where ${}^{m}a_m$ is the linear acceleration measured by the Microstrain and

${}^{w}g_m = \begin{vmatrix} 0 & 0 & 9.81 \end{vmatrix}^{T}$. Thus,

$${}^{b}\dot{v}_b = \left({}^{b}\omega \times {}^{b}v_m\right) + {}^{b}_{w}R(t)\left({}^{w}_{m}R(t)^{m}a_m - {}^{w}g_m\right) - \left({}^{b}\dot{\omega} \times {}^{b}r\right) \tag{4.16}$$

$$= \left({}^{b}\omega \times {}^{b}v_m\right) + {}^{b}_{m}R\,{}^{m}a_m - {}^{b}_{w}R(t)\,{}^{w}g_m - \left({}^{b}\dot{\omega} \times {}^{b}r\right), \tag{4.17}$$

where

$${}^{b}v_m = {}^{b}\omega \times {}^{b}x + {}^{b}v_{dvl}, \tag{4.18}$$

and thus,

$$
\begin{aligned}
{}^{b}\dot{v}_{b} &= {}^{b}\omega \times \Big(\big({}^{b}\omega \times {}^{b}x \big) + {}^{b}v_{dvl} \Big) + {}^{b}_{m}R\, {}^{m}a_{m} - {}^{b}_{w}R(t)\, {}^{w}g_{m} - \big({}^{b}\dot{\omega} \times {}^{b}r \big) \qquad (4.19) \\
&= {}^{b}\omega \times \big({}^{b}\omega \times {}^{b}x \big) + \big({}^{b}\omega \times {}^{b}v_{dvl} \big) + {}^{b}_{m}R\, {}^{m}a_{m} - {}^{b}_{w}R(t)\, {}^{w}g_{m} - \\
&\quad \big({}^{b}\dot{\omega} \times {}^{b}r \big) \\
&= {}^{b}\omega \big({}^{b}\omega^{T}\, {}^{b}x \big) - {}^{b}x \big({}^{b}\omega^{T}\, {}^{b}\omega \big) + \big({}^{b}\omega \times {}^{b}v_{dvl} \big) + {}^{b}_{m}R\, {}^{m}a_{m} - {}^{b}_{w}R(t)\, {}^{w}g_{m} - \\
&\quad \big({}^{b}\dot{\omega} \times {}^{b}r \big) \\
&= {}^{b}\omega \big({}^{b}\omega^{T}\, {}^{b}x \big) - {}^{b}x\, {}^{b}\omega^{2} + \big({}^{b}\omega \times {}^{b}v_{dvl} \big) + {}^{b}_{m}R\, {}^{m}a_{m} - {}^{b}_{w}R(t)\, {}^{w}g_{m} - \\
&\quad \big({}^{b}\dot{\omega} \times {}^{b}r \big) \qquad (4.20)
\end{aligned}
$$

The measured total acceleration from the Microstrain sensor is the sum of gravity (1g) and the vehicle acceleration relative to a north-east-down (NED) local reference frame. The signal of vehicle acceleration is roughly an order of magnitude smaller than the gravity vector—meaning the total measured acceleration signal reported by the Microstrain is dominated by the acceleration due to gravity. As shown in (4.20), removing the gravity signal from the measured vehicle's acceleration signal requires accurate attitude measurements. Thus, it is effectively impossible to isolate the UV motion from the gravitation acceleration with the compass on board the Iver3 AUV. For this reason, we chose to differentiate and then low-pass filter the DVL-reported velocity wherever the signal of vehicle linear acceleration was required.

4.3 Nullspace-Based Least Squares

This section reports a novel approach to solving the parameter-estimation problem for UV plants of the form (4.1) based on least-squares regression analysis. To the best of our knowledge, the **nullspace-based least squares (NBLS)** algorithm, first reported in [31], is the first reported method to identify simultaneously the plant-model parameters and the control-actuator parameters. This section was coauthored with Tyler Paine, who assisted in the mathematical development of the NBLS algorithm and took the lead on coding the first implementation of the NBLS algorithm.

4.3.1 Iver3 UV Plant and Actuator Model

We utilize a nonlinear dynamic process model for the vehicle (4.1), with terms defined as in (3.1), with the exception of the drag matrix. For the NBLS algorithm, we chose to include four additional off-diagonal quadratic drag terms in the diagonal quadratic drag matrix:

$$\boldsymbol{D}(\boldsymbol{\nu}) = \begin{bmatrix} d_{11}|u| & 0 & 0 & 0 & 0 & 0 \\ 0 & d_{22}|v| & 0 & 0 & 0 & d_{26}|c| \\ 0 & 0 & d_{33}|w| & 0 & d_{35}|b| & 0 \\ 0 & 0 & 0 & d_{44}|a| & 0 & 0 \\ 0 & 0 & d_{53}|w| & 0 & d_{55}|b| & 0 \\ 0 & d_{62}|v| & 0 & 0 & 0 & d_{66}|c| \end{bmatrix} \tag{4.21}$$

Exploiting port-starboard symmetry, we set $d_{35} = d_{53}$ and $d_{26} = d_{62}$. The off-diagonal entries correspond to a moment on the UV, which occurs because the vehicle's CP is not coincident with the CG. We chose to include off-diagonal drag terms to avoid potential issues with un-modeled dynamics when identifying parameters in experimental data for the Iver3 AUV. In anecdotal simulation results, the NBLS approach performs equally as well with the off-diagonal drag terms set to zero.

4.3.1.1 Parameter Vector

As is typical for the least-squares approach to parameter estimation, we define a vector of model parameters that enter *linearly* into (4.1). The parameter vector, $\boldsymbol{\theta_p}$, is defined as

$$\boldsymbol{\theta_p} = \left| \boldsymbol{m_p}^T \ \boldsymbol{d_p}^T \ m_7 \ m_8 \ \beta_1 \ \beta_2 \ \beta_3 \ \beta_4 \ \beta_5 \right|^T \in \mathbb{R}^{21} \tag{4.22}$$

where the mass and quadratic drag parameters are

$$\boldsymbol{m_p} = \begin{vmatrix} m_{11} & m_{22} & m_{33} & m_{44} & m_{55} & m_{66} \end{vmatrix}^T \in \mathbb{R}^6 \tag{4.23}$$

$$\boldsymbol{d_p} = \begin{vmatrix} d_{11} & d_{22} & d_{33} & d_{44} & d_{55} & d_{66} & d_{26} & d_{35} \end{vmatrix}^T \in \mathbb{R}^8. \tag{4.24}$$

Note that the parameters m_7 and m_8 have physical significance: $gm_7 = g(m - \rho\bigtriangledown)$ is the net buoyant force in Newtons, and $gm_8 = g(z_b\rho\bigtriangledown)$ is the net restoring moment in Newton-meters. Here z_b is the vertical distance, in meters, between the vehicle's CG, the reference frame for all our derivations, and the center of buoyancy (CB).

Lift and drag coefficients of symmetric airfoils, like the control fins on the JHU Iver3 AUV, are well established in aerodynamics literature [2]. In general, $C_L(\alpha)$ is experimentally found to be an odd function and $C_D(\alpha)$ an even function with a positive intercept. Thus, we use a simple parameterization of $C_L(\alpha)$ and $C_D(\alpha)$

$$C_L(\alpha) = \beta_3\alpha + \beta_4\alpha^3 \tag{4.25}$$

$$C_D(\alpha) = \beta_1 + \beta_2\alpha^2. \tag{4.26}$$

Lastly, the propeller coefficient β_5 is defined such that

$$T = \beta_5\omega_p^2. \tag{4.27}$$

4.3.1.2 NBLS Algorithm

Because all of the parameters in $\boldsymbol{\theta_p}$ enter into (4.1) linearly, we can write

$$0 = \frac{\partial}{\partial \boldsymbol{\theta_p}} \bigg(\boldsymbol{M}\dot{\boldsymbol{\nu}} + \left(\boldsymbol{D}(\boldsymbol{\nu}) + \boldsymbol{C}(\boldsymbol{\nu})\right)\boldsymbol{\nu} + \boldsymbol{g}(\boldsymbol{\varphi}) - \boldsymbol{\tau}(\boldsymbol{\nu}, \boldsymbol{\xi}) \bigg) \boldsymbol{\theta_p} \tag{4.28}$$

$$0 = \mathbb{W}(\dot{\boldsymbol{\nu}}, \boldsymbol{\nu}, \boldsymbol{\varphi}, \boldsymbol{\xi})\boldsymbol{\theta_p}, \tag{4.29}$$

where

$$\mathbb{W}(\dot{\boldsymbol{\nu}}, \boldsymbol{\nu}, \boldsymbol{\varphi}, \boldsymbol{\xi}) \in \mathbb{R}^{6\times 21} \tag{4.30}$$

is a matrix-valued function commonly termed the *regressor matrix*. During an experiment (or simulated experiment), we observe the vehicle's body velocity $\boldsymbol{\nu(t_i)}$, body acceleration $\dot{\boldsymbol{\nu}}\boldsymbol{(t_i)}$, body attitude $\boldsymbol{\varphi(t_i)}$, and control inputs $\boldsymbol{\xi(t_i)}$ at time $t_i \in [t_1, t_n]$. Let $\mathbb{W}_{t_i}$ be the regressor matrix computed using experimental data observed at time t_i. Each $\mathbb{W}_{t_i}$ matrix is appended to the end of a composite matrix, $\overline{\mathbb{W}}$,

$$\overline{\mathbb{W}} = \left| \begin{matrix} \mathbb{W}_{t_0} \\ \mathbb{W}_{t_1} \\ \vdots \\ \mathbb{W}_{t_i} \end{matrix} \right| \in \mathbb{R}^{6n\times 21}\ \forall t_i \in [t_1, t_n]. \tag{4.31}$$

We can solve for $\boldsymbol{\theta_p}$ using the following properties of linear algebra:

Proposition: $\boldsymbol{\theta_p} \in \ker(\overline{\mathbb{W}}^T\overline{\mathbb{W}})$

Proof: By definition of the kernel, (4.29) means $\boldsymbol{\theta_p} \in \ker\left(\mathbb{W}_{t_i}\right)$. Note that

$$\overline{\mathbb{W}}^T\overline{\mathbb{W}} = \sum_{i=0}^{n} \mathbb{W}_{t_i}^T \mathbb{W}_{t_i}, \tag{4.32}$$

meaning

$$\overline{\mathbb{W}}^T\overline{\mathbb{W}}\boldsymbol{\theta_p} = \Big[\sum_{i=0}^{n} \mathbb{W}_{t_i}^T \mathbb{W}_{t_i}\Big]\boldsymbol{\theta_p} \tag{4.33}$$

$$= \sum_{i=0}^{n} \big[\mathbb{W}_{t_i}^T \mathbb{W}_{t_i}\boldsymbol{\theta_p}\big] \tag{4.34}$$

$$= \mathbf{0}. \tag{4.35}$$

Thus $\boldsymbol{\theta_p} \in \ker(\overline{\mathbb{W}}^T\overline{\mathbb{W}})$. Also $\boldsymbol{\theta_p} \neq \mathbf{0}$ because the vehicle parameters are not all zero, meaning $\overline{\mathbb{W}}^T\overline{\mathbb{W}}$ is rank deficient. This analytical result holds for perfectly modeled, finite-dimensional systems without noise and forms a theoretical basis for applications on real UV parameter identification. In practice, sensor noise, unmodeled system dynamics, and numerical precision will add more variability to the data, which will artificially reduce the dimension of $\ker(\overline{\mathbb{W}}^T\overline{\mathbb{W}})$ to be numerically zero and thus $\overline{\mathbb{W}}^T\overline{\mathbb{W}}$ will have full rank. Consequently, we use the following solution to the classic least squares problem:

$$\min_{\boldsymbol{\theta_p}} \Big\{ ||\overline{\mathbb{W}}\boldsymbol{\theta_p}||_2 \colon \; ||\boldsymbol{\theta_p}||_2 = 1 \Big\}, \tag{4.36}$$

where $|| * ||_2$ is the ℓ_2-norm. Note that this minimization problem may be rewritten as

$$\min_{\boldsymbol{\theta_p} \neq 0} \left\{ \frac{\boldsymbol{\theta_p}^T \overline{\mathbb{W}}^T \overline{\mathbb{W}} \boldsymbol{\theta_p}}{\boldsymbol{\theta}_p^T \boldsymbol{\theta}_p} \right\}. \tag{4.37}$$

$\overline{\mathbb{W}}^T\overline{\mathbb{W}}$ is Hermitian, so, by the Rayleigh-Ritz inequality [35], (4.37) is bounded from below by the smallest eigenvalue of $\overline{\mathbb{W}}^T\overline{\mathbb{W}}$, with equality achieved when $\boldsymbol{\theta_p}$ is the eigenvector corresponding to the minimum eigenvalue of $\overline{\mathbb{W}}^T\overline{\mathbb{W}}$. If more than one eigenvalue of $\overline{\mathbb{W}}^T\overline{\mathbb{W}}$ is zero, then the solution is any vector in the kernel of $\overline{\mathbb{W}}^T\overline{\mathbb{W}}$.

Note that solutions for $\boldsymbol{\theta_p}$ of this form are only defined up to scale. In practice, we chose scale the vector by a known parameter, such as the net buoyant force of the vehicle.

4.3.2 NBLS Results

This section reports simulation results with the NBLS algorithm. First, we report anecdotal simulation results with additive Gaussian noise to ensure there is sufficient motion for the parameter vector defined above to be observable. We also examine the feasibility of utilizing the NBLS-identified parameters in cooperative acoustic navigation without a DVL. These results were first reported in [31]. Anecdotally, we observe the NBLS algorithm is relatively sensitive to measurement noise, especially in translational velocity and translational acceleration. Section 4.3.2.3 reports a noise sensitivity analysis conducted by varying translational velocity noise, and, as mentioned above, differentiating the translational velocity and then low-pass filtering the differentiated signal to obtain translational acceleration. The noise sensitivity analysis indicates it may be infeasible to identify parameters with free-motion experimental trials collected by instruments on board in the Iver3 AUV using the NBLS algorithm, which confirms numerous failed attempts by the authors to use NBLS for parameter identification with real data.

4.3.2.1 Initial NBLS UV Parameter Identification Results

We performed a simulation study to evaluate the feasibility of using the NBLS algorithm described in Section 4.3.1 for parameter estimation of an underactuated, torpedo-shaped AUV in 6 DOF, similar to JHU's OceanServer Iver3 AUV (L3 OceanServer, Fall River, MA, USA). Two simulations of vehicle motion were conducted: the first simulation was used to identify parameters (hereafter referred to as the IDSIM) and the second was used to verify the results using cross-validation (hereafter referred to as the CROSSIM).

In the IDSIM, the simulated vehicle was subject to closed-loop control of forward thrust, pitch, and heading. Trajectory-tracking proportional derivative control (PDC) was used for each of forward thrust, pitch, and heading to track reference trajectories reported in Table 4.6. The total simulated mission time was approximately 30 minutes.

Gaussian noise was added to the true state variables from the forward simulation to emulate sensor noise. Table 4.7 reports the the standard deviation, σ, of the zero-mean Gaussian noise added to each signal. Each signal was then low-pass filtered, acausally to ensure zero phase change. A parameter vector was computed with NBLS, as described in Section 4.3.1.2.

To evaluate the performance of the model with the identified parameters from the IDSIM, we employed the same cross-validation approach as in [52]. In the CROSSIM the identified model was subject to a trackline-following controller with waypoints arranged in a "lawnmower" pattern. This was done intentionally to evaluate the performance of the identified model in a simulation with different trajectories and control types. State estimates of the identified model during the CROSSIM were computed using the CEKF formulation of cooperative acoustic navigation utilizing the dynamic model identified using NBLS. The MAE of the CROSSIM is reported in Table 4.8.

Table 4.6: Sinusoidal Reference Trajectories for IDSIM

DOF	Amplitude	Angular Frequency	Offset
$Surge$	0.2 m/s	0.40 (rad/s)	1 m/s
$Pitch$	-30°	0.30 (rad/s)	
$Heading$	30°	0.35 (rad/s)	

Table 4.7: Standard Deviation σ of Added Noise

Signal	σ	Signal	σ	Signal	σ
$x(t)$		$u(t)$		$\dot{u}(t)$	
$y(t)$	$0\ \mathrm{m}$	$v(t)$	$0.05\ \frac{\mathrm{m}}{\mathrm{s}}$	$\dot{v}(t)$	$0.001\ \frac{\mathrm{m}}{s^2}$
$z(t)$		$w(t)$		$\dot{w}(t)$	
$\phi(t)$		$p(t)$		$\dot{p}(t)$	
$\theta(t)$	$0.1\ \mathrm{deg}$	$q(t)$	$0.36\ \frac{\mathrm{deg}}{\mathrm{s}}$	$\dot{q}(t)$	$0.05\ \frac{\mathrm{deg}}{s^2}$
$\psi(t)$		$r(t)$		$\dot{r}(t)$	

Table 4.8: Mean Absolute Error Values for Cross-Validation

DOF	MAE	DOF	MAE
u	0.0074 m/s	p	1.3e-6 °/s
v	1.6e-5 m/s	q	1.8e-4 °/s
w	4.5e-4 m/s	r	1.2e-5 °/s

4.3.2.2 Effect on Cooperative Navigation

To evaluate the feasibility of using the NBLS-identified parameters in the dynamic UV process model for cooperative acoustic navigation without a DVL, we conducted a preliminary simulation study wherein we used the CEKF version of cooperative acoustic navigation for lawnmower survey at constant altitude with OWTT acoustic updates every 30s. The measurement noise statistics used in the study are listed in Table 4.9. A sample trackline result is shown in Fig 4.7.

We examined CEKF performance with various parameter vectors, including a parameter vector artificially degraded by adding a randomly signed 10% error of the true value to each parameter. The results are plotted in Figure 4.8. The estimated parameter vector performs on par with the true parameter vector, both of which are considerably better than the parameter vector that is accurate to within 10% of the true parameter vector.

Table 4.9: Simulation measurement sources, resolutions, and accuracies

State	Source	Update Rate	Measurement Std Dev
XY Trans	modem	30 s	1 m (range) 0.1m/s (range rate)
Z Trans	Paroscientific	7 Hz	6 cm
Heading	OCTANS	3 Hz	0.10°
Pitch, Roll	OCTANS	3 Hz	0.05°
Trans Velocity	300 kHz RDI DVL	5 Hz (when used)	0.01 m/s (when used)
Ang Vel	OCTANS	3 Hz	0.4-0.6°/s

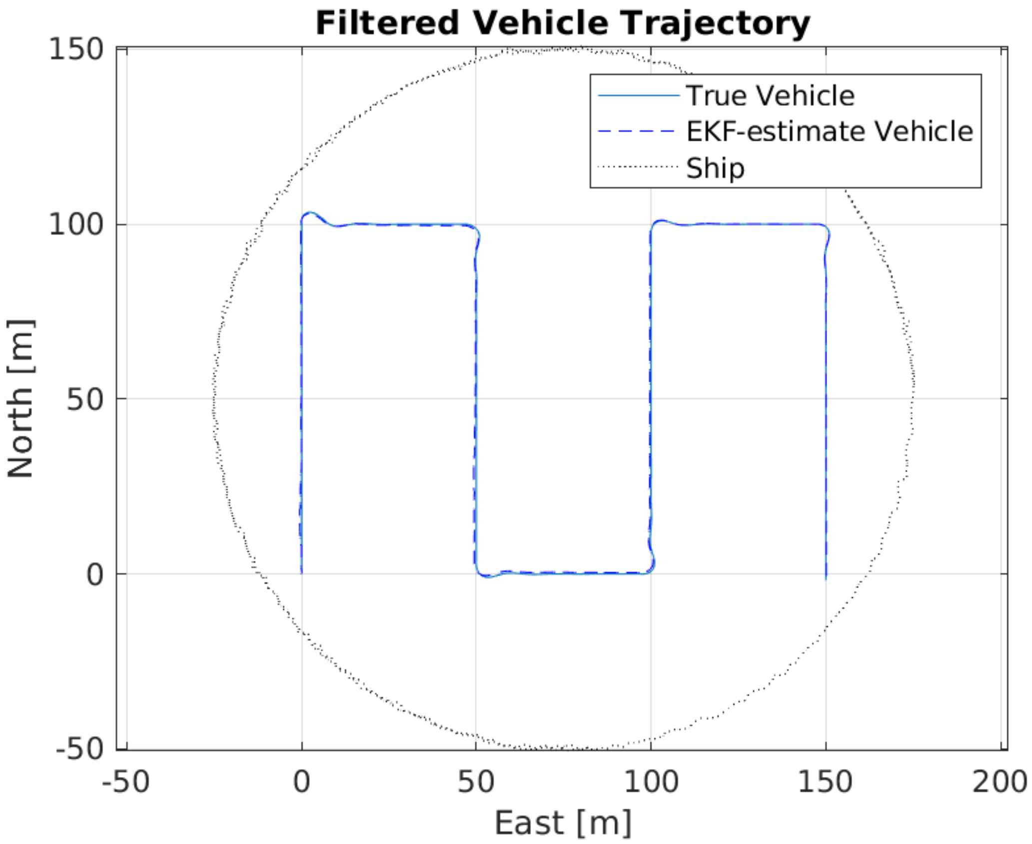

Figure 4.7: Vehicle XY position from the CEKF on simulated data using dynamic model with the NBLS-estimated parameter vector and no DVL. This figure indicates it may be feasible to utilize a parameter vector where both the plant-model parameters and the control-actuator parameters were identified simultaneously using the NBLS algorithm in cooperative acoustic navigation.

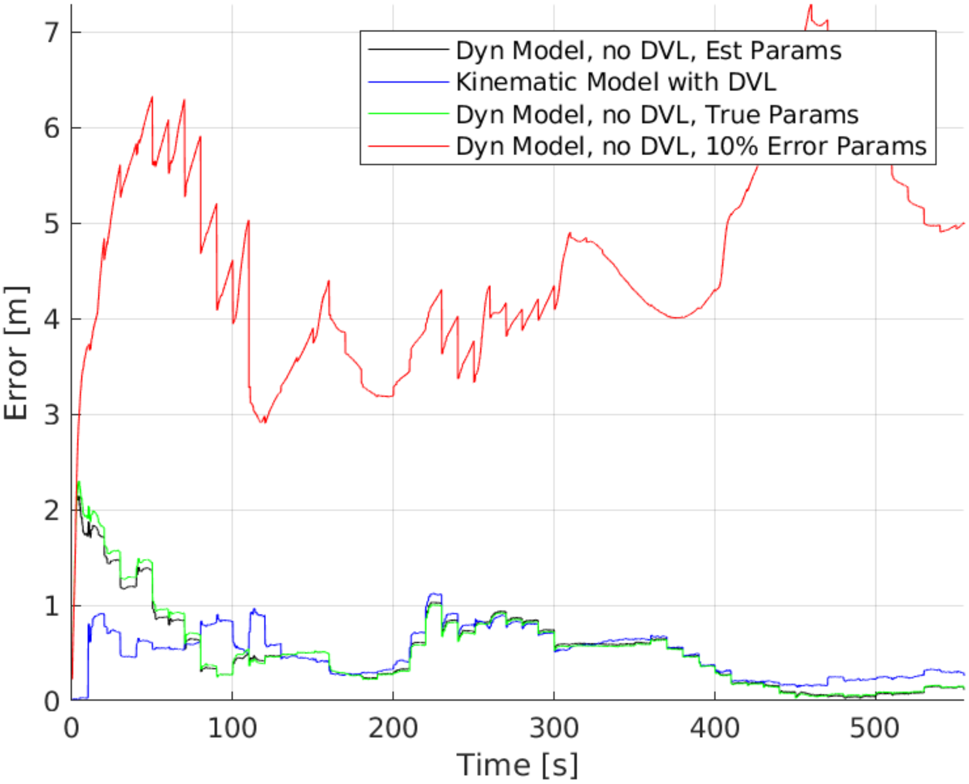

Figure 4.8: Vehicle XY position error magnitude (i.e., the magnitude of the difference between the estimated and true simulated values) from the CEKF on simulated data using dynamic model with the NBLS-estimated parameter vector and no DVL as a function of mission time. This figure indicates that the CEKF utilizing an NBLS-identified parameter vector performs slightly worse than the true parameter vector for the noise statistics reported in 4.9 and significantly better than a parameter vector with a random error with 1σ of 10% of the true values.

4.3.2.3 NBLS Noise Sensitivity Analysis

The results from a preliminary 1 DOF pilot study suggest the NBLS approach performs similarly to total least squares (TLS) and superior to ordinary least squares (OLS) under similar general noise characteristics. Given the success of TLS for model identification of fully actuated remotely operated vehicles (ROVs) with known actuator parameters, as reported in [50] we were hopeful NBLS would achieve adequate results for underactuated unmanned underwater vehicles (UUVs) with unknown actuator parameters.

However, as discussed in Section 4.3.2.3, the NBLS approach to parameter estimation is sensitive and not robust to noise in linear velocity and linear acceleration. Despite substantial effort, we were unable to achieve a adequate parameter estimates utilizing data from the sensors onboard the Iver3 AUV. This section reports a measurement-noise sensitivity analysis, for the purpose of determining whether the NBLS algorithm could work on real data collected with sensors on board the Iver3 AUV. To achieve the results report in Sections 4.3.2.1 and 4.3.2.2, we used static Microstrain levels of noise for acceleration, as noted in Table 4.9. This section attempts to quantify exactly how much sensor noise would be acceptable for parameter estimation with the NBLS algorithm. We generated the true simulated values in forward simulation and added noise. However, as noted in Section 4.2, using the Microstrain measurement of translation acceleration requires accurate knowledge of pitch and roll. Because the gravity vector is such a dominant signal in Microstrain acceleration, simple calculations indicate, the vehicle's pitch and roll would have to be measured more accurately than is available on the Iver3 AUV, either from the OceanServer compass or the Microstrain's internal attitude calculation. Therefore, this noise-sensitivity analysis was conducted with differentiating the DVL velocities and then filtering the differentiated signal with an acausal, second-order low-pass filter. Anecdotal analysis suggests that the NBLS is relatively insensitive to noise in angular position and angular velocity, but quite sensitive to noise in translational velocity.

Table 4.10 reports the MAE and RMS between a simulation using the NBLS-estimated parameter vector and the true simulated values with zero noise in linear velocity and an angular-rate noise with a standard deviation of $0.01°$/s. Table 4.11 and Figure 4.9 report the MAE between a simulation using the NBLS-estimated parameter vector and the true simulated values with varying noise in linear velocity and an angular-rate standard deviation of $0.01°$/s. Table 4.12 and Figure 4.10 report the RMS between a simulation using the NBLS-estimated parameter vector and the true simulated values with varying noise in linear velocity and an angular-rate standard deviation of $0.01°$/s.

As shown in Tables 4.11 and 4.12, the performance of the NBLS algorithm drops off drastically as a function of noise in translational velocity. These tables are plotted in Figures 4.10 and 4.9 to show graphically how the error increases nonlinearly as a function of translational velocity noise.

From this noise-sensitivity analysis, we conclude the NBLS algorithm appears to exhibit a fairly nonlinear response to noise in translational velocity—the algorithm appears fairly immune to noise until approximately 0.5 cm/s, after which the performance quickly degrades until a forward cross-validation simulation with a linear velocity noise of 0.7 cm/s standard deviation would not complete. For comparison, recall from Section 4.2.1 that the Teledyne RDI Explorer DVL installed on the Iver3 AUV has an accuracy of approximately 1.2 cm/s. These simulation results confirm our conjectures from unsuccessful attempts to perform parameter estimation with real data from Iver3 AUV.

Table 4.10: Root Mean Square Error with angular-rate std dev 0.01°/s

	Ang Vel, °/s					Lin Vel, m/s		
	Roll	Pitch	x-DOF	y-DOF	z-DOF	x-DOF	y-DOF	z-DOF
RMS	0.2357	1.5884	0.7634	0.7604	1.4464	0.0059	0.0117	0.0078
MAE	0.1999	1.3712	0.6413	0.6700	1.1838	0.0049	0.0091	0.0069

4.4 Adaptive Identification Algorithm

This section presents an extension of the AID reported in [52] that simultaneously adaptively identifies both plant and control parameters of 6 DOF UVs with diagonal mass and drag matrices. Simulation results with realistic sensor noise are reported, including a noise-sensitivity analysis.

The AID approach for UVs in 6 DOF was developed by Christopher McFarland with the assumption that the control actuator parameters were known [52]. The AID algorithm reported by McFarland was extended by Tyler Paine to include the control-actuator parameters as part of the AID state [58]. An analytical stability proof of this extension to

Table 4.11: Mean Absolute Error with angular-rate noise 0.01°/s

Lin Accel Noise			Ang Vel, °/s			Lin Vel, m/s		
	Roll	Pitch	x-DOF	y-DOF	z-DOF	x-DOF	y-DOF	z-DOF
0 cm/s	0.194	1.4579	0.6587	0.7021	1.2128	0.0051	0.0093	0.0071
0.01 cm/s	0.1929	1.4702	0.6600	0.7062	1.2138	0.0051	0.0093	0.0071
0.1 cm/s	0.1973	1.5127	0.6759	0.7237	1.2424	0.0051	0.0095	0.0073
0.2 cm/s	0.2121	1.6935	0.7369	0.7987	1.3553	0.0054	0.0102	0.0078
0.4 cm/s	0.2798	2.6048	1.0286	1.1673	1.841	0.0073	0.0136	0.0105
0.6 cm/s	0.451	6.1012	2.0443	2.4787	3.5204	0.0200	0.0268	0.0211
0.65 cm/s	0.5072	7.8199	2.672	3.0815	4.5428	0.0245	0.0389	0.0267

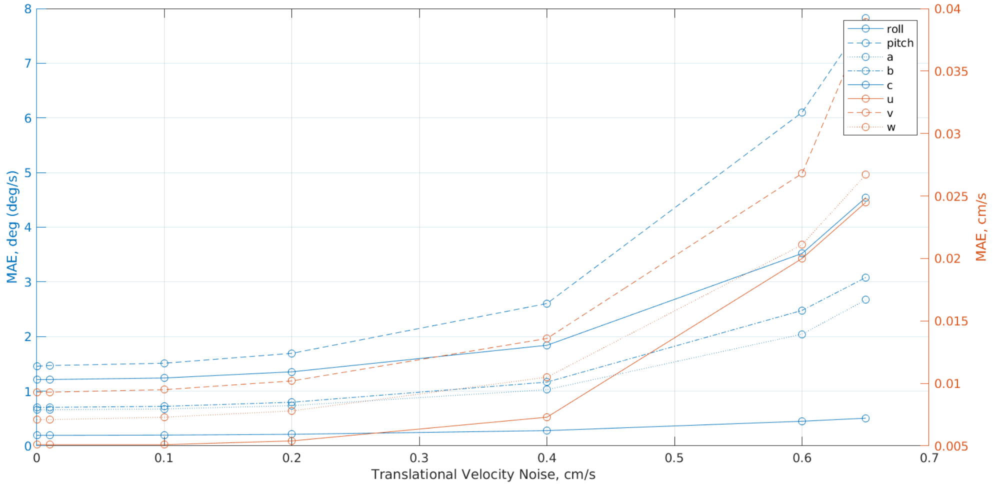

Figure 4.9: NBLS Noise Sensitivity Plot at 0.01 deg/s angular velocity noise: mean absolute error (MAE) vs 1 σ Translational Velocity Noise. In this noise-sensitivity study, the translational velocity was differentiated and then low-pass filtered to obtain the translational acceleration, and the angular velocity was differentiated and low-pass filtered to obtain the angular acceleration. Above 0.65 cm/s 1σ noise, a forward simulation ceases to complete. This figure indicates the NBLS algorithm is sensitive to noise in translational velocity. Further, the NBLS approach is not robust enough to translational velocity noise to work with the best commercially available DVL installed on the Iver3 AUV, which reports translational velocity with a standard deviation of 1.2 cm/s.

Table 4.12: Root Mean Square Error with angular-rate noise 0.01°/s

Lin Accel Noise			Ang Vel, °/s			Lin Vel, m/s		
	Roll	Pitch	x-DOF	y-DOF	z-DOF	x-DOF	y-DOF	z-DOF
0.0 cm/s	0.2291	1.6806	0.7836	0.7943	1.483	0.0061	0.0120	0.0081
0.01 cm/s	0.2278	1.6934	0.7848	0.7984	1.4844	0.0061	0.0120	0.0081
0.1 cm/s	0.2331	1.7393	0.8029	0.8170	1.5215	0.0061	0.0123	0.0083
0.2 cm/s	0.2502	1.9392	0.8716	0.8980	1.6570	0.0065	0.0132	0.0089
0.4 cm/s	0.3308	2.9462	1.2037	1.2997	2.2472	0.0088	0.0177	0.0122
0.6 cm/s	0.552	6.7923	2.3627	2.7517	4.5598	0.0249	0.0368	0.0249
0.65 cm/s	0.6501	8.6905	3.0596	3.4276	6.5601	0.0298	0.056	0.0316

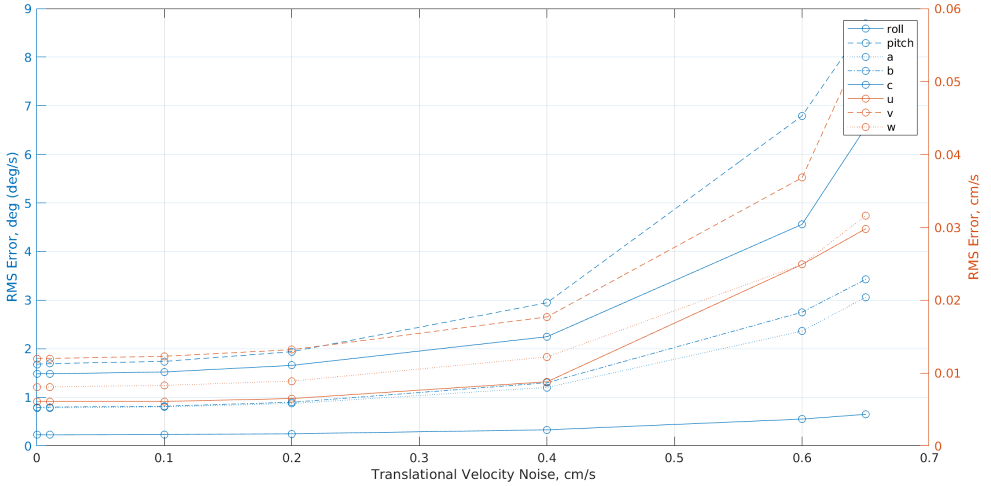

Figure 4.10: NBLS Noise Sensitivity Plot at 0.01 deg/s angular velocity noise: RMSE vs Linear Velocity Noise In this noise-sensitivity study, the translational velocity was differentiated and then low-pass filtered to obtain the translational acceleration, and the angular velocity was differentiated and low-pass filtered to obtain the angular acceleration. Above 0.65 cm/s 1σ noise, a forward simulation ceases to complete. This figure indicates the NBLS algorithm is sensitive to noise in translational velocity. Further, the NBLS approach is not robust enough to translational velocity noise to work with the best commercially available DVL installed on the Iver3 AUV, which reports translational velocity with a standard deviation of 1.2 cm/s.

estimate simultaneously the plant-model parameters and control-actuator parameters in 6 DOF was reported in Paine's masters thesis utilizing scalar gains [58]. Paine and Harris contributed equally to the publication of this AID extension to estimate simultaneously the plant and control parameters with an analytic stability proof using scalar gains and a preliminary simulation effort conducted with the forward simulation and AID done in a loop [77]. However, preliminary anecdotal simulation efforts in post-processing the simulated data by the author indicated poor parameter convergence with scalar gains. This thesis extends Paine's stability proof to utilize diagonal gain matrices rather than scalar gains. This thesis also reports simulation results in 6 DOF with realistic sensor noise, as well as a measurement-noise sensitivity analysis.

Anecdotal numerical simulations with realistic measurement noise indicated poor parameter adaptation with scalar gains. Improved performance was achieved by utilizing diagonal gain matrices, for which we report a novel analytical stability result.

Control of UVs is traditionally achieved using some combination of thrusters and actuated control surfaces. The control actuators or actuation available for many UVs is often modeled as a function of one or more unknown parameters, such as propeller coefficients and lift and drag coefficients of control surfaces, which we will refer to as actuation parameters, and known signals such as angular velocity of propellers, position of control surfaces, and velocity of vehicle relative to the water. Although the structures of many of these control functions are well studied and experimentally verified in the literature [72], the actuation parameters must be determined experimentally for each UV.

4.4.0.1 Parameter Description

We choose to use the dynamics and parameters described in Section 3.1.2. The vector of control inputs $\tau(v, \varphi, \xi) \in \mathbb{R}^6$ is defined as the vector of body-forces that are a result of body velocity v, attitude of the vehicle φ, and p control inputs such as fin angle and propeller speed denoted as $\xi \in \mathbb{R}^p$. If the actuation parameters enter linearly into $\tau(v, \varphi, \xi)$, which they do for the form of $\tau(v, \varphi, \xi) \in \mathbb{R}^6$ developed explicitly in Section 3.1.2.1 as shown in Section 4.3.1.1, then we may the control vector such that

$$\tau(v, \varphi, \xi) = G_a(v, \varphi, \xi)\theta_a, \tag{4.38}$$

where $G_a(v, \varphi, \xi) \in \mathbb{R}^{6xn}$ is the (nonlinear) actuator regressor matrix and $\theta_a \in \mathbb{R}^n$ is the parameter vector that contains the actuator parameters to be identified. As per Section 4.3.1.1, we model fin drag as a quadratic and fin lift as a cubic, each with two unknown parameter coefficients. Examples of these terms include lift and drag coefficients of the control surfaces and propeller coefficients. Substituting (4.38) into (4.1) results in

$$0 = M\dot{v} + C(v)v + D(v)v + \mathcal{G}(\varphi) - G_a(v, \varphi, \xi)\theta_a. \tag{4.39}$$

The following AID can estimate parameters of any vehicle actuation configuration, as long as two conditions are satisfied:

1. The parameters to be identified which make up θ_a must enter linearly into $\tau(v, \varphi, \xi)$
2. The function $G_a(v, \varphi, \xi) \in \mathcal{C}^1$ and is bounded for bounded v, φ, and ξ.

This AID extension comes with an additional caveat. because all terms on both sides of (4.39) contain parameters to be estimated and these parameters enter linearly, the estimate of the set of parameters is only defined up to scale. This is analogous to the limitations of the NBLS parameter-identification method reported in Section 4.3.

Specifically, we attempt to identify the following parameters: m_{11}, m_{22}, m_{33}, m_{44}, m_{55}, m_{66}, d_{11}, d_{22}, d_{33}, d_{44}, d_{55}, d_{66}, g, b_1, b_2, b_3, θ_1, θ_2, θ_3, θ_4, θ_5

Because the mass and drag matrices are diagonal, we use the following notation for convenience: $M =$ diag ($m_{11}, m_{22}, m_{33}, m_{44}, m_{55}, m_{66})$ and $D =$ diag ($d_{11}, d_{22}, d_{33}, d_{44}, d_{55}, d_{66})$

4.4.1 Adaptive Identifier Extension

This section reports an extension to the AID first reported in [58] which itself was an extension of [52] to estimate plant-model and actuator parameters simultaneously with scalar gains. The original contribution of this section is the use of diagonal gain matrices in the stability proof, which preliminary anecdotal simulation studies suggest are required to achieve parameter convergence in the uncontrolled DOF.

- Plant: The model, of the same form as (3.2), is

$$M\dot{v} = -C(v)v - D(v)v - \mathcal{G}(\varphi) + G_a(v, \varphi, \xi)\theta_a \tag{4.40}$$

- Task: Design parameter update laws for $\hat{v}(t)$, $\hat{M}(t)$, $\hat{D}_i(t)$, $\hat{g}(t)$, $\hat{b}(t)$, and $\hat{\theta}_a(t)$ such that $\lim_{t\to\infty} \Delta v(t) = \vec{0}$, $\lim_{t\to\infty} \dot{\hat{M}}(t) = 0_{6x6}$, $\lim_{t\to\infty} \dot{\hat{D}}_i(t) = 0_{6x6}$, $\lim_{t\to\infty} \dot{\hat{g}}(t) = 0$, $\lim_{t\to\infty} \dot{\hat{b}}(t) = \vec{0}$, and $\lim_{t\to\infty} \dot{\hat{\theta}}_a(t) = \vec{0}$.

- Error Coordinates:

  ◎ $\Delta v(t) = \hat{v}(t) - v(t)$

  ◎ $\Delta m(t) = \hat{m}(t) - m$

  ◎ $\Delta d(t) = \hat{d}_{ii}(t) - d_{ii}\ (i = \{1, 2, ..., 6\})$

  ◎ $\Delta g(t) = \hat{g}(t) - g$

  ◎ $\Delta b(t) = \hat{b}(t) - b$

  ◎ $\Delta \theta_a(t) = \hat{\theta}_a(t) - \theta_a$

- Parameter Update Laws:

$$\dot{\hat{v}} = \hat{M}^{-1}\Big(- C(\hat{M}, v)v - \hat{D}(v)v - \hat{\mathcal{G}}(\varphi) + G_a(v, \varphi, \xi)\hat{\theta}_a\Big) - \alpha \Delta v \tag{4.41}$$

$$\dot{\hat{m}} = \Gamma_1\big(v^T\ diag(\psi_1) + \psi_2^T\ diag(\Delta v)\big)^T \tag{4.42}$$

$$\dot{\hat{d}} = \Gamma_2\big(\Delta v^T\ diag(|v|)\ diag(v)\big)^T \tag{4.43}$$

$$\dot{\hat{g}} = \Gamma_3\ \Delta \nu^T R^T(\varphi)\ e_3 \tag{4.44}$$

$$\dot{\hat{b}} = - \Gamma_4 J(\Delta \omega) R^T(\varphi)\ e_3 \tag{4.45}$$

$$\dot{\hat{\theta}}_a = - \Gamma_5\Big(G_a(v, \varphi, \xi)\Big)^T \Delta v \tag{4.46}$$

  where

  ◎ $G_a(v, \varphi, \xi, \hat{\theta}_a)$ will be shown to be bounded in consequence of the boundedness of v, φ, ξ, and $\hat{\theta}_a$

  ◎ $\psi_1 = ad(v)^T \Delta v$

- ◎ $\psi_2 = \dot{\hat{v}} + \alpha \Delta v$
- ◎ $\alpha \in \mathbb{R}_+$; $\Gamma_1, \Gamma_2, \Gamma_3, \Gamma_4, \Gamma_5 \in \mathbb{R}^{6\times 6}$ is diagonal and PDS.
- ◎ $diag\big(\hat{m}(t_0)\big)$ is PDS, or equivalently all entries in $\hat{m}(t_0)$ are positive
- ◎ $\hat{v}(t_0) = v(t_0)$

For convenience we will define $\Delta M = diag(\Delta m)$ and $\Delta D = diag(\Delta d)$. As in [52], we develop the velocity error dynamics expression

$$\begin{aligned} M\Delta\dot{v} =& M(\dot{\hat{v}} - \dot{v}) \\ =& \alpha M \Delta v - \Delta M \psi_2 - ad(v)\Delta M v - diag(|v|)\Delta D v - \\ & \Delta\mathcal{G}(R(\varphi)) + G_a(v,\varphi,\xi)\,\Delta\theta_a. \end{aligned} \tag{4.47}$$

Consider the following Lyapunov function candidate

$$\begin{aligned} V(t) =& \frac{1}{2}\Delta v^T M \Delta v + \frac{1}{2}\Delta m^T \Gamma_1^{-1}\Delta m + \frac{1}{2}\Delta d^T \Gamma_2^{-1}\Delta d + \frac{1}{2}\Gamma_3^{-1}(\Delta g)^2 \\ & + \frac{1}{2}\Delta b^T \Gamma_4^{-1}\Delta b + \frac{1}{2}\Delta\theta_a^T \Gamma_5^{-1}\Delta\theta_a. \end{aligned} \tag{4.48}$$

It is

- positive definite
- radially unbounded
- equal zero if and only if $\Delta v = \vec{0}$, $\Delta m = \vec{0}$, $\Delta d = \vec{0}$, $\Delta g = 0$, $\Delta b = \vec{0}$, and $\Delta\theta_a = \vec{0}$.

The time derivative of (4.48) is

$$\begin{aligned}\dot{V}(t) =& \frac{1}{2}\Big(\Delta\dot{v}^T M\Delta v + \Delta v^T M\Delta\dot{v}\Big) + \frac{1}{2}\Big(\Delta\dot{m}^T\Gamma_1^{-1}\Delta m\ + \Delta m^T\Gamma_1^{-1}\Delta\dot{m}\Big) + \\ & \frac{1}{2}\Big(\Delta\dot{d}^T\Gamma_2^{-1}\Delta d\ + \Delta d^T\Gamma_2^{-1}\Delta\dot{d}\Big)\ + \Gamma_3^{-1}\Delta\dot{g}\Delta g + \frac{1}{2}\Big(\Delta\dot{b}^T\Gamma_4^{-1}\Delta b\ + \Delta b^T\Gamma_4^{-1}\Delta\dot{b}\Big) + \\ & \frac{1}{2}\Big(\Delta\dot{\theta}_a^T\Gamma_5^{-1}\Delta\theta_a\ + \Delta\theta_a^T\Gamma_5^{-1}\Delta\dot{\theta}_a\Big) \\ =& \Delta v^T M\Delta\dot{v} + \Delta\dot{m}^T\Gamma_1^{-1}\Delta m\ + \Delta\dot{d}^T\Gamma_2^{-1}\Delta d\ + \Gamma_3^{-1}\Delta\dot{g}\Delta g\ + \Delta\dot{b}^T\Gamma_4^{-1}\Delta b + \\ & \Delta\dot{\theta}_a^T\Gamma_5^{-1}\Delta\theta_a \end{aligned} \tag{4.49}$$

Substituting in (4.47) yields

$$\begin{aligned}\dot{V}(t) =& -\alpha\Delta v^T M\Delta v - \frac{1}{2}\Big(v^T\Delta M\psi_1 + \psi_2^T\Delta M\Delta v\Big) \\ & -\frac{1}{2}\Big(\Delta v^T\Delta M\psi_2 + \psi_1^T\Delta M v\Big) - \\ & \Delta v^T diag(|v|)\Delta D v - \Delta v^T\Delta\mathcal{G}(R(\varphi)) + \\ & \Delta v^T G_a(v,\varphi,\xi)\Delta\theta_a + \Delta\dot{m}^T\Gamma_1^{-1}\Delta m\ + \Delta\dot{d}^T\Gamma_2^{-1}\Delta d\ + \Gamma_3^{-1}\Delta\dot{g}\Delta g + \\ & \Delta\dot{b}^T\Gamma_4^{-1}\Delta b\ + \Delta\dot{\theta}_a^T\Gamma_5^{-1}\Delta\theta_a. \end{aligned} \tag{4.50}$$

Substituting in the parameter update laws (4.42) - (4.46) yields

$$
\begin{aligned}
\dot{V}(t) = & -\alpha \Delta v^T M \Delta v - \frac{1}{2}\Big(v^T \Delta M \psi_1 + \psi_2^T \Delta M \Delta v\Big) \\
& - \frac{1}{2}\Big(\Delta v^T \Delta M \psi_2 + \psi_1^T \Delta M v\Big) - \Delta v^T diag(|v|)\Delta D v - \\
& \Delta v^T \Delta \mathcal{G}(R(\varphi)) \; + \Delta v^T G_a(v,\varphi,\xi)\Delta\theta_a + \\
& \Big(\Gamma_1 \big(v^T \; diag(\psi_1) + \psi_2^T \; diag(\Delta v)\big)^T\Big)^T \Gamma_1^{-1}\Delta m + \\
& \Big(\Gamma_2 \big(\Delta v^T \; diag(|v|) \; diag(v)\big)^T\Big)^T \Gamma_2^{-1}\Delta d + \\
& \Gamma_3^{-1}\Big(\Gamma_3 \; \Delta\nu^T R^T(\varphi) \; e_3\Big)\Delta g \; + \Big(-\Gamma_4 J(\Delta\omega) R^T(\varphi) \; e_3\Big)^T \Gamma_4^{-1}\Delta b + \\
& \Big(-\Gamma_5 \Big(G_a(v,\varphi,\xi)\Big)^T \Delta v\Big)^T \Gamma_5^{-1}\Delta\theta_a
\end{aligned} \tag{4.51}
$$

$$
\begin{aligned}
= & -\alpha \Delta v^T M \Delta v - \frac{1}{2}\Big(v^T \Delta M \psi_1 + \psi_2^T \Delta M \Delta v\Big) - \frac{1}{2}\Big(\Delta v^T \Delta M \psi_2 + \psi_1^T \Delta M v\Big) \\
& - \Delta v^T diag(|v|)\Delta D v + \Delta v^T G_a(v,\varphi,\xi)\Delta\theta_a + \\
& \big(v^T \; diag(\psi_1) + \psi_2^T \; diag(\Delta v)\big)\Gamma_1 \Gamma_1^{-1}\Delta m + \\
& \big(\Delta v^T \; diag(|v|) \; diag(v)\big)\Gamma_2 \Gamma_2^{-1}\Delta d \; - G_a(v,\varphi,\xi)\Delta v \Gamma_5 \Gamma_5^{-1}\Delta\theta_a,
\end{aligned} \tag{4.52}
$$

which makes use of the fact that Γ_i are diagonal matrices so they are symmetric by definition. Note that for all vectors $y_1, y_2 \in \mathbb{R}^6$, $diag(y_1)y_2 = diag(y_2)y_1$ and $y_1^T diag(y_2) = y_2^T diag(y_1)$. The final simplified expression is

$$
\dot{V}(t) = -\alpha \Delta v^T M \Delta v, \tag{4.53}
$$

which is negative definite in Δv and negative semidefinite in the entire error coordinates Δv, Δm, Δd, Δg, Δb, and $\Delta\theta_a$. A proof that the smallest eigenvalue of $\Delta\hat{M}$ is bounded away from zero for all time can be found [52].

We note from [52] that with v, Δv, Δm, Δd, Δg, Δb, $\Delta\theta_a$, and $G(v, \varphi, \xi)$, bounded and m, d, g, b, and θ_a constant, it is implied that $\hat{v}$, $\hat{m}$, $\hat{d}$, $\hat{g}$, $\hat{b}$, and $\hat{\theta}_a$ are bounded. If we assume that the smallest eigenvalue of $\Delta\hat{M}$ is bounded away from zero for all time then $\Delta\hat{M}^{-1}$ is bounded and thus $\Delta\dot{v}$ is bounded. Additionally $\Delta v \in \mathcal{L}_2$ and bounded $\Delta\dot{v}$ implies that $\lim_{t\to\infty} \Delta v = \vec{0}$

Since the parameter update equation (4.46) is bounded and $\lim_{t\to\infty} \Delta v = \vec{0}$ this implies that $\lim_{t\to\infty} \dot{\hat{m}} = \vec{0}$, $\lim_{t\to\infty} \dot{\hat{m}} = \vec{0}$, $\lim_{t\to\infty} \dot{\hat{g}} = 0$, $\lim_{t\to\infty} \dot{\hat{b}} = \vec{0}$, and $\lim_{t\to\infty} \dot{\hat{\theta}}_a = \vec{0}$. Thus, the estimator's angular and linear velocities asymptotically converge to the velocities of the actual vehicle and all estimated parameters converge to a common scalar multiple of their constant values [52].

4.4.2 AID Simulation Results

This section reports results utilizing the AID algorithm described in Section 4.4.1 in post-processing on simulated data with additive Gaussian noise. These simulation results corroborate the analytical stability analysis

4.4.2.1 Initial Simulation Results

For this feasibility study, 5000 seconds of vehicle motion was simulated for the identification process. Note that the adaptive gains determine how quickly the parameters converge to the true parameters, and the selection of adaptation gains is an open problem in adaptive systems theory.

Gaussian noise was added to the attitude and velocity signals to mimic the expected measurement noise of the JHU Iver3 AUV sensors. All sensors were resampled to 10 Hz, which is the operating frequency of the Microstrain. The specific noise characteristics used in the simulation study are provided in Table 4.13. These values are representative of the measured noise statistics for the Iver3 AUV onboard sensors, detailed in Section 4.2.1.

Table 4.13: Measurement sources and accuracies

State	Source	Measurement Std Dev
Attitude	Microstrain MSF	0.25°
Angular Velocity	Microstrain MST	0.01°/s
Trans Velocity	RDI	1.3 cm/s

All available control inputs were excited in open loop in an attempt to achieve persistent excitation. A summary of the inputs is provided in Table 4.14. The velocity error, i.e., the difference between the true velocity and the AID velocity in CROSSIM is plotting in Figure 4.11.

4.4.2.2 AID Noise Sensitivity Analysis

This section reports a noise-sensitivity analysis for the AID parameter estimation algorithm, run in post-processing on simulated vehicle data. The purpose of this noise sen-

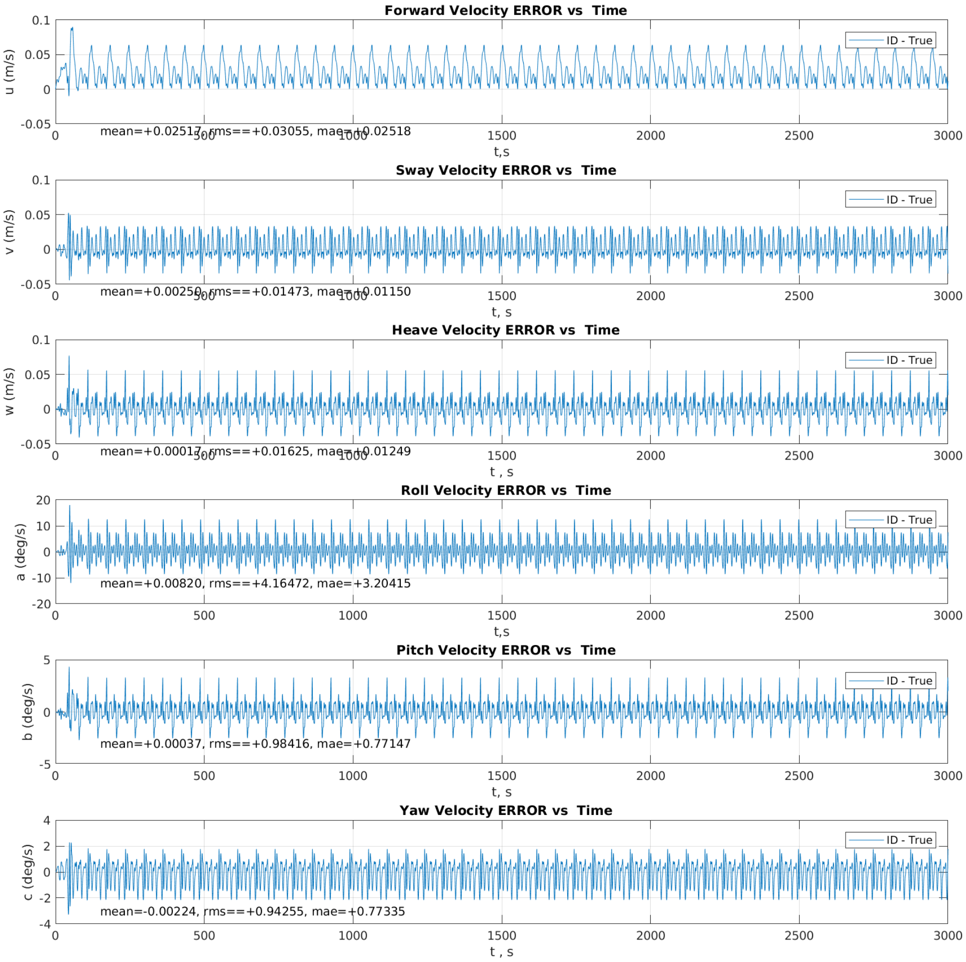

Figure 4.11: CROSSIM Velocity Error in simulation with open loop control in all 6 DOF. This figure indicates that the AID plant velocities are close to the true plant velocities in most DOF especially the translational DOF. Because the UV is equipped with an attitude sensor, velocity errors in attitude (roll, pitch, and yaw) will have a smaller effect on the performance of model-based navigation.

Table 4.14: Simulated Control Input

Actuator	IDSIM	CROSSIM
Propeller	8 + 8 * Sin(0.7 t) N	5 + 3 * Sin(0.5t) N
R Fin	5°+15° * Sin(0.4 t)	7°+5° * Sin(0.2 t)
T Fin	15° * Sin(0.2 t)	8° * Sin(0.4 t)
L Fin	5°+15° * Sin(0.4 t)	7°+5° * Sin(0.2 t)
B Fin	15° * Sin(0.2 t)	8° * Sin(0.4 t)

sitivity analysis is to determine if it is feasible to utilize the AID approach for parameter identification with the sensor suite available on board the JHU Iver3 AUV. To do this, we added noise to angular position, angular velocity, and linear velocity as described below.

Tables 4.16 and 4.17 show the MAE and RMS, respectively, for a noise sensitivity analysis of the AID algorithm in cross validation with varying amounts of linear-velocity noise and $0.01°$/s angular-rate noise and $0.25°$ angular position noise in roll and pitch.

Tables 4.18 and 4.19 show the MAE and RMS, respectively, for a noise sensitivity analysis of the AID algorithm in cross validation with varying amounts of linear-velocity noise and $0.1°$/s angular-rate noise and $0.25°$ angular position noise in roll and pitch. Figures 4.14 and 4.15 show graphically the MAE and RMS, respectively, corresponding to Tables 4.18 and 4.19.

The velocity error appears to increase slightly as a function of translational velocity noise, but appears to be relatively insensitive to noise. We believe the anomoly is because these error results are for a single run with randomly generated noise, rather than an ensemble of runs with the error averaged.

Table 4.15: Root Mean Square Error with angular-rate std dev 0.01°/s

			Ang Vel, °/s			Lin Vel, m/s		
	Roll	Pitch	x-DOF	y-DOF	z-DOF	x-DOF	y-DOF	z-DOF
RMS	1.2948	0.6383	0.8643	0.1910	0.1992	0.0065	0.0033	0.0032
MAE	0.7807	0.4312	0.5297	0.1308	0.1502	0.0055	0.0024	0.0022

4.5 Summary

This chapter presents two novel algorithms for identifying simultaneously the plant parameters—i.e., hydrodynamic mass, quadratic drag, gravitational force and buoyancy parameters—and the actuator parameters—i.e., propeller coefficient and fin lift and drag as a function of commanded angle—for second-order, underactuated UV plants in 6 DOF.

The first algorithm, termed nullspace-based least squares, uses a least squares to solve for a parameter vector in the kernel of the regressor matrix. Simulation results suggest a torpedo-shaped, underactuated UV can achieve sufficient motion in the uncontrolled DOF for a minimal parameter set to be observable in the presence of sensor noise. Simulation results with an application to cooperative acoustic navigation are presented. A noise sensitivity analysis is presented, and we concluded the NBLS approach is not robust enough to

Table 4.16: Mean Absolute Error with angular-rate noise 0.01°/s

Lin Accel Noise			Ang Vel, °/s			Lin Vel, m/s		
	Roll	Pitch	x-DOF	y-DOF	z-DOF	x-DOF	y-DOF	z-DOF
0 cm/s	0.7512	0.4206	0.5051	0.1253	0.1453	0.0053	0.0023	0.0021
0.1 cm/s	0.7601	0.4177	0.5174	0.1270	0.1458	0.0053	0.0023	0.0021
0.2 cm/s	0.7632	0.4165	0.5174	0.1274	0.1465	0.0053	0.0023	0.0021
0.4 cm/s	0.7592	0.3932	0.5156	0.1269	0.1456	0.0048	0.0024	0.0022
0.6 cm/s	1.1045	0.5917	0.7373	0.1744	0.2079	0.0076	0.0033	0.0029
0.8 cm/s	1.2813	0.7223	0.8317	0.2023	0.2253	0.0073	0.0036	0.0033
1.0 cm/s	1.2147	0.6306	0.8382	0.2174	0.2208	0.0053	0.0035	0.0036
1.2 cm/s	1.0933	0.6693	0.7097	0.2321	0.1744	0.0046	0.0029	0.0035
1.4 cm/s	1.6226	0.9075	1.0580	0.2641	0.2896	0.0076	0.0044	0.0043

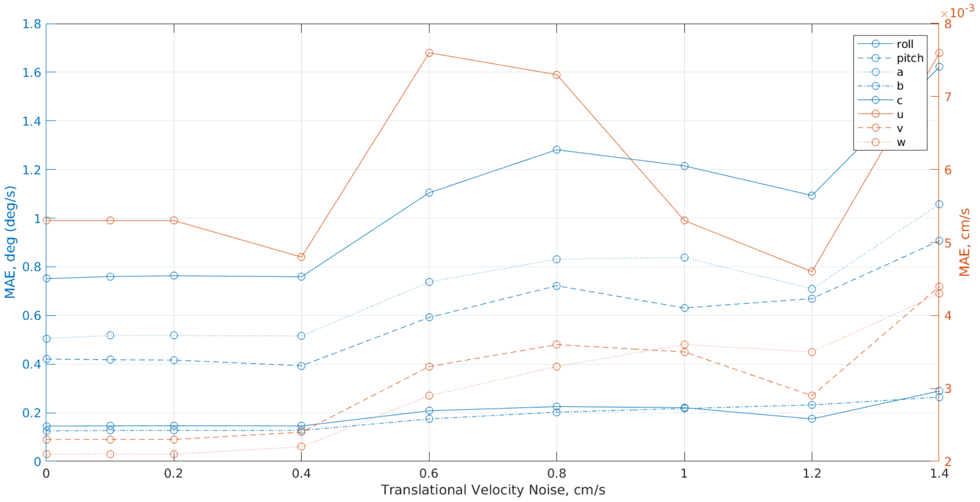

Figure 4.12: AID Noise Sensitivity Plot at 0.01 deg/s angular velocity noise: MAE vs Linear Velocity Noise In this noise-sensitivity study, the translational velocity was differentiated and then low-pass filtered to obtain the translational acceleration, and the angular velocity was differentiated and low-pass filtered to obtain the angular acceleration. Unlike the NBLS sensitivity-analysis plots reported in Section 4.3.2.3, the 1σ translational-velocity noise extends out to 1.4 cm/s. The commercially available DVL installed on the Iver3 AUV, which reports translational velocity with a standard deviation of 1.2 cm/s. For this reason, we believe it may be possible to utilize this AID approach on experimental data collected by the Iver3 AUV.

Table 4.17: Root Mean Square Error with angular-rate noise 0.01°/s

Lin Accel Noise			Ang Vel, °/s			Lin Vel, m/s		
	Roll	Pitch	x-DOF	y-DOF	z-DOF	x-DOF	y-DOF	z-DOF
0 cm/s	1.2507	0.6195	0.8277	0.1835	0.1921	0.0063	0.0032	0.0031
0.1 cm/s	1.2616	0.6159	0.8424	0.1864	0.1939	0.0063	0.0032	0.0031
0.2 cm/s	1.2580	0.6108	0.8371	0.1855	0.1943	0.0063	0.0032	0.0031
0.4 cm/s	1.2553	0.5705	0.8419	0.1858	0.1953	0.0058	0.0033	0.0032
0.6 cm/s	1.7289	0.8542	1.1585	0.2505	0.2668	0.0090	0.0044	0.0042
0.8 cm/s	1.8673	0.9955	1.2330	0.2748	0.2834	0.0090	0.0047	0.0047
1.0 cm/s	1.8636	0.8637	1.2696	0.2983	0.3044	0.0064	0.0049	0.0051
1.2 cm/s	1.5355	0.9099	0.9812	0.3057	0.2247	0.0055	0.0038	0.0047
1.4 cm/s	2.2963	1.2176	1.5115	0.3515	0.3585	0.0097	0.0057	0.0060

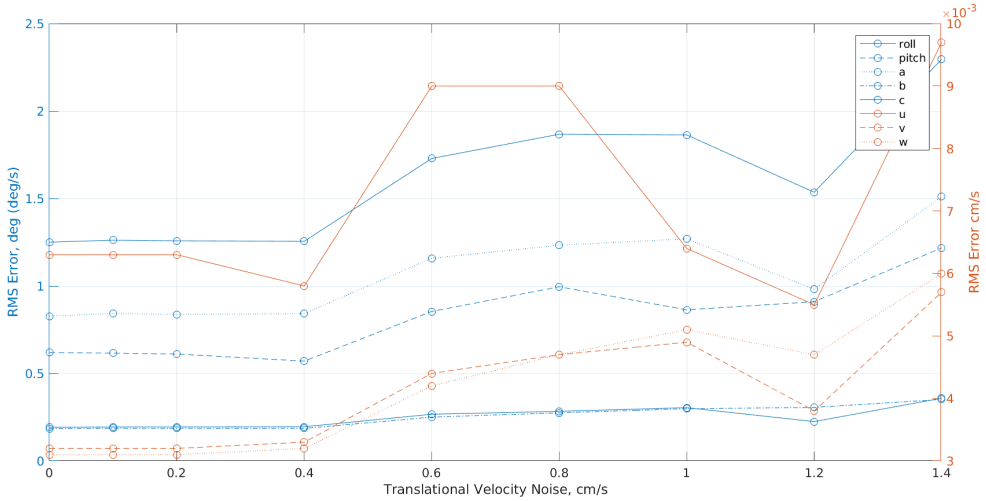

Figure 4.13: AID Noise Sensitivity Plot at 0.01 deg/s angular velocity noise: RMSE vs Linear Velocity Noise In this noise-sensitivity study, the translational velocity was differentiated and then low-pass filtered to obtain the translational acceleration, and the angular velocity was differentiated and low-pass filtered to obtain the angular acceleration. Unlike the NBLS sensitivity-analysis plots reported in Section 4.3.2.3, the 1σ translational-velocity noise extends out to 1.4 cm/s. Additionally, we note that in comparing this figure to Figure 4.13, increasing the angular-rate noise by an order of magnitude has a small net effect on the overall error. The commercially available DVL installed on the Iver3 AUV, which reports translational velocity with a standard deviation of 1.2 cm/s. For this reason, we believe it may be possible to utilize this AID approach on experimental data collected by the Iver3 AUV.

Table 4.18: Mean Absolute Error with angular-rate noise 0.1°/s

Lin Accel Noise			Ang Vel, °/s			Lin Vel, m/s		
	Roll	Pitch	x-DOF	y-DOF	z-DOF	x-DOF	y-DOF	z-DOF
0 cm/s	0.7144	0.3840	0.4848	0.1187	0.1356	0.0048	0.0022	0.0020
0.2 cm/s	0.8555	0.4818	0.5726	0.1419	0.1637	0.0059	0.0026	0.0024
0.4 cm/s	1.0120	0.5661	0.6941	0.1750	0.1865	0.0065	0.0029	0.0028
0.6 cm/s	0.8170	0.4709	0.5185	0.1320	0.1531	0.0054	0.0025	0.0022
0.8 cm/s	1.1792	0.6328	0.8090	0.2011	0.2220	0.0067	0.0035	0.0033
1.0 cm/s	1.5755	0.7916	1.1149	0.2620	0.2972	0.0098	0.0047	0.0043
1.2 cm/s	1.6087	0.7875	1.0985	0.2639	0.2829	0.0082	0.0045	0.0041
1.4 cm/s	1.5427	0.7502	1.0469	0.2594	0.2866	0.0071	0.0046	0.0041

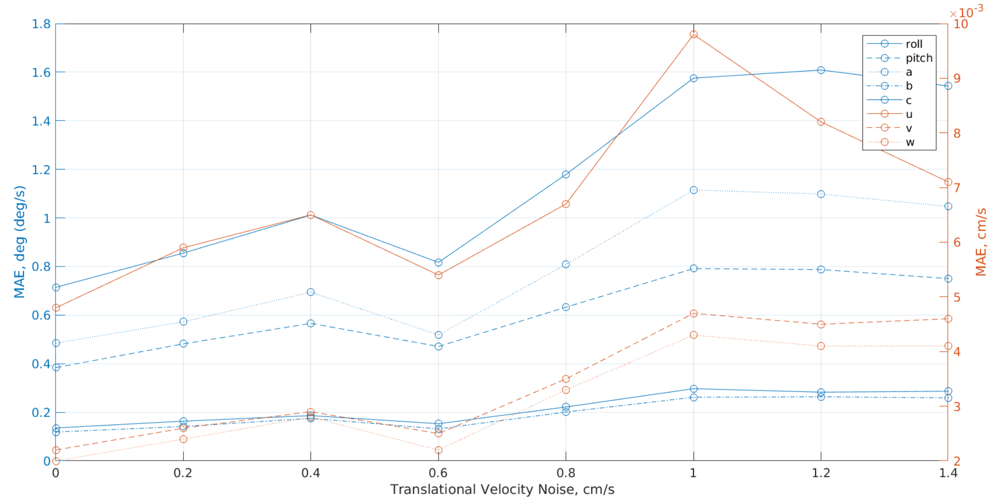

Figure 4.14: AID Noise Sensitivity Plot at 0.1 deg/s angular velocity noise: MAE vs Linear Velocity Noise In this noise-sensitivity study, the translational velocity was differentiated and then low-pass filtered to obtain the translational acceleration, and the angular velocity was differentiated and low-pass filtered to obtain the angular acceleration. Unlike the NBLS sensitivity-analysis plots reported in Section 4.3.2.3, the 1σ translational-velocity noise extends out to 1.4 cm/s. Additionally, we note that in comparing this figure to Figure 4.12, increasing the angular-rate noise by an order of magnitude has a small net effect on the overall error. The commercially available DVL installed on the Iver3 AUV, which reports translational velocity with a standard deviation of 1.2 cm/s. For this reason, we believe it may be possible to utilize this AID approach on experimental data collected by the Iver3 AUV.

Table 4.19: Root Mean Square Error with angular-rate noise 0.1°/s

Lin Accel Noise			Ang Vel, °/s			Lin Vel, m/s		
	Roll	Pitch	x-DOF	y-DOF	z-DOF	x-DOF	y-DOF	z-DOF
0 cm/s	1.1864	0.5654	0.7911	0.1751	0.1819	0.0057	0.0031	0.0029
0.2 cm/s	1.4142	0.7105	0.9432	0.2078	0.2160	0.0070	0.0036	0.0035
0.4 cm/s	1.6014	0.8046	1.0828	0.2469	0.2502	0.0075	0.0041	0.0041
0.6 cm/s	1.2818	0.6673	0.8193	0.1869	0.1959	0.0065	0.0033	0.0032
0.8 cm/s	1.9151	0.9371	1.3010	0.2886	0.3003	0.0081	0.0049	0.0048
1.0 cm/s	2.5123	1.1577	1.7488	0.3812	0.3964	0.0114	0.0064	0.0063
1.2 cm/s	2.3362	1.0516	1.5909	0.3662	0.3565	0.0099	0.0058	0.0060
1.4 cm/s	2.2552	0.9953	1.5216	0.3586	0.3621	0.0087	0.0059	0.0059

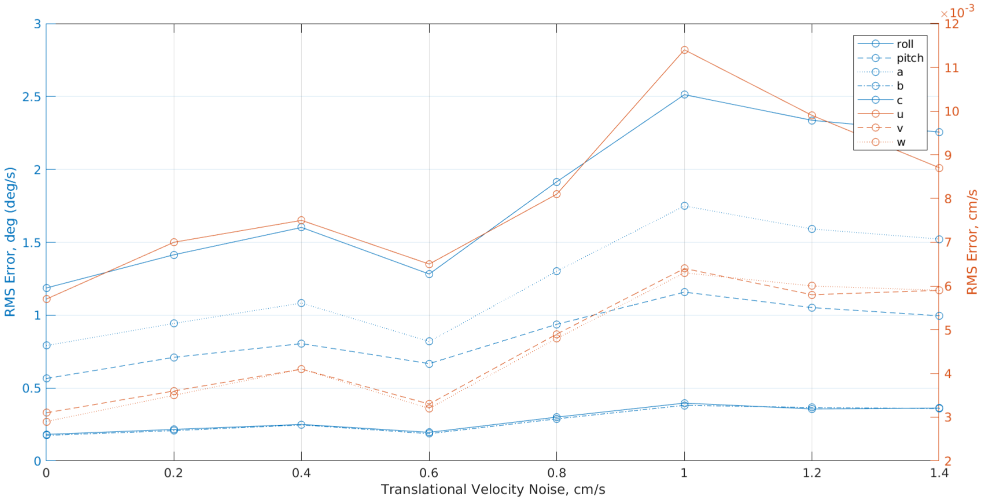

Figure 4.15: AID Noise Sensitivity Plot at 0.1 deg/s angular velocity noise: RMSE vs Linear Velocity Noise In this noise-sensitivity study, the translational velocity was differentiated and then low-pass filtered to obtain the translational acceleration, and the angular velocity was differentiated and low-pass filtered to obtain the angular acceleration. Unlike the NBLS sensitivity-analysis plots reported in Section 4.3.2.3, the 1σ translational-velocity noise extends out to 1.4 cm/s. Additionally, we note that in comparing this figure to Figure 4.13, increasing the angular-rate noise by an order of magnitude has a small net effect on the overall error. The commercially available DVL installed on the Iver3 AUV, which reports translational velocity with a standard deviation of 1.2 cm/s. For this reason, we believe it may be possible to utilize this AID approach on experimental data collected by the Iver3 AUV.

noise for parameter estimation with the JHU Iver3 AUV.

The second algorithm is an extension to the AID algorithm reported in [58] to utilize diagonal gain matrices rather than scalar gains. An analytical stability result using Lyapunov's direct method with diagonal gain matrices is reported, and numerical simulation results in 6 DOF with realistic measurement noise confirm the analytic stability result. A noise sensitivity analysis is presented, and we concluded the AID approach may work on real data collected by the sensor suite on board the Iver3 AUV.

Chapter 5

Combined Control and Navigation without a DVL: A Simulation Study

This chapter presents simulation results on combined control and navigation in a loop of a torpedo-shaped, underactuated underwater vehicle without a DVL using a feedback controller to follow a continuous reference trajectory and the CEKF formulation of cooperative navigation for position estimation.

We utilized the CEKF formulation of the cooperative acoustic navigation algorithm described in Chapter 2 and the dynamic plant model described in Chapter 3. To the best of our knowledge, no previous study has examined the combined control and cooperative navigation of low-cost underwater vehicles without a DVL utilizing a dynamic model of the submerged vehicles motion in the cooperative navigation algorithm.

5.1 Trajectory Generation

Many torpedo-shaped UVs are configured with a single propeller and aft control surfaces, i.e., they are underactuated; therefore, generating a feasible trajectory is more difficult than simply generating waypoints. There are many approaches to motion planning for underactuated robots. In this thesis, we chose to generate waypoints parameterized in time and implemented a commonly employed trackline-following algorithm: a proportional controller to compute the forward thrust and proportional derivative control (PDC) to compute the fin angles required to follow the trackline, as reported in Section 3.1.3. We ran a forward simulation of the vehicle dynamics and trackline-following PDC in a loop, and the resulting motion (i.e., the vehicle's path and corresponding velocities) formed our desired trajectory. This approach, while inefficient for online planning, is simple and ensures the trajectory is achievable.

5.2 Controller

We used a linear-quadratic regulator (LQR) controller to determine the desired moment about each axis. A key benefit of an LQR controller over the standard PDC is that the gain is computed as part of the algorithm—this makes it easier to compare performance across multiple process models without tuning the gains by hand. A comparison of the dynamic process model without a DVL to the kinematic process model with and without a DVL is the subject of future work. The LQR controller is an approach to constrained optimal control. Specifically, we seek to minimize the quadratic cost function, J, over u, i.e.,

$$\min_u J(x,u) = \min_u \int_{t_k}^{t_{k+1}} x^T Q x + u^T R u + 2x^T N u, \tag{5.1}$$

subject to the continuous-time dynamics

$$\dot{x} = Ax + Bu. \tag{5.2}$$

In the same way that we linearize (3.2) about the current state for the EKF, we linearize (3.2) about the current state to achieve linear dynamics of the form (5.2). The feedback-control law that solves the above minimization problem is

$$u = -Kx, \tag{5.3}$$

where

$$K = R^{-1}(B^T P(t) + N^T). \tag{5.4}$$

$P(t)$ is the solution to the continuous-time Riccati ordinary differential equation (ODE). A full derivation may be found in [42]. Note that the combination of the Kalman filter, in our case the EKF, and an LQR controller is known as linear-quadratic-Gaussian (LQG) control.

5.3 Simulation Results

This section reports results from a numerical simulation for a torpedo-shaped, underactuated vehicle.

Table 5.1: Simulation measurement sources, resolutions, and accuracies

			Measurement
State	Source	Update Rate	Std Dev
XY Trans	modem	30 s	1 m (range) 0.1m/s (range rate)
Z Trans	Paroscientific	7 Hz	6 cm
Heading	OCTANS	3 Hz	0.10°
Pitch, Roll	OCTANS	3 Hz	0.05°
Trans Velocity	300 kHz RDI DVL	5 Hz (when used)	0.01 m/s (when used)
Ang Vel	OCTANS	3 Hz	0.4-0.6°/s

We utilized a numerical simulation to investigate the feasibility of running the CEKF with a dynamic model in a loop with an LQR controller on a previously generated trajectory, as described in Section 5.1. We treated the control signal as piecewise-constant across time-steps and computed a forward simulation of the vehicle dynamics as the "true" state. From these signals, we generated simulated sensor measurements for each of the navigation sensors with the noise characteristics outlined in Table 5.1.

In the simulation result presented here, the vehicle conducted a simulated survey mission of ten $1\ \mathrm{km}$ tracklines spaced $100\ \mathrm{m}$ apart at a velocity of $1\ \mathrm{m/s}$ and a constant depth of $3\ \mathrm{m}$. The ship circled continuously on a $600\ \mathrm{m}$ radius at a velocity of $2\ \mathrm{m/s}$ broadcasting the first acoustic packet after $60\ \mathrm{s}$, and then regularly at $30\ \mathrm{s}$ intervals. The speed of sound was assumed constant at $1500\ \mathrm{m/s}$.

Figure 5.1 shows the true and estimated XY vehicle position with the filter's covariance plotted at every acoustic update. The arrows point from the vehicle to the ship along acoustic path with the length scaled by the angle from vertical.

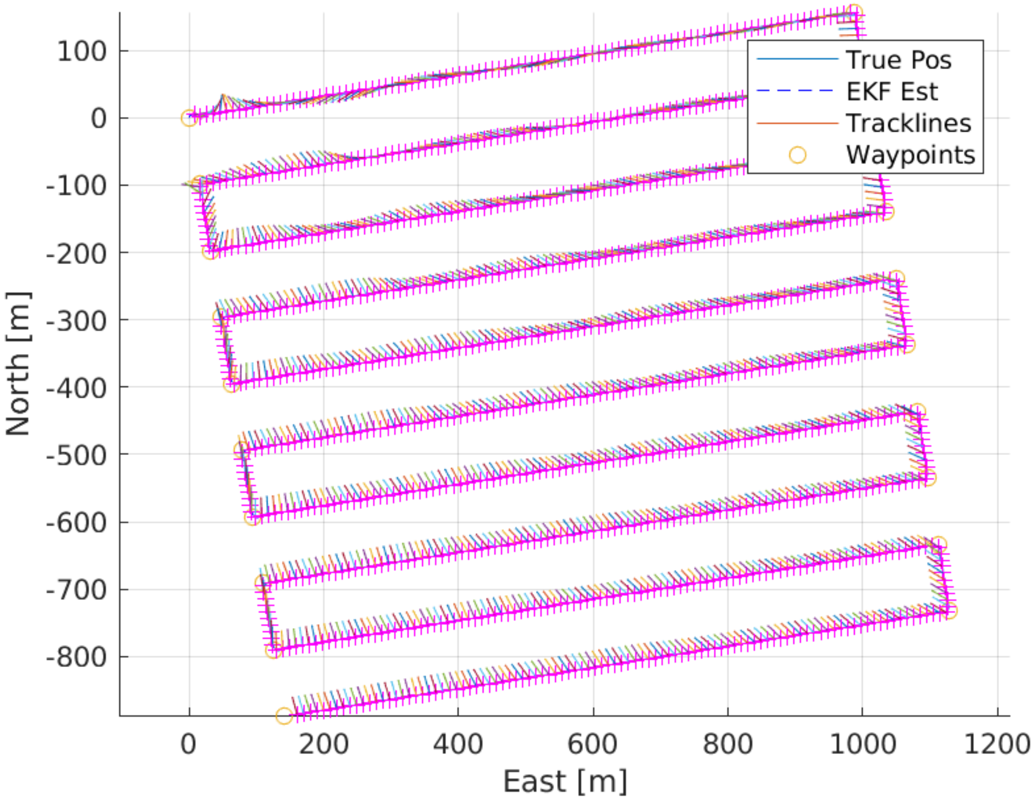

Figure 5.1: Vehicle XY position estimate from the CEKF on simulated data using the dynamical process model and no DVL with the output of the navigation solution used as the input to an LQR controller for combined control and navigation. The UVs true position is plotted in solid blue, the CEKF position estimate is plotted in dashed blue, the tracklines are plotted in red, and the waypoints are plotted as yellow circles. This figure indicates it may be feasible to do combined control and cooperative acoustic navigation utilizing a dynamic UV plant model without a DVL.

Figure 5.2 shows the XY error magnitude, i.e., the magnitude of the difference between the true position and the EKF-estimated position using the dynamic model without the DVL.

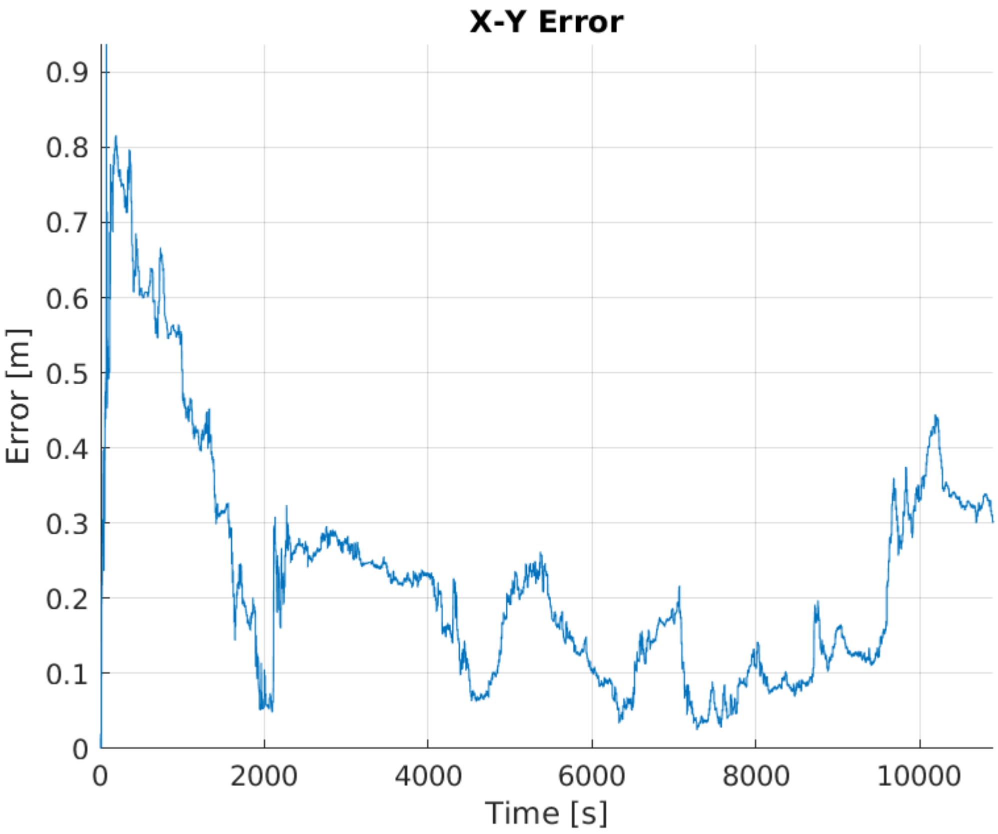

Figure 5.2: XY position error magnitude i.e., the magnitude of the difference between the true position and the CEKF-estimated position using the dynamic model without the DVL in combined control and acoustic navigation, versus mission time. This figure shows the error doing combined control and cooperative acoustic navigation utilizing a dynamic UV plant model without a DVL may be quite low.

As shown by Figures 5.1 and 5.2, our anecdotal results indicate that it may be feasible to utilize a second-order dynamic model for combined control and cooperative acoustic navigation without a DVL.

Chapter 6

Conclusion

6.1 Thesis Summary

This thesis reports theoretical and experimental results for model-based navigation for UVs lacking a DVL and dynamic-model parameter estimation for underactuated UVs, such as the now-ubiquitous class of torpedo-shaped UVs.

Chapter 2 reviews cooperative acoustic navigation and presents an observation model for acoustic range-rate observations. Chapter 2 also presents simulation and experimental results with the JHU Iver3 AUV to evaluate the addition acoustic range rate to acoustic range in the context of cooperative acoustic navigation. These results indicate that the addition of range-rate observations to acoustic range observations does not appear to significantly improve the convergence time, transient response, or steady-state position error of the CEKF with or without a DVL utilizing a kinematic model. Additionally, we note that the CEKF formulation of cooperative acoustic navigation exhibits poor performance, and even instability, without a DVL with a low-cost attitude sensor, but appears to provide acceptable results with simulated data representing a high-accuracy gyroscope, such as an iXblue OCTANS or PHINS.

Chapter 3 details a second-order nonlinear dynamical model of UVs, including a development of the nonlinear actuation function to relate commanded fin angle and propeller speed to an overall torque on the UV, for use in cooperative acoustic navigation without a DVL. Simulation and experimental results were reported utilizing the JHU Iver3 AUV. The reported results suggest a dynamic model without a DVL outperforms a kinematic model without a DVL and may outperform DVL-based dead reckoning. The experimental results validate the simulation results. Additionally, an experimental evaluation on the effect of adding (relative) velocity corrections in the form of acoustic range-rate observations to the CEKF when utilizing a dynamic model without a DVL was reported. We concluded that the addition of infrequent velocity observations, such as those provided by acoustic range rate, does not appear to improve the performance of the CEKF algorithm with a dynamic model.

Chapter 4 reports a novel nullspace-based least squares (NBLS) algorithm for underactuated UV plant-parameter and actuator-parameter estimation in 6 DOF. NBLS uses least squares to solve for a parameter vector in the kernel of the regressor matrix. Simulation results suggest a torpedo-shaped, underactuated UV can achieve sufficient motion in the uncontrolled DOF for a minimal parameter set to be observable with a small amount of sensor noise. Simulation results with an application to cooperative acoustic navigation are presented. A noise sensitivity analysis is presented, and we conclude the NBLS approach may be too sensitive to noise in translational velocity and translational acceleration to allow for parameter estimation on real data collected with the JHU Iver3 AUV.

Chapter 4 also reports an extension to the AID algorithm reported in [58] to utilize diagonal gain matrices rather than scalar gains. An analytical stability result using Lyapunov's direct method with diagonal gain matrices is reported, and numerical simulation results in 6 DOF with realistic measurement noise corroborate the analytic stability result.

Chapter 5 reports a simulation study to determine the feasibility of doing combined model-based navigation and control in a loop without a DVL. The reported simulation results suggest combined navigation and control utilizing a dynamic plant model without a DVL is feasible.

6.2 Future Work

A first step towards extending the work reported in this thesis would be to implement the algorithms reported herein to run in real-time on the JHU Iver3 AUV, i.e., implementing the AID algorithm to run in real time and implementing the DEIF formulation of cooperative acoustic navigation with a dynamical model (that utilizes AID-estimated parameters) in a loop with a trackline-following controller.

An extension to DVL-denied cooperative navigation would be to add a velocity-bias term to the cooperative navigation state to would enable water-current estimation without a DVL. In this context, it is possible that acoustic range-rate observations may improve the navigation solution.

After the AID algorithm is implemented in real-time on the JHU Iver3, parameter adaptation could be monitored to automate fault detection. The parameters estimated by the AID are assumed constant during the course of a mission; thus, changes in parameters may indicate component failure. Changes to specific parameters might be used to indicate specific failure modes, e.g., changes in mass parameters may indicate flooded compartments; changes in drag parameters may indicate entanglement; changes in actuator parameters may indicate actuator failures, such as a broken fin. A suite of adaptive model-based control (AMBC) algorithms could then be designed to compensate for specific failure modes. Automated fault-detection and compensation could enable longer duration missions at higher levels of autonomy.

Bibliography

[1] "Ocean twilight zone," Feb 2019. [Online]. Available: https://www.whoi.edu/know-your-ocean/ocean-topics/ocean-life/ocean-twilight-zone/

[2] I. Abbott and A. von Doenhoff, *Theory of Wing Sections: Including a Summary of Airfoil Data*, ser. Dover Books on Aeronautical Engineering. Dover Publications, 2012. [Online]. Available: https://books.google.com/books?id=lWe8AQAAQBAJ

[3] J. Alleyne, "Position estimation from range only measurements," Master's thesis, Naval Postgraduate School, Monterey, CA, Sept. 2000.

[4] F. Arrichiello, G. Antonelli, A. Aguiar, and A. Pascoal, "An observability metric for underwater vehicle localization using range measurements," *Sensors*, vol. 13, no. 12, pp. 16 191–16 215, 2013.

[5] P. Baccou and B. Jouvencel, "Homing and navigation using one transponder for AUV, post-processing comparisons results with long base-line navigation," in *Proceedings of the IEEE International Conference on Robotics and Automation*, vol. 4, Washington, DC, May 2002, pp. 4004–4009.

[6] ——, "Simulation results, post-processing experimentations and comparisons results for navigation, homing and multiple vehicles operations with a new positioning method using on transponder," in *Proceedings of the IEEE/RSJ International Conference on Intelligent Robots and Systems*, vol. 1, Oct. 2003, pp. 811–817.

[7] A. Bahr and J. Leonard, "Cooperative localization for autonomous underwater vehicles," in *Proc. 10th Intl. Symp. on Experimental Robotics (ISER)*, Rio de Janeiro, Brasil, July 2006, pp. 387–395.

[8] A. Bahr, "Cooperative localization for autonomous underwater vehicles," Ph.D. dissertation, Massachusetts Institute of Technology / Woods Hole Oceanographic Institution Joint Program, Cambridge, MA, USA, Feb. 2009.

[9] A. Bahr, J. J. Leonard, and M. F. Fallon, "Cooperative localization for autonomous underwater vehicles," *International Journal of Robotics Research*, vol. 28, no. 6, pp. 714–728, June 2009.

[10] T. Bailey, M. Bryson, H. Mu, J. Vial, L. McCalman, and H. Durrant-Whyte, "Decentralised cooperative localisation for heterogeneous teams of mobile robots," in *Proceedings of IEEE International Conference on Robotics and Automation*, May 2011, pp. 2859–2865.

[11] Y. Bar-Shalom, X. Rong Li, and T. Kirubarajan, *Estimation with applications to tracking and navigation*. New York: John Wiley & Sons, Inc., 2001.

[12] P. Batista, C. Silvestre, and P. Oliveira, "Single beacon navigation: Observability analysis and filter design," in *Proceedings of the 2010 American Control Conference*. IEEE, 2010, pp. 6191–6196.

[13] ——, "Single range aided navigation and source localization: Observability and filter design," *Systems & Control Letters*, vol. 60, no. 8, pp. 665–673, 2011.

[14] B. S. Bourgeois, "Using range and range rate for relative navigation," Naval Research Laboratory, Mapping, Charting, Geodesy Branch, Marine Geosciences Division, Tech. Rep., September 2007.

[15] J. A. Catipovic and L. E. Freitag, "High data rate acoustic telemetry for moving ROVs in a fading multipath shallow water environment," in *Proceedings of the Symposium on Autonomous Underwater Vehicle Technology*, June 5-6 1990, pp. 296–303.

[16] A. Chatfield, *Fundamentals of high accuracy inertial navigation*. AIAA (American Institute of Aeronautics & Astronautics), 1997, vol. 174.

[17] B. Claus, J. H. Kepper, S. Suman, and J. C. Kinsey, "Closed-loop one-way-travel-time navigation using low-grade odometry for autonomous underwater vehicles," *Journal of Field Robotics*, pp. n/a–n/a, 2017. [Online]. Available: http://dx.doi.org/10.1002/rob.21746

[18] N. Crasta, M. Bayat, A. P. Aguiar, and A. M. Pascoal, "Observability analysis of 2d single beacon navigation in the presence of constant currents for two classes of maneuvers," *IFAC Proceedings Volumes*, vol. 46, no. 33, pp. 227–232, 2013.

[19] ——, "Observability analysis of 3d auv trimming trajectories in the presence of ocean currents using single beacon navigation," *IFAC Proceedings Volumes*, vol. 47, no. 3, pp. 4222–4227, 2014.

[20] D. De Palma, F. Arrichiello, G. Parlangeli, and G. Indiveri, "Underwater localization using single beacon measurements: Observability analysis for a double integrator system," *Ocean Engineering*, vol. 142, pp. 650–665, 2017.

[21] R. M. Eustice, L. L. Whitcomb, H. Singh, and M. Grund, "Recent advances in synchronous-clock one-way-travel-time acoustic navigation," in *Proceedings of the IEEE/MTS OCEANS Conference and Exhibition*, Boston, MA, USA, Sept. 2006, pp. 1–6.

[22] R. M. Eustice, H. Singh, and L. L. Whitcomb, "Synchronous-clock one-way-travel-time acoustic navigation for underwater vehicles," *Journal of Field Robotics, Special Issue on State of the Art in Maritime Autonomous Surface and Underwater Vehicles*, vol. 28, no. 1, pp. 121–136, Jan./Feb. 2011.

[23] M. F. Fallon, G. Papadopoulos, J. J. Leonard, and N. M. Patrikalakis, "Cooperative auv navigation using a single maneuvering surface craft," *International Journal of Robotics Research*, vol. 29, no. 12, pp. 1461–1474, October 2010.

[24] T. I. Fossen, *Guidance and Control of Ocean Vehicles*. New York: John Wiley and Sons, 1994.

[25] A. Gadre, "Observability analysis in navigation systems with an underwater vehicle application," Ph.D. dissertation, Virginia Polytechnic Institute and State University, Blacksburg, Virginia, Jan. 2007.

[26] A. Gadre and D. Stilwell, "Toward underwater navigation based on range measurements from a single location," in *Proceedings of the IEEE International Conference on Robotics and Automation*, vol. 5, New Orleans, Apr. 2004, pp. 4472–4477.

[27] ——, "A complete solution to underwater navigation in the presence of unknown currents based on range measurements from a single location," in *Proceedings of the IEEE/RSJ International Conference on Intelligent Robots and Systems*, Edmonton, Alberta, Canada, Aug. 2005, pp. 1420–1425.

[28] ——, "Underwater navigation in the presence of unknown currents based on range measurements from a single location," in *Proc. Am. Control Conf.*, vol. 1, June 2005, pp. 656–661.

[29] J. G. Graver, R. Bachmayer, N. E. Leonard, and D. M. Fratantoni, "Underwater glider model parameter identification," in *Proc. 13th Int. Symp. on Unmanned Untethered Submersible Technology (UUST)*, vol. 1, 2003, pp. 12–13.

[30] M. Green and K. Scussel, "Underwater data communication and instrument release management system," US Patent, March, 2007. [Online]. Available: https://www.google.com/patents/US7187623

[31] Z. J. Harris, T. M. Paine, and L. L. Whitcomb, "Preliminary evaluation of null-space dynamic process model identification with application to cooperative navigation of underwater vehicles," in *2018 IEEE/RSJ International Conference on Intelligent Robots and Systems (IROS)*, Oct 2018, pp. 3453–3459.

[32] Z. J. Harris and L. L. Whitcomb, “Preliminary study of cooperative navigation of underwater vehicles without a DVL utilizing range and range-rate observations,” in *Proceedings of IEEE International Conference on Robotics and Automation*, 2016.

[33] J. C. Hartsfield, “Single transponder range only navigation geometry (STRONG) applied to REMUS autonomous under water vehicles,” Master’s thesis, Massachusetts Institute of Technology and Woods Hole Oceanographic Institution, Aug. 2005.

[34] O. Hegrenaes, O. Hallingstad, and B. Jalving, “Comparison of mathematical models for the HUGIN 4500 AUV based on experimental data,” in *2007 Symposium on Underwater Technology and Workshop on Scientific Use of Submarine Cables and Related Technologies*, April 2007, pp. 558–567.

[35] R. A. Horn and C. R. Johnson, *Matrix Analysis*. Cambridge University Press.

[36] M. Hunt, W. Marquet, D. Moller, K. Peal, W. Smith, and R. Spindel, “An acoustic navigation system,” WHOI, Tech. Rep. WHOI-74-6, Dec 1974.

[37] J. Jouffroy and J. Reger, “An algebraic perspective to single-transponder underwater navigation,” in *Proceedings IEEE 2006 CCA/CACSD/ISIC*, Munich, Germany, 2006, pp. 1789–1794.

[38] G. C. Karras, C. P. Bechlioulis, M. Leonetti, N. Palomeras, P. Kormushev, K. J. Kyriakopoulos, and D. G. Caldwell, “On-line identification of autonomous underwater vehicles through global derivative-free optimization,” in *2013 IEEE/RSJ International Conference on Intelligent Robots and Systems*, Nov 2013, pp. 3859–3864.

[39] J. H. Kepper IV, B. C. Claus, and J. C. Kinsey, “A navigation solution using a MEMS IMU, model-based dead-reckoning, and one-way-travel-time acoustic range measurements for autonomous underwater vehicles,” *IEEE Journal of Oceanic Engineering*, vol. 44, no. 3, pp. 664–682, July 2019.

[40] D. B. Kilfoyls and A. B. Baggeroer, “The state of the art in underwater acoustic telemetry,” *IEEE Journal of Oceanic Engineering*, vol. 25, no. 1, pp. 4–27, January 2000.

[41] J. C. Kinsey, R. M. Eustice, and L. L. Whitcomb, “A survey of underwater vehicle navigation: Recent advances and new challenges,” in *IFAC Conference of Manoeuvring and Control of Marine Craft*, Lisbon, Portugal, 2006, invited paper.

[42] D. Kirk, *Optimal Control Theory: An Introduction*, ser. Dover Books on Electrical Engineering Series. Dover Publications, 2004. [Online]. Available: https://books.google.com/books?id=fCh2SAtWIdwC

[43] C. E. LaPointe, “Virtual long baseline (vlbl) autonomous underwater vehicle navigation using a single transponder,” Ph.D. dissertation, 2006.

[44] ——, “Virtual long baseline (VLBL) autonomous underwater vehicle navigation using a single transponder,” Master’s thesis, Massachusetts Institute of Technology and Woods Hole Oceanographic Institution, June 2006.

[45] M. Larsen, “High performance autonomous underwater navigation: Experimental results,” *Hydro International*, vol. 6, no. 1, pp. 6–9, Jan./Feb. 2002.

[46] ——, “Synthetic long baseline navigation of underwater vehicles,” in *Proceedings of the IEEE/MTS OCEANS Conference and Exhibition*, vol. 3, Providence, RI, Sept. 2000, pp. 2043–2050.

[47] ——, “Synthetic long baseline navigation of underwater vehicles,” in *OCEANS 2000 MTS/IEEE Conference and Exhibition*, vol. 3, 2000, pp. 2043–2050 vol.3.

[48] ——, “Methods and systems for navigating under water,” US Patent, Nov, 2006. [Online]. Available: https://www.google.com/patents/US7139647

[49] P.-M. Lee, B.-H. Jun, and Y.-K. Lim, “Review on underwater navigation system based on range measurements from one reference,” in *OCEANS 2008 - MTS/IEEE Kobe Techno-Ocean*, April 2008, pp. 1–5.

[50] S. C. Martin and L. L. Whitcomb, “Experimental identification of six-degree-of-freedom coupled dynamic plant models for underwater robot vehicles,” *IEEE Journal of Oceanic Engineering*, vol. 39, no. 4, pp. 662–671, Oct 2014.

[51] S. C. Martin, “Advances in six-degree-of-freedom dynamics and control of underwater vehicle,” Ph.D. dissertation, The Johns Hopkins University, Baltimore, MD, August 2008.

[52] C. J. McFarland and L. L. Whitcomb, “Comparative experimental evaluation of a new adaptive identifier for underwater vehicles,” in *2013 IEEE International Conference on Robotics and Automation*, May 2013, pp. 4614–4620.

[53] C. J. McFarland and L. L. Whitcomb, “Experimental evaluation of adaptive model-based control for underwater vehicles in the presence of unmodeled actuator dynamics,” in *2014 IEEE International Conference on Robotics and Automation (ICRA)*, May 2014, pp. 2893–2900.

[54] S. McPhail and M. Pebody, “Range-only positioning of a deep-diving autonomous underwater vehicle from a surface ship,” *IEEE J. Oceanic Eng.*, vol. 34, no. 4, pp. 669–677, Oct. 2009.

[55] P. H. Milne, *Underwater Acoustic Positioning Systems*. Houston: Gulf Publishing, 1983.

[56] S. Natarajan, C. Gaudig, and M. Hildebrandt, “Offline experimental parameter identification using on-board sensors for an autonomous underwater vehicle,” in *OCEANS 2012 MTS/IEEE: Harnessing the Power of the Ocean*, 10 2012, pp. 1–8.

[57] T. M. Paine and L. L. Whitcomb, “Adaptive parameter identification of underactuated unmanned underwater vehicles: A preliminary simulation study,” in *OCEANS 2018 MTS/IEEE Charleston*, Oct 2018, pp. 1–6.

[58] T. M. Paine, “Robust model identification methods for nonlinear second-order plant models for underwater vehicles,” Baltimore, MD, May 2018.

[59] A. Palmeiro, M. Martin, I. Crowther, and M. Rhodes, “Underwater radio frequency communications,” in *OCEANS, 2011 IEEE - Spain*, june 2011, pp. 1–8.

[60] G. Parlangeli and G. Indiveri, “Single range observability for cooperative underactuated underwater vehicles.” *IFAC Proceedings Volumes*, vol. 47, no. 3, pp. 5127–5138, 2014.

[61] L. Paull, M. Seto, and J. Leonard, “Decentralized cooperative trajectory estimation for autonomous underwater vehicles,” in *Intelligent Robots and Systems (IROS 2014), 2014 IEEE/RSJ International Conference on*, Sept 2014, pp. 184–191.

[62] J. D. Quenzer and K. A. Morgansen, “Observability based control in range-only underwater vehicle localization,” in *2014 American Control Conference*. IEEE, 2014, pp. 4702–4707.

[63] P. Ridao, A. Tiano, A. El-Fakdi, M. Carreras, and A. Zirilli, “On the identification of non-linear models of unmanned underwater vehicles,” *Control Engineering Practice*, vol. 12, no. 12, pp. 1483 – 1499, 2004, guidance and control of underwater vehicles. [Online]. Available: http://www.sciencedirect.com/science/article/pii/S0967066104000152

[64] B. Ristic, S. Arulampalam, and J. McCarthy, “Target motion analysis using range-only measurements: algorithms, performance and application to ISAR data,” *Signal Processing*, vol. 82, no. 2, pp. 273–296, Feb. 2002.

[65] A. Ross and J. Jouffroy, “Remarks on the observability of single beacon underwater navigation,” in *Proceedings of the International Symposium on Unmanned Untethered Submersible Technology*, Durham, New Hampshire, Aug. 2005.

[66] M. T. Sabet, H. M. Daniali, A. Fathi, and E. Alizadeh, “Identification of an autonomous underwater vehicle hydrodynamic model using the extended, cubature, and transformed unscented Kalman filter,” *IEEE Journal of Oceanic Engineering*, vol. PP, no. 99, pp. 1–11, 2017.

[67] A. Scherbatyuk, “The AUV positioning using ranges from one transponder LBL,” in *Proceedings of the IEEE/MTS OCEANS Conference and Exhibition*, vol. 3, San Diego, CA, Oct. 1995, pp. 1620–1623.

[68] M. Shafiei and T. Binazadeh, “Application of neural network and genetic algorithm in identification of a model of a variable mass underwater vehicle,” *Ocean Engineering*, vol. 96, pp. 173 – 180, 2015.

[69] H. Singh, J. Catipovic, R. Eastwood, L. Freitag, H. Henriksen, F. Hover, D. Yoerger, J. Bellingham, and B. Moran, “An integrated spproach to multiple AUV communications, navigation and docking,” in *Proceedings of the IEEE/MTS OCEANS Conference and Exhibition*, vol. 1, Fort Lauderdale, Sept. 1996, pp. 59–64.

[70] S. Singh, M. Grund, B. Bingham, R. Eustice, H. Singh, and L. Freitag, “Underwater acoustic navigation with the WHOI micro-modem,” in *OCEANS 2006*. IEEE, 2006, pp. 1–4.

[71] D. A. Smallwood and L. L. Whitcomb, “Adaptive identification of dynamically positioned underwater robotic vehicles,” *IEEE Transactions on Control Systems Technology*, vol. 11, no. 4, pp. 505–515, July 2003.

[72] Society of Naval Architects and Marine Engineers (U.S.). Technical and Research Committee. Hydrodynamics Subcommittee, *Nomenclature for Treating the Motion of a Submerged Body Through a Fluid: Report of the American Towing Tank Conference*, ser. Technical and research bulletin. Society of Naval Architects and Marine Engineers, 1950. [Online]. Available: https://books.google.com/books?id=sZ_bOwAACAAJ

[73] T. Song, “Observability of target tracking with range-only measurements,” *IEEE Journal of Oceanic Engineering*, vol. 24, no. 24, pp. 383–387, July 1999.

[74] R. Spindel, R. Porter, W. Marquet, and J. Durham, “A high-resolution pulse-Doppler underwater acoustic navigation system,” *Oceanic Engineering, IEEE Journal of*, vol. 1, no. 1, pp. 6–13, September 1976.

[75] S. Thrun, W. Burgard, and D. Fox, *Probabilistic Robotics*, 2005.

[76] A. Tiano, R. Sutton, A. Lozowicki, and W. Naeem, “Observer Kalman filter identification of an autonomous underwater vehicle,” vol. 15, pp. 727–739, 06 2007.

[77] L. W. T.M. Paine, Z. J. Harris, “Preliminary feasibility study of adaptive parameter identification for decoupled, underactuated, unmanned underwater vehicle plant models in 6 degrees of freedom,” in *19th Yale Workshop on Adaptive and Learning Systems*, June 2019.

[78] J. Vaganay, P. Baccou, and B. Jouvencel, "Homing by acoustic ranging to a single beacon," in *Proceedings of the IEEE/MTS OCEANS Conference and Exhibition*, vol. 2, Providence, RI, Sept. 2000, pp. 1457–1462.

[79] P. W. van de Ven, T. A. Johansen, A. J. Srensen, C. Flanagan, and D. Toal, "Neural network augmented identification of underwater vehicle models," *Control Engineering Practice*, vol. 15, no. 6, pp. 715 – 725, 2007, special Section on Control Applications in Marine Systems. [Online]. Available: http://www.sciencedirect.com/science/article/pii/S0967066105002467

[80] J. M. Walls and R. M. Eustice, "An origin state method for communication constrained cooperative localization with robustness to packet loss." *The International Journal of Robotics Research*, vol. 33, no. 9, pp. 1191–1208, 2014.

[81] S. E. Webster, "Decentralized single-beacon acoustic navigation: Combined communication and navigation for underwater vehicles," Ph.D. dissertation, Johns Hopkins University, Baltimore, MD, June 2010.

[82] S. E. Webster, R. M. Eustice, C. Murphy, H. Singh, and L. L. Whitcomb, "Toward a platform-independent acoustic communications and navigation system for underwater vehicles," in *Proceedings of the IEEE/MTS OCEANS Conference and Exhibition*, Biloxi, MS, Oct. 2009, pp. 1–7.

[83] S. E. Webster, R. M. Eustice, H. Singh, and L. L. Whitcomb, "Advances in single-beacon one-way-travel-time acoustic navigation for underwater vehicles," *The International Journal of Robotics Research*, vol. 31, no. 8, pp. 935–950, 2012, http://ijr.sagepub.com/content/31/8/935.

[84] ——, "Preliminary deep water results in single-beacon one-way-travel-time acoustic navigation for underwater vehicles," in *Proceedings of the IEEE/RSJ International Conference on Intelligent Robots and Systems*, St. Louis, MO, Oct. 2009, pp. 2053–2060.

[85] S. E. Webster, J. M. Walls, L. L. Whitcomb, and R. M. Eustice, "Decentralized extended information filter for single-beacon cooperative acoustic navigation: Theory and experiments," *Robotics, IEEE Transactions on*, vol. 29, no. 4, pp. 957–974, Aug 2013.

[86] S. E. Webster, L. L. Whitcomb, and R. M. Eustice, "Preliminary results in decentralized estimation for single-beacon acoustic underwater navigation," in *Proceedings of the Robotics: Science & Systems Conference*, Zaragoza, Spain, June 2010.

[87] B. Wehbe, M. Hildebrandt, and F. Kirchner, "Experimental evaluation of various machine learning regression methods for model identification of autonomous underwater vehicles," in *2017 IEEE International Conference on Robotics and Automation (ICRA)*, May 2017, pp. 4885–4890.

[88] B. Wehbe and M. M. Krell, “Learning coupled dynamic models of underwater vehicles using support vector regression,” in *OCEANS 2017 - Aberdeen*, June 2017.

[89] N.-L. Wu, X.-Y. Wang, T. Ge, C. Wu, and R. Yang, “Parametric identification and structure searching for underwater vehicle model using symbolic regression,” *Journal of Marine Science and Technology*, vol. 22, no. 1, pp. 51–60, Mar 2017. [Online]. Available: https://doi.org/10.1007/s00773-016-0396-8

[90] D. R. Yoerger, M. Curran, J. Fujii, C. R. German, D. Gomez-Ibanez, A. F. Govindarajan, J. C. Howland, J. K. Llopiz, P. H. Wiebe, B. W. Hobson, K. Katija, M. Risi, B. H. Robison, C. J. Wilkinson, S. M. Rock, and J. A. Breier, “Mesobot: An autonomous underwater vehicle for tracking and sampling midwater targets,” in *2018 IEEE/OES Autonomous Underwater Vehicle Workshop (AUV)*, Nov 2018, pp. 1–7.

Vita

Zachary Jess Harris was born in Louisiana in 1988. He received bachelor of science degrees in Marine Engineering and Naval Architecture from Webb Institute in 2011. In August 2013, he enrolled in the Mechanical Engineering Ph.D. program at Johns Hopkins University. Zachary has been recognized with several awards, including a Webb Institute full academic scholarship 2007-2011; Marine Technology Society (MTS) Remotely Operated Vehicle scholarship first prize 2007 and runner-up 2009; Johns Hopkins University Mechanical Engineering Department Bowles Family Fellowship 2013-2014; National Defense Science and Engineering Graduate Fellowship 2014-2017.